

KfK 4210
März 1987

Stress and Lifetime Calculations for First Wall and Blanket Structural Components

**Part II:
Crack Propagation in the NET First Wall**

**E. Diegele, T. Fett, D. Munz, H. Stamm
Institut für Material- und Festkörperforschung
Projekt Kernfusion**

Kernforschungszentrum Karlsruhe

KERNFORSCHUNGSZENTRUM KARLSRUHE

Institut für Material- und Festkörperforschung

Projekt Kernfusion

KfK 4210

STRESS AND LIFETIME CALCULATIONS FOR FIRST
WALL AND BLANKET STRUCTURAL COMPONENTS

Part II: Crack propagation in the NET First Wall

E. Diegele, T. Fett, D. Munz, H. Stamm

The investigation was performed under NET-contract 155/84-028/T

Kernforschungszentrum Karlsruhe GmbH, Karlsruhe

Als Manuskript vervielfältigt
Für diesen Bericht behalten wir uns alle Rechte vor

Kernforschungszentrum Karlsruhe GmbH
Postfach 3640, 7500 Karlsruhe 1

ISSN 0303-4003

STRESS AND LIFETIME CALCULATIONS FOR FIRST WALL
AND BLANKET STRUCTURAL COMPONENTS

Part II: Crack Propagation in the NET-First Wall

Abstract

In this report lifetime results for first wall components of a fusion reactor are presented. The aim is to show the general procedure for lifetime calculations, to demonstrate the principal mechanical behaviour of plasma faced structures, to consider effects of radiation on the behaviour of the material and assess lifetimes within the framework of fatigue crack growth analysis. The treatment of lifetime predictions is outlined in case of a first wall concept proposed by the NET-team for two materials, an austenitic steel (SS316CW) and an martensitic steel (1.4914). In general the results show a superiority of martensitic steel compared with austenitic steel.

SPANNUNGS- UND LEBENSDAUERBERECHNUNGEN FÜR ERSTE WAND-
UND BLANKET-KOMPONENTEN

Teil II: Rißwachstum in der Ersten Wand für ein NET-Design

Kurzfassung

Der Bericht stellt Lebensdauervorhersagen für Komponenten der Ersten Wand eines Fusionsreaktors vor. Es wird die allgemeine Vorgehensweise für Lebensdauerberechnungen aufgezeigt, das typische mechanische Verhalten von plasma-nahen Bauteilen unter Berücksichtigung von strahlungsinduziert verändertem Materialverhalten demonstriert, und eine Abschätzung für die im Rahmen einer Ermüdungsrißwachstumsrechnung zu erwartende Lebensdauer gegeben.

Die Lebensdauervorhersage wird für ein von dem NET-Team vorgeschlagenes Erste Wand Konzept für zwei Materialien, einen austenitischen Stahl (SS316CW) und einen martensitischen Stahl (1.4914), durchgeführt. Die Ergebnisse zeigen günstigere Vorhersagen für martensitischen gegenüber austenitischem Stahl.

CONTENTS

| | | |
|-----|---|----|
| 1. | Introduction | 1 |
| 2. | Temperature and thermal stress distributions | 3 |
| 2.1 | First Wall geometry | 3 |
| 2.2 | Finite Element meshes | 4 |
| 2.3 | Thermal loads and material properties | 4 |
| 2.4 | Temperature analysis | 5 |
| 2.5 | Stress analysis - displacement constraints | 5 |
| 2.6 | Elastic stresses on boundary lines | 6 |
| 3. | Time dependent stress development | 7 |
| 3.1 | Swelling | 7 |
| 3.2 | Irradiation creep | 9 |
| 3.3 | Derivation of basic equations | 10 |
| 3.4 | Numerical results | 12 |
| 3.5 | Cyclic stresses in the wall | 13 |
| 4. | Calculation of stress intensity factors | 13 |
| 5. | Fatigue crack growth and lifetime calculations | 16 |
| 5.1 | Results of lifetime calculations | 20 |
| 6. | Summary | 22 |
| | Figures | 24 |
| | Appendix A: Analytical temperature distribution | 27 |
| | Appendix B: Influence of geometric shape on temperature and stress distribution | 38 |
| | Figures of Appendices | 39 |
| | References | 41 |

1. Introduction

The lifetime of the first wall and blanket system of fusion reactors can be limited by different failure modes such as

- excessive plastic deformation due to exceeding of yield strength or to creep
- creep rupture
- crack propagation due to cyclic loading
- wall erosion due to sputtering

Crack extension by the cyclic operation of a fusion reactor seems to be the most important failure mode. Cracks can be generated during fabrication as welding cracks, during normal operation as fatigue cracks or during plasma disruptions.

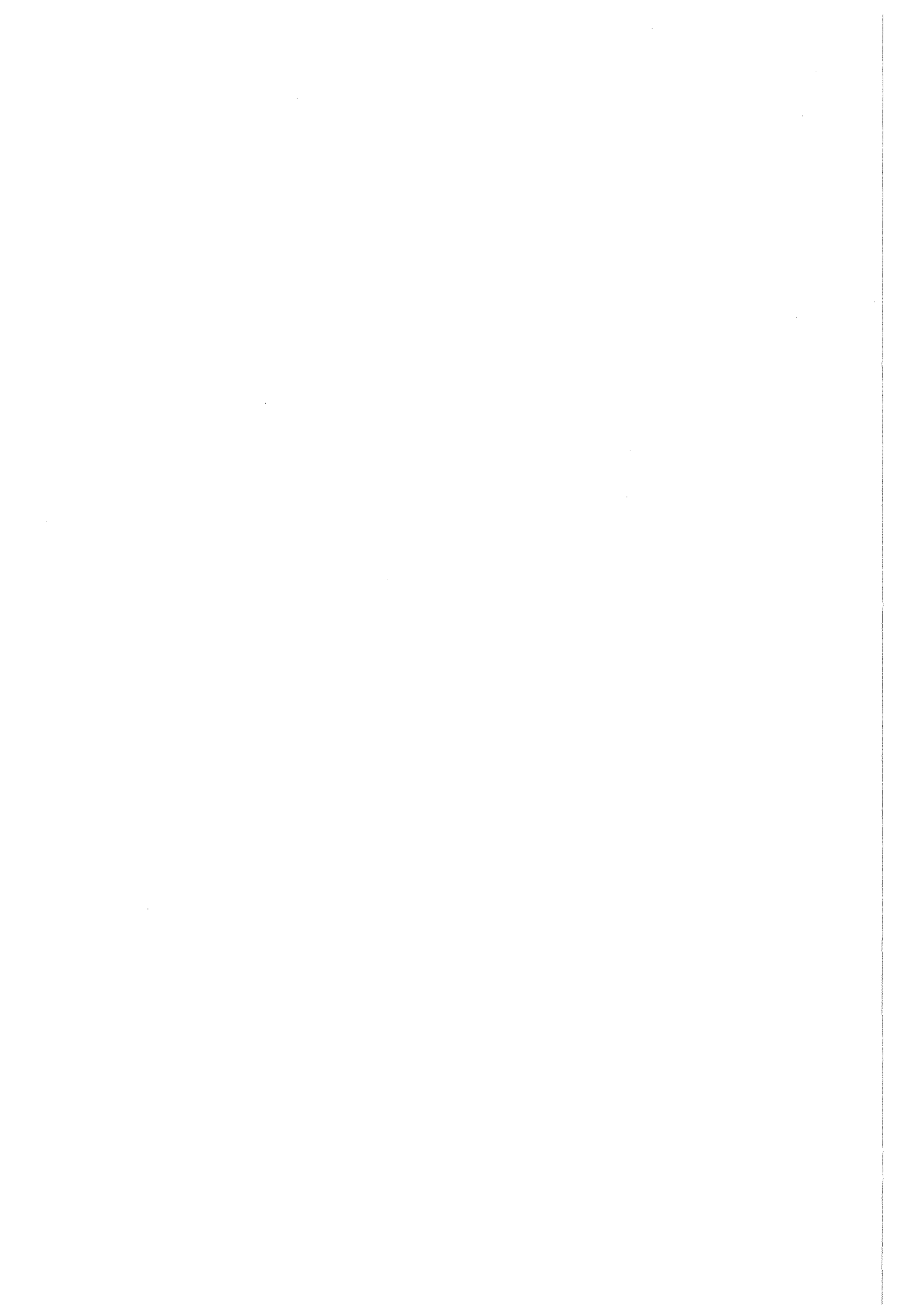
Because of geometrical boundary conditions restraining the free deformation of the wall a complex time dependent stress distribution results by combination of thermal extension, swelling, irradiation creep and internal pressure. These cyclic stresses give rise for crack extension and failure by fatigue.

In the past, lifetime calculations were performed often for constrained plates [1-4]. In [5,6] these results were extended for tubes of stainless steel SS 316(20%CW).

The purpose of this investigation is to exhibit the general behaviour of first wall and blanket structures, and to provide informations about the importance of influencing factors such as swelling, radiation creep, crack growth rates and irradiation embrittlement on the lifetime prediction.

In this study the existence of semi-elliptical surface cracks is assumed and both austenitic and martensitic candidate materials are taken into account.

As an example of practical importance the actual NET-Design [7,8] of the first wall was chosen.



2. Temperature and thermal stress distributions

In Chapter 2 calculations of temperature and stress distributions have been carried out for a First Wall (FW) concept proposed by the NET team applying finite element methods (FEM). All computations throughout this chapter are nonlinear, i.e. temperature dependent physical data have been used. Stress analyses are (thermo-) elastic and therefore can be considered only as first cycle response. Most of the investigations have been carried out for two materials, i.e. for an austenitic as well as for a martensitic steel. Some geometric data have been varied to study their influence on temperature and stress fields. The effect of changing the FW geometry on stress distributions will be presented in Appendix B. Temperatures were calculated analytically as well as numerically by the Finite Element Method (FEM). The analytical method is outlined in detail in the Appendix A. For thermal stress computations only the FE-Method was applied. In Appendix B results obtained for changed geometric data are reported.

In Chapter 3 inelastic effects like irradiation creep and swelling will be superimposed to the elastic stress fields which were calculated for a reference geometry. This reference geometry will be defined in Section 2.1. Calculations of temperature and stress fields, on the basis of which computations of fatigue crack growth and lifetime analysis have been carried out in the Chapter 3, are the main results of this chapter and will be presented in Section 2.5.

2.1 First Wall geometry

One of the First Wall designs proposed by NET consists of a panel with square coolant channels in poloidal direction. Inside of these square channels water cooled tubes are arranged. Liquid $\text{Li}_{17}\text{Pb}_{83}$ serves as bonding between the panel and the cooling tubes. The inlet temperature of the water is assumed to be 240°C , the outlet temperature is about 280°C . Figure 1 shows the First Wall design investigated.

Calculations of temperature and stress distributions have been carried out for a set of parameters. Throughout this chapter all results refer to ($d=8\text{mm}$, $c=5\text{mm}$, $R=6\text{mm}$). These parameters are defined in fig.1. All other geometric data, given by the NET team, are held constant and are summarized in fig.1 .

2.2 Finite Element meshes

Temperature distributions have been calculated using the ADINAT FE program [9]. For this purpose, the First Wall structure has been idealized by a 2-dimensional mesh with 352 elements and 1169 nodes. Thermal stresses have been computed with 3D as well as 2D elements using the FE code ADINA [10]. For 3D calculations (simulating generalized plane strain) the mesh, modelled with 208 3D elements (bodies) and 1709 nodes, is shown in fig.2a .

To simplify the model, cooling tubes and $\text{Li}_{17}\text{Pb}_{83}$ breeder material have been neglected in stress analysis, assuming no internal pressure in the channels. Because of the good agreement between 2D and 3D calculations, see Section 2.5, all other computations have been carried out using a 2D mesh with 208 2D elements (surfaces) and 725 nodes (fig.2b).

2.3 Thermal loads and material properties

The plasma side First Wall (outboard side) is exposed to a surface heat flux \dot{Q} and in the whole FW an internal heat generation \dot{q} is caused from neutrons. The cyclic thermal loading is simplified assuming the maximum values of internal heat generation and surface heat flux to be reached within 10 seconds after plasma ignition, a burn time of 250 s with constant $\dot{q}_s = 15 \text{ W/cm}^3$ and $\dot{Q} = 15 \text{ W/cm}^2$, a linear decrease of the surface heat flux and volumetric heating to 0 within 10s after burn off, and a dwell time of 50s. For $\text{Li}_{17}\text{Pb}_{83}$ a maximum volumetric heat generation of $\dot{q}_b = 20 \text{ W/cm}^3$ is assumed. At the inner side of the coolant tubes convection boundary conditions

$$\dot{Q} = h(T - T_c) \quad (1)$$

with an environmental temperature T_c for the inlet and outlet coolant water of 240°C and 280°C , respectively, and a heat transfer coefficient of $h = 3 \text{ W/(cm}^2\text{K)}$ are allowed.

As structural materials austenitic 316 SS and martensitic 1.4914 steels are considered. The latter as an alternative to the reference material 316SS. The temperature dependence of the Young's modulus E , thermal conductivity λ , thermal expansion α and volumetric specific heat c_p is illustrated in figs.3, 4 and 5. Data for the $\text{Li}_{17}\text{Pb}_{83}$ breeder material are shown in fig.6 .

2.4 Temperature analysis

Transient analyses have been carried out in the following way: The structure is heated from initial temperatures at 260°C until steady state is reached, then cooled during a dwell time of 50s and heated up again from minimum temperature. Figures 7 show two contour plots at the end of the burn time (t=260s) for the two examined materials.

The maximum temperatures, 442°C and 402°C, in the case of austenitic and martensitic steels, respectively, were obtained at point A (compare fig.1). The minimum temperatures at t=260s are 268°C in both cases.

The temperature range $\Delta T = T_{\max} - T_{\min}$ at point A over one burn cycle is $\Delta T = 167$ K for austenitic steel and $\Delta T = 127$ K for martensitic steel, respectively. Thus the cyclic temperature variation ΔT is 24% smaller using martensitic steel than that using austenitic steel.

2.5 Stress analysis

A suitable choice for boundary conditions for the FW is generalized plane strain. The structure is prevented from bending and for each point a 'free' homogeneous expansion in poloidal (z) direction is prescribed. Since 2D generalized plane strain elements are not implemented in the FE code ADINA, stress analyses have been carried out using 2D plane strain elements, with $\epsilon_{zz}(x,y)=0$ on the FW structure. Therefore compressive stresses σ_{zz}^{AD} across the whole wall occur.

The stresses in z-direction σ_{zz}^{AD} given by the ADINA program have been corrected by subtraction of the mean value in z-direction $\bar{\sigma}$:

$$\bar{\sigma} = \int \sigma_{zz}(x,y) dA / \int dA \quad (2)$$

$$\sigma_{zz} = \sigma_{zz}^{AD}(x,y) - \bar{\sigma} \quad (3)$$

These stresses σ_{zz} are in very good agreement with the results obtained by use of a simple 3D mesh as shown in fig. 2, modelling generalized plane strain conditions exactly. Therefore most of the FE calculations have been performed using the 2D model.

In figs. 8 and 9, respectively, results of 2D stress calculations for austenitic and martensitic steel are given in contour plots for steady state conditions.

For austenitic steel the stresses σ_{zz} vary from -455 MPa to 488 MPa across the wall and the stresses σ_{xx} range from -481 MPa to 413 MPa. For martensitic steel the variation of σ_{zz} and σ_{xx} is from -213 MPa to 241 MPa and from -231 MPa to 208 MPa, respectively. Tensile as well as compressive stresses and therefore the stress range over the whole structure for martensitic steel are almost exactly one half of the stresses for austenitic steel. The stresses in y-direction amount less than 15% of those in the other directions.

The first set of boundary conditions assuming generalized plane strain the x-y plane, with 'free' expansion in x-direction, but prevented from bending with respect to the y-z plane, may be too conservative.

Therefore the calculations have been repeated with a set allowing bending with respect to the y-z plane. In table 1 a comparison between boundary conditions which describe expansion in x-direction and boundary displacement conditions which additionally describe bending is given. There is a strong decrease of 34% for the variation of σ_{xx} across the wall and a moderate decrease of 17% for the stresses σ_{zz} .

2.6 Elastic stresses on boundary lines

So far the calculated stresses are those of the first cycles. Due to irradiation effects stresses besides their cyclic variation are dose dependent and, assuming a constant dose, time dependent. These inelastic effects are considered in the next chapter. For this development the elastically calculated stresses on the boundary lines (L1, L2, L3, L4) are needed. From a fitting procedure one obtains temperature and stresses in a polynomial form .

$$T = \sum_{v=1}^4 A_v^T \xi^v \quad \sigma_x = \sum_{v=1}^4 A_v^X \xi^v \quad \sigma_z = \sum_{v=1}^4 A_v^Z \xi^v \quad (4)$$

$$\sigma_y < 10 \text{ MPa} , \quad \text{with } \xi = x/b_1 \quad \text{for } 0 \leq x \leq b_1$$

$$T = \sigma_x = \sigma_y = \sigma_z = 0 \quad \text{for } b_1 < x < b_2 \quad (5)$$

$$T = \sum_{v=1}^4 A_v^T \kappa^v \quad \sigma_x = \sum_{v=1}^4 A_v^X \kappa^v \quad \sigma_z = \sum_{v=1}^4 A_v^Z \kappa^v \quad (6)$$

$$\sigma_y < 1 \text{ MPa} , \quad \text{with } \kappa = (x-b_2)/(b-b_2) \quad \text{for } b_2 \leq x \leq b$$

For line L1 and line L2 the coefficients are given in table 2.

3. Time dependent stress development

Up to now only thermoelastic stresses were considered. Under the conditions of reactor operation time-dependent inelastic effects as swelling and creep have to be taken into account, influencing the cyclic stress state.

3.1 Swelling

The basic effect of swelling is the generation of vacancies and interstitials by the displacement of atoms from their regular lattice sites. Such defects can interact in two ways.

Vacancies and interstitials can recombine to annihilate each other, or vacancies can nucleate and grow, producing so-called cavities or "voids." By the latter process the volume of the material will increase. The effect of volume expansion ΔV is called "swelling," given by

$$S = \Delta V / V = 3\Delta l / l \quad (7)$$

In case of SS316CW swelling is dependent on the temperature and the irradiation dose ϕt . Various formulae are known to describe the dependency. An empirical expression known from fast breeder technology is [11]

$$S = R \left\{ D + \frac{1}{\alpha} \ln \left[\frac{1 + \exp(\alpha(\tau - D))}{1 + \exp(\alpha\tau)} \right] \right\} \quad (8)$$

where $R = 0.002 \exp(0.042 + 1.498\beta + 0.122\beta^2 - 0.332\beta^3 - 0.441\beta^4)$ dpa^{-1}

$$\alpha = 0.15 \text{ dpa}^{-1}$$

$$\beta = (T - 500^\circ\text{C}) / 100^\circ\text{C}$$

$$D = \int \phi dt, \quad \phi = \text{fluence}$$

$$\tau = 5(4.742 - 0.2326\beta + 2.717\beta^2) \text{ dpa}$$

is the so-called "incubation dose."

HORIE et al [12] have proposed a different relationship for SS316CW

$$S/3 = 1.54 \cdot 10^{-14} \exp(T/35.5) D^{3.5} + 5.94 \cdot 10^{-13} \exp(T/46.3) D \exp(0.108 D) \quad (9)$$

In fig.10 both relations are compared. For a small dose eq.(8) yields higher swelling than eq.(9). At higher dose eq.(8) shows a linear increase in swelling while eq.(9) predicts a very rapid acceleration in swelling. Both relations will be used in this study.

Up to now the swelling relations have only described "stress-free swelling" $S_0 = S(\sigma=0)$. In the presence of stresses a different swelling behaviour has been observed. It has been found in case of hydrostatic stress components $\sigma_{Hy} \geq 0$ that

$$S(\sigma_{Hy}) = S_0 (1 + B\sigma_{Hy}) \quad (10)$$

The hydrostatic stress is given as

$$\sigma_{Hy} = (\sigma_x + \sigma_y + \sigma_z) / 3 \quad (11)$$

Values of the factor B have been compiled by EHRlich [13] and lie in the range of

$$1.6 \cdot 10^{-3} < B < 3.8 \cdot 10^{-3} \quad (\text{MPa}^{-1}) \quad \text{for } 500^\circ\text{C}$$

In this study a mean value of $B = 0.0025 \text{ MPa}^{-1}$ has been chosen. As there is no reason for negative swelling under high compressive stresses, eq.(10) has been used in a modified formulation

$$S/S_0 = \begin{cases} 1 + B\sigma_{Hy} & \text{for } B\sigma_{Hy} \geq -1 \\ 0 & \text{for } B\sigma_{Hy} < -1 \end{cases} \quad (12)$$

For martensitic steel 1.4914 swelling can be neglected. The maximum swelling rates observed are smaller than 0.07%/dpa

3.2 Irradiation creep

A metal subjected to neutron irradiation and non-hydrostatic stresses undergoes inelastic deformation, the so-called "irradiation creep." In case of multiaxial stresses the creep law can be expressed by a power law

$$d\varepsilon_{ij}^c/dD = \dot{\varepsilon}_{ij}^c = \frac{3}{2} C \sigma_{eff}^{n-1} S_{ij} \quad (13)$$

where S_{ij} is the deviatoric and σ_{eff} an effective stress. The dot is standing for the derivation with respect to the radiation dose D and not for the time derivation. The deviatoric stresses are

$$S_{ij} = \sigma_{ij} - \frac{1}{3} \sigma_{kk} \delta_{ij} \quad (14)$$

and the effective stress is given by

$$\sigma_{eff} = \left[\frac{3}{2} S_{ij} S_{ij} \right]^{\frac{1}{2}} \quad (15)$$

Results on irradiation creep of SS316 CW are available in the literature [12,14,15] and summarized in fig.11 for different temperatures. GILBERT and BATES [14] proposed the equation

$$(\varepsilon^c/\sigma)_{GB} = 0.067 D^{+5.8} 10^{-3} \exp(-8000/T) [D-8.5 \tanh(D/8.5)] \quad (16)$$

$$\varepsilon/\sigma \quad \text{in } 10^{-5} \text{MPa}^{-1}, \quad T \text{ in } ^\circ\text{C} \quad \text{and } D \text{ in dpa}$$

to describe their measurements.

This relationship is shown in fig.12 as a dashed line. Especially for high doses, the data measured are underestimated by eq.(16).

Therefore we modified this relation by

$$\varepsilon^c/\sigma = 10 \{ \exp[0.1(\varepsilon^c/\sigma)_{GB}] - 1 \} \quad (17)$$

For small neutron doses both equations are equivalent as can be shown by a power series expansion of eq.(17). At higher doses the exponential term causes significantly steeper curves. This behaviour is represented by the

dotted curve. The agreement with the experimental results is very good at 400°C and 450°C. Unfortunately, the results of HORIE et al [12] show high scatter. A good agreement can also be stated, at least in the comparison with the results of GILBERT and BATES [14] as well as with the mean value curve describing the results of WALTERS [15]. The "lower series of data points" reported in [12] is also in agreement with eq.(17).

In-pile creep tests performed on martensitic steel 1.4914 can be described by [16]

$$\dot{\epsilon}^C = C \sigma^n \exp(-3eV/kT) \quad \text{dpa}^{-1} \quad (18)$$

with $n=5$ and $C=2 \cdot 10^6$.

In fig.13 measured data of irradiation creep rates as well as thermal creep rates are shown. It becomes evident that thermal creep is not important for the temperatures considered in first wall problems.

3.3 Derivation of basic equations

Under the conditions of generalised plane strain all total strain rates $\dot{\epsilon}_x$, $\dot{\epsilon}_z$ are independent of the location in y-direction and, consequently, identical to the mean strain rates

$$\dot{\epsilon}_x = \frac{1}{b} \int \dot{\epsilon}_x dy \quad (19.1)$$

$$\dot{\epsilon}_z = \frac{1}{F} \int \dot{\epsilon}_z dF' \quad (19.2)$$

The total deformation rate of a volume element can be composed by superposition of elastic, creep and swell strain rates. Neglecting the very low stresses in the y-direction as found in the FE-calculations this yields

$$\dot{\epsilon}_x = \frac{1}{E} (\dot{\sigma}_x - \mu \dot{\sigma}_z) + \dot{\epsilon}_x^C + \frac{1}{3} \dot{S} \neq f(y) \quad (20.1)$$

$$\dot{\epsilon}_z = \frac{1}{E} (\dot{\sigma}_z - \mu \dot{\sigma}_x) + \dot{\epsilon}_z^C + \frac{1}{3} \dot{S} \neq f(x,y) \quad (20.2)$$

Integrating eqs.(20) over the wall thickness using (19) yields

$$\frac{1}{E}(\dot{\sigma}_x - \mu \dot{\sigma}_z) = -\dot{\varepsilon}_x^c - \frac{1}{3} \dot{S} + \frac{1}{b} \int \left[\frac{1}{E}(\dot{\sigma}_x - \mu \dot{\sigma}_z) + \dot{\varepsilon}_x^c + \frac{1}{3} \dot{S} \right] dy \quad (21.1)$$

$$\frac{1}{E}(\dot{\sigma}_z - \mu \dot{\sigma}_x) = -\dot{\varepsilon}_z^c - \frac{1}{3} \dot{S} + \frac{1}{b} \int \left[\frac{1}{E}(\dot{\sigma}_z - \mu \dot{\sigma}_x) + \dot{\varepsilon}_z^c + \frac{1}{3} \dot{S} \right] dy \quad (21.2)$$

where

$$b' = \begin{cases} b & \text{for cutting line C - D} \\ b + b_1 - b_2 & \text{for cutting line A - B} \end{cases} \quad (22)$$

Multiplying eq.(21.2) by μ and adding it to eq.(21.1) gives

$$\dot{\sigma}_x = \frac{E}{1-\mu^2} \left[-\dot{\varepsilon}_z^c - \mu \dot{\varepsilon}_x^c - \frac{1+\mu}{3} \dot{S} + \frac{1}{b} \int \left(\frac{1-\mu^2}{E} \dot{\sigma}_x + \dot{\varepsilon}_x^c + \mu \dot{\varepsilon}_z^c + \frac{1+\mu}{3} \dot{S} \right) dy \right] \quad (23.1)$$

Multiplying eq.(21.1) by μ and adding it to eq.(21.2) gives

$$\dot{\sigma}_z = \frac{E}{1-\mu^2} \left[-\dot{\varepsilon}_x^c - \mu \dot{\varepsilon}_z^c - \frac{1+\mu}{3} \dot{S} + \frac{1}{b} \int \left(\frac{1-\mu^2}{E} \dot{\sigma}_z + \dot{\varepsilon}_z^c + \mu \dot{\varepsilon}_x^c + \frac{1+\mu}{3} \dot{S} \right) dy \right] \quad (23.2)$$

By solution of the system of eqs.(23) the time dependent stresses in the whole structure can be determined. Since the stress rates appear in the integrals on the right hand side ,too, an iterative procedure is required.

3.3.1 Solution for the simplified problem

The problem can be substantially reduced when the small variation of Young's modulus E in the interesting temperature range of $300^\circ\text{C} \leq T \leq 500^\circ\text{C}$ is taken into account. According to the data of Section 2. a mean value $E \approx 1.8 \cdot 10^5$ MPa can be chosen which deviates less than $\pm 3\%$ from the experimental curve.

Neglecting the temperature dependence of E has only a small influence because the deviations in both directions will compensate each other. Using the temperature independent average Young's modulus, $(1-\mu^2)/E$ can be put in front of the integrals. Due to the absence of normal forces, i.e. $\int \dot{\sigma}_x dy = 0$, eq.(23.1) is reduced to

$$\dot{\sigma}_x = \frac{E}{1-\mu^2} \left\{ -\dot{\varepsilon}_z^c - \mu \dot{\varepsilon}_x^c - \frac{1+\mu}{3} \dot{S} + \frac{1}{b} \int \left[\dot{\varepsilon}_x^c + \mu \dot{\varepsilon}_z^c + \frac{1+\mu}{3} \dot{S} \right] dy \right\} \quad (24.1)$$

By integrating eq.(20.2) over the total x-y-cross section instead of over the thickness only and considering the equilibrium conditions

$$\int \sigma_z dF' = 0 \quad \text{and} \quad \int \sigma_x dF' = \int \left[\int \sigma_x dy \right] dx = 0$$

one obtains

$$\dot{\sigma}_z = E \left[-\dot{\epsilon}_z^c - \frac{1}{3} \dot{S} + \frac{1}{F} \int (\dot{\epsilon}_z^c + \frac{1}{3} \dot{S}) dF' \right] + \mu \dot{\sigma}_x \quad (24.2)$$

The numerical solution of the system, eq.(24.1) and eq.(24.2), becomes much simpler.

3.4 Numerical results

The following calculations are carried out for the state of constant operation. From figs.14-20 the complete stress history can be understood.

The results will be shown e.g. for the stress component σ_x .

Immediately after the start of operation the stress state is given by the thermoelastic stresses (the internal pressure in the channels can be neglected). These stresses become very high because the bending deformations are fully restrained.

Due to irradiation creep the thermal stresses start to relax against zero. After swelling becomes noticeable for SS316CW compressive stresses are generated in high temperature regions and tensile stresses in low temperature regions because swelling at high temperatures is higher than swelling at low temperatures. The swelling effect is responsible for the moderate increase of stresses for a dose $\phi t > 25 \text{ dpa}$, as shown in fig.14 for different locations. Here the neutron flux in the rear part of the first wall was assumed to be equal to the flux at the front parts.

Figure 15 shows the stress distribution through the thickness of the wall along the line 1-2,3-4 for both a homogeneous neutron flux distribution and a reduced neutron flux in the rear part.

The influence of a reduced neutron flux in the rear wall part on the time dependent stresses is demonstrated in fig.16. If the neutron flux in the rear wall is reduced by less than 30% of the neutron flux in the front wall all effects of shading can be neglected.

From fig.17 the influence of the choice of a special swelling formula can be judged. Calculations based on the swelling formula eq.(8) as reported by WATSON [11] indicate an insignificantly earlier and more pronounced stress increase. This becomes quite clear from fig.10 because for the fluences

considered here eq.(8) causes higher swelling than eq.(9) proposed by HORIE et al [12].

Finally the effect of the chosen creep law is demonstrated in fig.18 . Here the difference is shown which exists between eq.(17) as used in all other calculations and the creep formula eq.(16) proposed by GILBERT and BATES [14]. The small deviations observed can be easily understood from the curves in fig.12. For 400 and 450°C it can be seen that substantial deviations between both formulas will not appear below 30dpa.

For the martensitic steel 1.4914 appreciable stress reduction during the first 50dpa occurs only in the hottest zone at the plasma faced surface (fig. 19) Apart from small stress changes, which are due to the condition of equilibrium the stresses in the rest of the structure remain nearly constant (fig.20).

3.5 Cyclic stresses in the wall

In most fusion reactors the plasma is heated by direct-current, with the plasma acting as a secondary winding of a transformer. The magnetic field varies constantly in time and produces a constant current in the plasma. Before the magnetic field reaches the saturation the reactor operation has to be interrupted. Therefore reactors are operating cyclically.

As a consequence of these cycles the thermal stresses change periodically. If the burn-off times are long enough, the temperature in the whole wall will become nearly equal to the temperature T_0 of the coolant medium. Due to this temperature changes $\Delta T = T - T_0$, cyclic thermoelastic stresses occur. For shorter interruptions the assumption of complete temperature balance in the wall becomes a worst case assumption with respect to crack growth behaviour.

Figure 21 represents the cyclic stresses at locations ① and ③. For the sake of clarity the duration of the cycles is not given on the correct scale.

4. Calculation of stress intensity factors

Cyclic stresses are responsible for crack growth. In welded structures e.g. the rear part of the first wall, pre-existing cracks cannot be excluded because only defects above a minimum size can be detected. But also in the plasma faced surface cracks are generated by melting of surface layers during plasma disruptions [17].

The fracture mechanical loading quantity characterizing the stress state at the crack tip is the stress intensity factor K . Very often it may be suffi-

cient to describe the surface crack as a semi-ellipse with the axes a and c and just to know the stress intensity factor at the deepest point K_A and at the surface K_B (fig.22). These stress intensity factors in a plate of thickness t are dependent on the aspect ratio a/c , the relative crack depth a/t , and the stress field σ in the uncracked plate.

For brittle fracture the question arises whether unstable fracture occurs if the maximum K -value applied along the crack front exceeds K_{Ic} . It is also conceivable that a K -value averaged in some way along the crack front has to be used taking into account the smaller K -values near the point of maximum K . The same question arises if fatigue crack growth is considered.

GRUSE and BESUNER [18] have outlined the calculation of averaged stress intensity factors. For the deepest point A and the surface point B (fig.23) the averaged K -values are calculated according to

$$\overline{K_A}^2 = \frac{1}{\Delta S_A} \int K^2(\vartheta) d|\Delta S_A(\vartheta)| \quad (25.1)$$

$$\overline{K_B}^2 = \frac{1}{\Delta S_B} \int K^2(\vartheta) d|\Delta S_B(\vartheta)| \quad (25.2)$$

In case of symmetric load $\sigma(x,y)=\sigma(x,-y)$ eqs.(25) can be written [18]

$$\overline{K_A} = \frac{H}{K_{rA}} \frac{4}{\pi c} \int_{y=0}^c \int_{x=0}^{a^*} \sigma(x,y) \frac{\partial u_r}{\partial a} dx dy \quad (26.1)$$

$$\overline{K_B} = \frac{H}{K_{rB}} \frac{4}{\pi a} \int_{y=0}^c \int_{x=0}^{a^*} \sigma(x,y) \frac{\partial u_r}{\partial c} dx dy \quad (26.2)$$

with

$$a^* = a[1-(y/c)^2]^{\frac{1}{2}}$$

and

$$H = \begin{cases} E & \text{for plane stress} \\ E/(1-\nu^2) & \text{for plane strain} \end{cases}$$

In order to evaluate eq.(26) the averaged stress intensity factors for a reference load $\overline{K_{rA}}$ and $\overline{K_{rB}}$ as well as the crack opening displacement field $u_r(x,y)$ for the reference loading case have to be known.

Following a suggestion by MATTHECK et al [19] the crack opening field can be described by

$$u_r = \sqrt{8} \frac{\sigma_0}{H} F_A(a) a^* \sum_{\nu=0}^N C_\nu (1-(x/a^*))^{\nu+\frac{1}{2}} \quad (27)$$

with $N=1$. The integrals in eqs.(26) can be solved analytically if the stress distribution is assumed to be given by a power series

$$\sigma(x) = \sum_{\mu} A_{\mu} (x/t)^{\mu} \quad (28)$$

The evaluation of eqs.(26) yields, as shown in [20]

$$\overline{K}_A = \frac{8\sqrt{2}t^2\sigma_0}{K_{rA}\pi} \frac{d}{da} F_A \sum_{\mu} (D_{\mu} + C_1 E_{\mu}) (a/t)^{\mu+2} \quad (29.1)$$

$$\overline{K}_B = \frac{8\sqrt{2}t^2\sigma_0}{K_{rB}\pi} \frac{d}{dc} F_A \sum_{\mu} (D_{\mu} + C_1 E_{\mu}) (a/t)^{\mu+2} (c/a) \quad (29.2)$$

with the coefficients

$$D_{\mu} = A_{\mu} 2^{\mu+2} \frac{\Gamma^2(\mu/2+2)\Gamma(\mu+1)\Gamma(3/2)}{\Gamma(\mu+4)\Gamma(\mu+5/2)} \quad (30.1)$$

$$E_{\mu} = A_{\mu} 2^{\mu+2} \frac{\Gamma^2(\mu/2+2)\Gamma(\mu+1)\Gamma(5/2)}{\Gamma(\mu+4)\Gamma(\mu+7/2)} \quad (30.2)$$

The function

$$C_1 = \frac{15\pi^2}{32\sqrt{2}F_A a^2} \int_0^a \overline{F^2}_{rA} a' da' - \frac{5}{3} \quad (31)$$

can be computed using the condition of selfconsistency, where

$$\overline{F^2}_A = \frac{4}{\pi} \int_0^{\pi/2} F^2 \sin^2 \phi d\phi \quad (32.1)$$

$$\overline{F^2}_B = \frac{4}{\pi} \int_0^{\pi/2} F^2 \cos^2 \phi d\phi \quad (32.2)$$

Pure tension was used for the reference load case. For the geometric function we applied the solution given by NEWMAN and RAJU [21]. With the geometric data of fig.22 we obtain

$$F(a, c, \gamma) = [M_1 + M_2(a/t)^2 + M_3(a/t)^4] g f_\gamma / \phi \quad (33)$$

$$\begin{aligned} M_1 &= 1.13 - 0.09(a/c) & g &= 1 + [0.1 + 0.35(a/t)^2](1 - \sin \gamma)^2 \\ M_2 &= -0.54 + 0.89/(0.2 + a/c) & f_\gamma^4 &= [\sin^2 \gamma + (a/c)^2 \cos^2 \gamma] \\ M_3 &= 0.5 - 1/(0.65 + a/c) + 14(1 - a/c)^{24} & \phi &= [1 + 1.464(a/c)^{1.65}]^{1/2} \end{aligned}$$

Introducing this formula into eqs.(32) and (31) one obtains after a fitting procedure [20]

$$C_1 = \sum_{\mu=0}^4 A_{0\mu} (a/c)^\mu + \sum_{\mu=0}^4 A_{1\mu} (a/c)^\mu (a/t)^{2\mu-1} + \sum_{\nu=2}^4 \sum_{\mu=0}^4 A_{\nu\mu} (a/c)^\mu (a/t)^{2\nu} \quad (34)$$

for $0 < a/t < 1$ and $0.1 < a/c < 1$ with the coefficients

| | | | | |
|----------------------|----------------------|----------------------|----------------------|----------------------|
| $A_{00} = -0.087852$ | $A_{10} = -0.053532$ | $A_{20} = 0.078357$ | $A_{30} = -0.076659$ | $A_{40} = 0.026680$ |
| $A_{01} = -0.016774$ | $A_{11} = 0.581998$ | $A_{21} = -0.754132$ | $A_{31} = 0.613202$ | $A_{41} = -0.178372$ |
| $A_{02} = -0.009208$ | $A_{12} = 0.342860$ | $A_{22} = -0.486732$ | $A_{32} = 0.314256$ | $A_{42} = -0.133334$ |
| $A_{03} = 0.021931$ | $A_{13} = -0.467154$ | $A_{23} = 0.939698$ | $A_{33} = -0.682336$ | $A_{43} = 0.178721$ |
| $A_{04} = -0.009636$ | $A_{14} = 0.201806$ | $A_{24} = -0.405997$ | $A_{34} = 0.316057$ | $A_{44} = -0.095833$ |

Using eqs.(29) and (31) the stress intensity factors of semi-elliptic surface cracks for time dependent stress distributions can be computed.

5. Fatigue Crack growth and lifetime calculations

The propagation of cracks in cyclically loaded structures is mainly a consequence of plastic deformations at the crack tip. These deformations and hence the crack growth rate are controlled by ΔK . Other crack growth mechanisms caused by static load in a corrosive environment will be excluded. For ΔK -controlled crack growth numerous relationships have been developed since the early 1960s. Taking into account a threshold ΔK_0 , below which no crack growth occurs, and an acceleration of crack growth rate near the critical stress intensity factor K_{Ic} , a modified Forman equation proposed by SPEIDEL [22] seems to be most appropriate. It reads

$$\frac{da}{dN} = \frac{C_1 \lambda^m [f \Delta K - \Delta K_0]^n}{K_{Ic} - \lambda f \Delta K} \quad (35)$$

where

$$\lambda = \frac{1}{1-R} \quad ; \quad R = K_{\min}/K_{\max} \quad (36)$$

and

$$f = E(T_1)/E(T) \quad (37)$$

is a correction factor to model the temperature effect caused by the temperature dependent Young's modulus. T_1 is the room temperature. Eq.(35) was applied for both points A and B of the crack contour.

ΔK is given by the difference between the maximum (K_{\max}), and minimum value (K_{\min}) during each cycle

$$\Delta K = K_{\max} - K_{\min} \quad (38)$$

The material constants for SS316CW are taken from WATSON[11] for air environment

$$\begin{aligned} C_1 &= 3.122 \cdot 10^{-9} && \text{(for da/dN in m/cycle)} \\ n &= 2.95 \\ K_{Ic} &= 150 && \text{MPa}\sqrt{\text{m}} \\ m &= \begin{cases} 1-0.31R-1.23R^2 & \text{for } R>0 \\ 1.88 & \text{for } R<0 \end{cases} \\ \Delta K_0 &= \begin{cases} 5.4(1-0.9R) \text{ MPa}\sqrt{\text{m}} & \text{for } R>0 \\ 5.4(1-0.2R) \text{ MPa}\sqrt{\text{m}} & \text{for } R<0 \end{cases} \end{aligned} \quad (39)$$

The wall may fail when K_{\max} is bigger than a critical value K_{Ic} , the plane strain fracture toughness. Because of irradiation embrittlement K_{Ic} is not a constant, but decreases with the neutron dose.

Unfortunately, not enough data on K_{Ic} as a function of the neutron dose are available in the literature. Therefore, we make use of models to calculate K_{Ic} from tensile test data on irradiated specimens. A semiempirical relation is given by the HAHN and ROSENFELD model as

$$K_{Ic} = n \sqrt{2E\sigma_y \epsilon_f / 3} \quad (40)$$

where n is the work hardening exponent, σ_y the yield strength, and ϵ_f the fracture strain. Evaluations of tensile tests by ODETTE and FREY [23] using (40) resulted in the curves depicted in fig.24a. From this set of curves WATSON [11] fitted the equation

$$K_{Ic} = 115 \exp(-0.25\phi t) + 35 \exp(-0.0134\phi t) \quad (41)$$

for $T=500^\circ\text{C}$. This relation which we used in earlier studies [6,8], does not seem to be the best representation of the curves, as can be seen by comparing the dotted line with the solid lines in fig.24a.

For the calculations presented here a relation for slightly lower temperatures is of more interest.

A formula -fitted to the results of fig.24a for the total range $400^\circ\text{C} \leq T \leq 600^\circ\text{C}$ - can be expressed by

$$K_{Ic} = K_{Ico} [0.585 \exp(-0.264D^*) + 0.15 \exp(-0.05D^*)] \quad (42)$$

with

$$D^* = D \exp[-0.094(T-400)] \quad , \quad D = \phi t \quad , \quad T \text{ in } ^\circ\text{C}$$

$$K_{Ico} = 180 - 0.15 T$$

The agreement with the results of [23] can be judged from fig.24b.

In contrast to the dramatically decreasing K_{Ic} -values WOLFER and JONES [24] found a much more moderate dose dependency. Whilst the Hahn-Rosenfeld model is based on the concept of homogeneous plastic deformation at the crack tip, WOLFER and JONES considered flow localisation and subsequent channel fracture. Their consideration carried out for 420°C yields the dash-dotted line in fig.24a. It can be expressed by

$$K_{Ic} = 130[0.315 \exp(-0.2 D) + 0.685 \exp(-0.019 D)] \quad (43)$$

This result is also used in this study.

Obviously there is a great uncertainty in K_{Ic} for irradiated material.

This has to be kept in mind for assessing the lifetime calculations.

Fatigue crack growth measurements were not available for martensitic steel 1.4914, but from other martensitic steels the crack growth behaviour can be estimated. Figure 25 shows fatigue measurements carried out with different martensitic steels [25]. In addition, the crack growth rates for SS316CW represented by the modified Foreman equation are plotted as solid line. Because of the good agreement with the results of martensitic steels, we used eq.(35) for both the austenitic and martensitic steel. For 1.4914 the embrittlement due to irradiation seems to be not as important as in case of SS316. Nevertheless, for a conservative calculation the same decrease of K_{Ic} with neutron dose was assumed.

The lifetime calculations were performed in the following way:

- Calculation of the purely elastic thermal stresses using the FEM.
- By solution of eq.(23) or (24) the time-dependent stress distributions were determined step by step, using the FEM results as initial conditions.
- Using a fitting procedure the stresses were expressed by 4th order polynomials. Their coefficients A_ν ($\nu=0, \dots, 4$) had to be determined for each time step separately. In the first time step these coefficients are identical to the thermal values A_ν of eqs.(4,6).
- Starting with the initial geometric data (a_1, c_1) of assumed pre-existing cracks, the weighted averaged stress intensity factors were calculated for points A and B by use of eqs.(29) and (30).
- From eqs.(38) and (36) the crack growth parameters ΔK_A , ΔK_B , R_A , and R_B were obtained.
- This gave the crack extensions Δa at point A and Δc at points B for the first cycle by introducing ΔK_A , R_A or ΔK_B , R_B into eq.(35).
- The crack increments were added to the old values
$$a \rightarrow a + \Delta a$$
$$c \rightarrow c + \Delta c$$
and the shape of the crack was assumed to remain semi-elliptical.

- For the following cycles the whole procedure had to be repeated until the maximum averaged K-factor reached the dose dependent fracture toughness K_{Ic} or the crack tip at point A penetrated the structure. In this cycle failure of the wall was stated.

5.1 Results of lifetime calculations

Lifetime calculations were carried out for various initial crack depths a_i and several aspect ratios a_i/c_i . To characterise the crack extension the maximum averaged stress intensity factors $\overline{K}_{A,max}$ or $\overline{K}_{B,max}$ are plotted as a function of the time of operation.

The calculations are based on the following data:

$$N = 10 \text{ cycles/h} , \phi = 20 \text{ dpa/yr}$$

$$T = 450^\circ\text{C} \text{ assumed to be constant in the front part}$$

$$T = 350^\circ\text{C} \text{ assumed to be constant in the rear part}$$

In fig.26 the development of a semi-circular crack situated at the plasma faced surface is represented in detail. The maximum and minimum values of \overline{K}_A and \overline{K}_B as well as the crack depth a , the aspect ratio a/c , the R-ratio, and the related ΔK -value have been plotted (fig.26b).

Figure 27 shows the development of a semi-circular crack with $a_i=0.2\text{mm}$ and $c_i=0.2\text{mm}$ for the different K_{Ic} -dependencies given by eqs.(41), (42) and (43).

As expected from fig.24 the maximum crack extension results using eq.(42). To be conservative eq.(42) was used for a worst case consideration.

The influence of the crack geometry is outlined in detail for cracks assumed to exist in the front part of the wall.

In fig.28 the influence of the initial crack depth is represented for semi-circular cracks situated at the plasma faced surface. Failure of the wall occurs at the intersections with the K_{Ic} -curve, where the maximum K-value reaches the fracture toughness. These intersections are marked by small circles. It is evident that the lifetime resulting from these conditions increases with decreasing crack size.

The effect of the aspect ratio a/c can be seen from fig.29. Maximum lifetimes are found for semi-circular cracks.

The development of the crack shape during crack growth is represented in fig.30. Whilst semi-circular cracks become more and more elliptic with increasing crack depth, semi-elliptical cracks first change into a more semi-circular shape, and with increasing crack size the shape becomes

elliptic again. This behaviour is well-known in fracture mechanics for specimens with stress gradients, i.e. for bending tests [26].

In fig.31 the lifetimes due to cracks at the plasma faced surface are compared with lifetimes due to cracks situated in the rear wall part. The real lifetime of the FW-structure for a given initial crack size is determined by the lower one of the two curves. The crack growth behaviour depends on crack size and can be understood from fig.32 .

For small cracks the ΔK -values are below the threshold ΔK_0 . Therefore no crack extension appears and failure is only caused by reducing the K_{IC} due to irradiation embrittlement. This is the case for front wall cracks as well as for rear wall cracks.

Large cracks yield short lifetimes for both wall regions. But in case of a medium crack size a different behaviour is observed for front and rear wall cracks.

Whereas at the front side the cracks grow continuously because of increasing $K_{A \max}$ at the rear side the cracks grow only in the first time of operation when $K_{A \max}$ is relative high. With increasing time the maximum stress intensity factor decreases and the initially growing crack stops. Failure is then caused by reduced toughness.

According to fig.24 the calculated lifetimes at the rear wall side are shorter because the lower temperatures are responsible for a higher irradiation embrittlement. Another reason for faster crack growth is the positive R-ratio that occurs in the rear wall from the beginning of operation.

A comparison between lifetimes calculated for austenitic steel SS316CW and martensitic steel 1.4914 is shown in fig.33 . Because of the influence of the significantly lower thermal stresses due to the lower coefficient of thermal expansion and the higher thermal conductivity it was expected that martensitic steel should be superior to austenitic steel.

At least for front wall cracks this superiority can be seen in fig.33 where the lifetimes for martensitic steel are compared with the results obtained for austenitic steel. But for rear wall cracks the lifetimes are nearly identical. There are two effects responsible for this result:

- The irradiation creep data for the martensitic steel from [16]
 - measured at relatively high temperature (fig.13)- were extrapolated to the distinctly lower operation temperature using an activation energy of 3eV. So irradiation creep in the temperature range $300^{\circ}\text{C} < T < 450^{\circ}\text{C}$ becomes small and the martensitic structure is nearly unaffected by

irradiation creep. For this reason the high positive R-ratio remains almost constant in the rear wall part and crack growth is not delayed by an decreasing maximum stress intensity factor as found for SS316CW. From this point of view a better knowledge of irradiation creep in the range $300^{\circ}\text{C} < T < 450^{\circ}\text{C}$ is absolutely necessary.

- The unfavourable embrittlement data of the austenitic steel were employed for the martensitic steel too.

6. Summary

In this report lifetime results for a proposed first wall structure are presented. The aim was to show the general procedure for lifetime calculations, to demonstrate the principal behaviour of plasma facing structures, to explain the irradiation effects and to give a first idea of the expected lifetimes from the view point of fatigue.

The treatment of lifetime predictions for the first wall of a fusion reactor was outlined in case of an actual NET-design:

- Temperature distribution and elastic stresses due to thermal loading were calculated elastically by FE-methods assuming generalized plane strain.
- The change of stresses during operation caused by irradiation creep and swelling was considered.
- Cracks of different geometry were assumed to exist in the front and in the backward parts of the wall.
- Due to cyclic operation of the reactor cyclic stresses occur in the whole structure causing fatigue crack growth.
- Weighted averaged stress intensity factors were calculated using the weight function method for semi-elliptical surface cracks.
- Crack extension computations by means of a modified Forman equation allow to predict the time to failure.

The candidate materials, an austenitic (SS316 CW) and martensitic steel

(1.4914) are considered.

The results show a superiority of martensitic steel compared with austenitic steel due to the lower thermal expansion coefficient of martensitic steel.

All fracture mechanical failure calculations are strongly influenced by the irradiation embrittlement of the structural material. Whilst fracture toughness data are available for unirradiated and for thermal aged materials, data of irradiated materials are deduced indirectly from tensile test results. Here a source of error will remain as long as reliable K_{Ic} -measurements on irradiated material are not available.

Therefore the lifetimes calculated in this report should be considered as rather rough estimates.

Nevertheless the importance of influencing factors can be demonstrated by the parametric studies given here.

Figures

- Fig.1 First wall , geometric data
- Fig.2 Finite element meshes used in 2D and 3D calculations
- Fig.3 Temperature dependence of Young's moduli
- Fig.4 Temperature dependence of thermal conductivity
- Fig.5 Temperature dependence of the coefficient of thermal expansion
- Fig.6 Material data for $\text{Li}_{17}\text{Pb}_{83}$
- Fig.7 Temperature distribution at the end of plasma burn,
a) austenitic steel
b) martensitic steel
- Fig.8 Thermal stress distributions, austenitic steel, steady state
a) stresses in x- direction
b) stresses in z- direction
- Fig.9 Thermal stress distributions, martensitic steel, steady state
a) stresses in x- direction
b) stresses in z- direction
- Fig.10 Comparison of swelling formulas for SS316CW
- Fig.11 Literature data on irradiation creep for SS316CW
- Fig.12 Description of irradiation creep data by eqs.(16) and (17)
- Fig.13 Creep measurements on martensitic steel 1.4914 [16]
- Fig.14 Stress development at various locations of the wall
for SS316CW
- Fig.15 Stress distributions in the wall for an unshaded and
a 50% shaded neutron dose in the rear wall part (316CW)

- Fig.16 Influence of partially shaded neutron dose in the rear wall part on the stresses (SS316CW)
- Fig.17 Stresses at two locations for different swelling formulaes
- Fig.18 Stresses at two locations calculated with radiation creep laws eq.(16) and (17)
- Fig.19 Stress distribution in the wall for 1.4914
- Fig.20 Dose dependent stresses in the wall for 1.4914
- Fig.21 Cyclic stresses in the wall (SS316CW) due to cyclic reactor operation
- Fig.22 Model a real surface crack by a semi-elliptic crack
- Fig.23 Crack increments during crack extension
- Fig.24 Irradiation embrittlement for SS316CW concluded from tensile test data
a) dependencies proposed by ODETTE and FREY [23] and WOLFER and JONES [24]
b) comparison with eq.(42)
- Fig.25 Fatigue crack growth results for martensitic steels [25] compared with the results for SS316 [11]
- Fig.26 Development of a semi-circular surface crack situated at the plasma faced surface
- Fig.27 Influence of the embrittlement formulation on the maximum averaged stress intensity factor $K_{A \max}$ for SS316CW
- Fig.28 Influence of the crack depth on lifetime for SS316CW
- Fig.29 Influence of the initial aspect ratio a_i/c_i on life time for SS316CW
- Fig.30 Change of ellipticity during crack extension

Fig.31 Lifetime in dependence of the initial crack size a_i for cracks situated in the front and rear part of the first wall for SS316CW

Fig.32 Maximum K-values and normalized crack sizes for cracks in the front part (a) and cracks in the backward part (b) of the wall (SS316CW)

Fig.33 a) Lifetime diagramm for 1.4914
b) Comparison of lifetime data SS316CW/1.4914

Appendix A: Analytical temperature distribution

A1. Influence of surface heating

A1.1 The boundary value problem

Figure A1 shows a part of a first wall with internal cooling cannels. Because of the periodicity of channels only one segment must be considered as depicted in fig. A1b. If \dot{Q} is the heat flux at the wall surface and T_0 is the temperature of the cooling channel surface -assumed as constant- the steady-state temperature distribution in the wall is given by solution of the stationary heat conduction equation

$$\Delta T = \frac{\partial^2 T}{\partial x^2} + \frac{\partial^2 T}{\partial y^2} = 0 \quad (A1)$$

satisfying the boundary conditions

$$\frac{\partial T}{\partial y} = \dot{Q} \quad \text{for } y=0 \quad 0 \leq x \leq a \quad , \quad 1/\Lambda = \text{heat conductivity}$$

$$\frac{\partial T}{\partial y} = 0 \quad \text{for } y=b \quad 0 \leq x \leq a$$

$$\frac{\partial T}{\partial x} = 0 \quad \text{for } x=0 \quad 0 \leq y \leq b_1$$

$$x=a \quad 0 \leq y \leq b_1$$

$$x=0 \quad b_2 \leq y \leq b$$

$$x=a \quad b_2 \leq y \leq b$$

and

$$T = T_0 \quad \text{for } y=b_1 \quad 0 \leq x \leq a_1$$

$$y=b_1 \quad a_2 \leq x \leq a$$

$$y=b_2 \quad 0 \leq x \leq a_1$$

$$y=b_2 \quad a_2 \leq x \leq a$$

$$x=a_1 \quad b_1 \leq y \leq b_2$$

$$x=a_2 \quad b_1 \leq y \leq b_2$$

Since each constant temperature T_0 satisfies eq.(A1) automatically here only

only $T_0=0$ is taken into account. For simplifying the mixed boundary problem the element of periodicity is divided in three regions I, II, III as shown in fig.A1.

A1.2 Solution of the boundary value problem

A1.2.1 Solution in region I

The general procedure of solution is outlined in detail for region I. Here the boundary conditions are

$$\frac{\partial T}{\partial y} = \dot{Q}A \quad \text{for } y=0 \quad 0 \leq x \leq a \quad \text{I.1}$$

$$\frac{\partial T}{\partial x} = 0 \quad \text{for } x=0 \quad 0 \leq y \leq b_1 \quad \text{I.2}$$

$$x=a \quad 0 \leq y \leq b_1$$

$$T=0 \quad \text{for } y=b_1 \quad 0 \leq x \leq a_1 \quad \text{I.3}$$

$$y=b_1 \quad a_2 \leq x \leq a \quad \text{I.4}$$

$$T \neq 0 \quad \text{for } y=b_1 \quad a_1 < x < a_2$$

The unknown temperature distribution at $y=b_1$ is described by a Fourier power series with unknown coefficients. Equation (A1) can be solved by insertion the usual set up

$$T(x,y) = U(x) \cdot V(y) \quad \text{(A2)}$$

Inserting eq.(A2) into eq.(A1) yields

$$\frac{1}{U} \frac{\partial^2 U}{\partial x^2} = - \frac{1}{V} \frac{\partial^2 V}{\partial y^2} = -m^2 \quad \text{(A3)}$$

As the left-hand side is not dependent on y and the right-hand side does not depend on x , both sides must equal to be a constant ($-m^2$).

From boundary condition (I.2) follows

$$U = C \cos m_v x \quad m_v = 2v\pi/a \quad v = \text{integer} \quad \text{(A4)}$$

From the right-hand side of eq.(A3) it results

$$\frac{\partial^2 V}{\partial y^2} - m^2 V = 0$$

From the boundary condition (I.1)

$$V_m = A_v \cosh my \tag{A5}$$

can be derived.

The v-th solution can be written

$$T_v = A_v \cosh(m_v y) \cos(m_v x)$$

and from the symmetry and boundary conditions it follows for $m=0$

$$T = -\Lambda \dot{Q} y \tag{A6}$$

and

$$T = \text{const.} = \gamma \tag{A7}$$

The general solution is found to be

$$T = \gamma - \Lambda \dot{Q} y + \sum_{v=1}^{\infty} A_v \cosh(m_v y) \cos(m_v x) \tag{A8}$$

A1.2.2 Solution in region II

The boundary conditions in region II are

$$\begin{array}{lll} T=0 & \text{for } x=a_1 & b_1 \leq y \leq b_2 \\ & x=a_2 & b_1 \leq y \leq b_2 \end{array} \quad \text{II.1}$$

$$T=T(x, b_1) \quad \text{for } a_1 \leq x \leq a_2 \quad \text{II.2}$$

$$T=T(x, b_2) \quad \text{for } a_1 \leq x \leq a_2 \quad \text{II.3}$$

This Dirichlet boundary problem is treated in [A1]. With the abbreviation

$$\alpha_n = (2n-1)\pi / (a_2 - a_1)$$

the result can be written

$$T = \sum_{n=1}^{\infty} (B_n \sinh \alpha_n (b_2 - y) + C_n \sinh \alpha_n (y - b_1)) \sin \alpha_n (x - a_1) \quad (A9)$$

$$B_n = \frac{2}{a_2 - a_1} [\sinh \alpha_n (b_2 - b_1)]^{-1} \int_{a_1}^{a_2} T(x, b_1) \sin \alpha_n (x - a_1) dx \quad (A10)$$

$$C_n = \frac{2}{a_2 - a_1} [\sinh \alpha_n (b_2 - b_1)]^{-1} \int_{a_1}^{a_2} T(x, b_2) \sin \alpha_n (x - a_1) dx$$

A1.2.3 Solution in region III

The mixed boundary value problem is described by

$$\frac{\partial T}{\partial y} = 0 \quad \text{for} \quad y=b \quad 0 \leq x \leq a \quad \text{III.1}$$

$$\frac{\partial T}{\partial x} = 0 \quad \text{for} \quad \begin{array}{l} x=0 \quad b_2 \leq x \leq b \\ x=a \quad b_2 \leq x \leq b \end{array} \quad \text{III.2}$$

$$T(x, b_2) = \begin{cases} 0 & \text{for} \quad 0 \leq x \leq a_1 \quad a_2 \leq x \leq a \\ f(x) & \text{for} \quad a_1 \leq x \leq a_2 \end{cases}$$

By use of a similar procedure as outlined in A1.2.1 it yields

$$T = \sum_{v=0}^{\infty} D_v \cosh m_v (b - y) \cos m_v x \quad (A11)$$

with

$$D_v = \frac{2}{a} [\cosh m_v (b - b_2)]^{-1} \int_0^a T(x, b_2) \cos m_v x dx \quad (A12)$$

A1.3 Determination of the Fourier coefficients

Because of the conditions of continuity for the temperatures T and their first derivatives $\partial T / \partial y$ at the boundaries $y=b_1$ and $y=b_2$ four relations between the unknown Fourier coefficients are given and all coefficients A_v ,

B_n, C_n, D_v are evaluable. A detailed representation is only outlined for boundary $y=b_1$. At this line it holds

$$T(x, b_1) = \sum_{\mu=0}^{\infty} A_{\mu} \cosh m_{\mu} b_1 \cos m_{\mu} x = \begin{cases} \sum_{n=1}^{\infty} B_n \sinh \alpha_n (b_2 - b_1) \sin \alpha_n (x - a_1) & \text{for } a_1 < x < a_2 \\ 0 & \text{else} \end{cases} \quad (A13)$$

Multiplying both sides by $\cos(m_{\nu} x)$ and integration from $x=0$ to $x=a$ yields

$$A_{\nu} \cosh m_{\nu} b_1 \int_0^a (\cos m_{\nu} x)^2 dx = \sum_{n=1}^{\infty} B_n \sinh \alpha_n (b_2 - b_1) \lambda_{n\nu} \quad (A14)$$

with the abbreviation

$$\lambda_{n\nu} = \int_{a_1}^{a_2} \sin \alpha_n (x - a_1) \cos m_{\nu} x dx = \begin{cases} \frac{2}{\pi} \left[\left(\frac{2n-1}{a_2 - a_1} \right)^2 - \left(\frac{2n}{a} \right)^2 \right]^{-1} \frac{2n-1}{a_2 - a_1} \cos m_{\nu} a_1 \\ -\frac{1}{2} (a_2 - a_1) \sin m_{\nu} a_1 & \text{if } \frac{2n-1}{a_2 - a_1} = \frac{2\nu}{a} \end{cases} \quad (A15)$$

For a fixed given n the coefficients A_{ν} result

$$A_{n\nu} = \frac{\delta}{a} B_n [\cosh m_{\nu} b_1]^{-1} \sinh \alpha_n (b_2 - b_1) \lambda_{n\nu} \quad A_{\nu} = \sum_n A_{n\nu} \quad (A16)$$

where

$$\delta = \begin{cases} 1 & \text{for } \nu=0 \\ 2 & \text{for } \nu>0 \end{cases}$$

From the derivative in the interval $a_1 \leq x \leq a_2$ one obtains

$$\begin{aligned} \frac{\partial T}{\partial y}(b_1) &= -\Lambda Q + \sum_{\nu=1}^{\infty} A_{\nu} m_{\nu} \sinh m_{\nu} b_1 \cos m_{\nu} x = \\ &= \sum_{n=1}^{\infty} [-B_n \alpha_n \cosh \alpha_n (b_2 - b_1) + C_n \alpha_n] \sin \alpha_n (x - a_1) \end{aligned} \quad (A17)$$

Multiplying eq.(A17) by $\sin \alpha_n(x-a_1)$ and integration from $x=a_1$ to $x=a_2$ yields

$$C_n = B_n \cosh \alpha_n(b_2-b_1) - \frac{2\Lambda\dot{Q}}{2n-1} (\lambda_{nv}/a^2) + \sum_{v=1}^{\infty} A_{nv} \frac{4v}{2n-1} \frac{\lambda_{vn}}{a} \sinh m_v b_1 \quad (A18)$$

Introducing eq.(A16)

$$C_n = B_n \left[\cosh \alpha_n(b_2-b_1) + \frac{8}{(2n-1)a^2} \sinh \alpha_n(b_2-b_1) \sum_{v=1}^{\infty} v \tanh m_v b_1 \lambda_{vn}^2 \right] - \frac{2\Lambda\dot{Q}}{(2n-1)\pi} \quad (A19)$$

By similar calculations at the boundary line $y=b_2$ one can conclude

$$B_n = C_n \left[\cosh \alpha_n(b_2-b_1) + \frac{8}{(2n-1)a^2} \sinh \alpha_n(b_2-b_1) \sum_{v=1}^{\infty} v \tanh m_v(b-b_1) \lambda_{vn}^2 \right] \quad (A20)$$

and

$$D_{nv} = \frac{\delta}{a} C_n [\cosh m_v(b-b_2)]^{-1} \sinh \alpha_n(b_2-b_1) \lambda_{nv} \quad D_v = \sum_n D_{nv} \quad (A21)$$

Combination of eqs.(A19) and (A20) yields

$$B_n = - \frac{2\Lambda\dot{Q}}{(2n-1)\pi} \lambda_{n0} \{ [\cosh \alpha_n(b_2-b_1) + K_n]^{-1} - \cosh \alpha_n(b_2-b_1) - L_n \}^{-1} \quad (A22)$$

$$K_n = \frac{8}{(2n-1)a^2} \sinh \alpha_n(b_2-b_1) \sum_{v=1}^{\infty} v \lambda_{nv}^2 \tanh m_v(b-b_1)$$

$$L_n = \frac{8}{(2n-1)a^2} \sinh \alpha_n(b_2-b_1) \sum_{v=1}^{\infty} v \lambda_{nv}^2 \tanh m_v b_1$$

The coefficients C_n can be evaluated from eq.(A20), the A_v from eq.(A16) and the D_v from eq.(A21). Figure A2 shows the stationary temperature distribution for T_0 , $a_1=0.2$, $a_2=0.8$, $a=1$, $b_1=0.4$, $b_2=0.8$ and $b=1$.

A1.4 Plate with slot shaped cooling channels

A simplified first wall construction with slot shaped cooling channels at the back side is shown in fig.A3a . Figure A3b describes an element of periodicity which is divided in two regions I and II as shown in fig.A3c. Similar treatment as given in I1.2 and I1.3 yields eq.(A8) and

$$T = \sum_{n=1}^{\infty} B_n \cosh \alpha_n (b-y) \sin \alpha_n (x-a_1) \quad (A23)$$

where

$$B_n = \frac{2\Lambda\dot{Q}}{(2n-1)\pi} \lambda_{0n} \left[\sinh \alpha_n (b-b_1) + \frac{8}{(2n-1)a^2} \cosh \alpha_n (b-b_1) \sum_{v=1}^{\infty} v \lambda_{nv}^2 \tanh \alpha_v b_1 \right]^{-1} \quad (A24)$$

The temperature distribution resulting from eqs.(A8), (A23) and (A23) is depicted in fig.A4 .

A1.5 Plate with rear cooling channels

A further simplification is given in fig.5 where cooling pipes are welded on the back side of the first wall. In this case it results eq.(A8) with

$$A_{\nu} = \frac{a\Lambda\dot{Q}}{2\pi} \lambda_{0n} \left[\cosh m_{\nu} b_1 \right]^{-1} \sum_{n=1}^{\infty} \lambda_{nv} \left(\sum_{v=1}^{\infty} v \lambda_{nv}^2 \tanh m_{\nu} b_1 \right)^{-1} \quad (A25)$$

The accompanying temperature distribution is plotted in fig. A6.

A2. Contributions of volumetric heating

If W is the density of heat production caused by volumetric heat sources and

$$\dot{q} = \dot{W}/\lambda = \dot{W}\Lambda \quad (A26)$$

the stationary heat conduction equation can be written

$$\Delta T + \dot{q} = 0 \quad (A27)$$

This Poisson equation has to be solved for a boundary value problem as described in fig. A7. By introducing

$$T_i = \dot{q}(C_0 + C_1 x + C_2 x^2 + C_3 y + C_4 y^2 + C_5 xy) \quad (A28)$$

into (A27) it can be verified that (A28) is a particular solution of eq. (A27). From symmetry and boundary conditions follows

$$C_2 + C_4 = -\frac{1}{2} \text{ and} \quad (A29)$$

$$\text{and } C_5 = 0 \quad (A30)$$

Solutions of the homogeneous differential equation are given in Section A1.2

A2.1 Solution for region I

In region I the boundary conditions are

$$\left. \frac{\partial T}{\partial y} \right|_{y=0} = \left. \frac{\partial T}{\partial x} \right|_{x=0} = \left. \frac{\partial T}{\partial x} \right|_{x=a/2} = 0 \quad (A31)$$

The constants of eq.(A28) are determined from

$$\begin{aligned} \left. \frac{\partial T}{\partial y} \right|_{y=0} &= 0 \quad \rightarrow \quad C_3 = 0 \\ \left. \frac{\partial T}{\partial y} \right|_{x=0} &= 0 \quad \rightarrow \quad C_1 = 0 \\ \left. \frac{\partial T}{\partial y} \right|_{x=a/2} &= 0 \quad \rightarrow \quad C_2 = 0 \end{aligned} \quad (A32)$$

and the total solution has the form

$$T = q (C_0 - \frac{1}{2}y^2) + \sum_{v=1}^{\infty} \tilde{A}_v \cos m_v x \cosh m_v y \quad (A33)$$

where

$$C_0 = \frac{1}{2} b^2 + \frac{1}{qa} \int_0^a T(x, b_1) dx \quad (A34)$$

$$\tilde{A}_{v>0} = \frac{2}{a} (\cosh m_v b_1)^{-1} \int_0^a T(x, b_1) \cos m_v x dx \quad (A35)$$

A2.2 Solution for region II

In this case the boundary conditions are given by

$$\left. \frac{\partial T}{\partial x} \right|_{x=a/2} = T \Big|_{x=a_1} = 0 \quad (\text{A36})$$

They are satisfied by homogeneous solutions similar to eq.(A9). The constants of the inhomogeneous solutions become

$$\left. \frac{\partial T}{\partial x} \right|_{x=a/2} = 0 \quad \rightarrow \quad C_1 = -C_2 a \quad (\text{A37})$$

$$T \Big|_{x=a_1} = 0 \quad \rightarrow \quad C_3 = C_4 = 0 \quad , \quad C_0 = -\frac{1}{2} a_1 a_2$$

The total solution in region II is written

$$T = \frac{1}{2} \dot{q} (ax - a_1 a_2 - x^2) + \sum_{n=1}^{\infty} T_n \quad (\text{A38})$$

$$T_n = (B_n \sinh \alpha_n (b_2 - y) + C_n \sinh \alpha_n (x - b_1)) \sin \alpha_n (x - a_1)$$

with

$$\tilde{B}_n = \frac{2}{a_2 - a_1} [\sinh \alpha_n (b_2 - b_1)]^{-1} \int_{a_1}^{a_2} [T(x, b_1) - \frac{1}{2} q (ax - a_1 a_2 - x^2)] \sin \alpha_n (x - a_1) dx \quad (\text{A39})$$

and

$$\tilde{C}_n = \frac{2}{a_2 - a_1} [\sinh \alpha_n (b_2 - b_1)]^{-1} \int_{a_1}^{a_2} [T(x, b_2) - \frac{1}{2} q (ax - a_1 a_2 - x^2)] \sin \alpha_n (x - a_1) dx \quad (\text{A40})$$

A2.3 Solution for region III

This region is described by

$$\left. \frac{\partial T}{\partial x} \right|_{x=0} = \left. \frac{\partial T}{\partial x} \right|_{x=a/2} = \left. \frac{\partial T}{\partial y} \right|_{y=b} = 0 \quad (\text{A41})$$

The coefficients of eq.(A28) become

$$\left. \frac{\partial T}{\partial x} \right|_{x=0} = 0 \quad \rightarrow \quad C_1 = 0 \quad (\text{A42})$$

$$\left. \frac{\partial T}{\partial x} \right|_{x=a/2} = 0 \quad \rightarrow \quad C_2 = 0$$

$$\left. \frac{\partial T}{\partial y} \right|_{y=b} = 0 \quad \rightarrow \quad C_3 = -2bC_4 = b$$

consequently, the total solution is given by

$$T = \dot{q} (C_0 + by - \frac{1}{2}y^2) + \sum_{v=1}^{\infty} T_v \quad (A43)$$

$$T_{v>0} = \tilde{D}_v \cosh m_v (b-y) \cos m_v x$$

where

$$C_0 = \frac{1}{2}b^2_2 - bb_2 + \frac{1}{aq} \int_0^a T(x, b_2) dx \quad (A44)$$

and

$$\tilde{D}_v = \frac{2}{a} [\cosh \alpha_v (b-b_2)]^{-1} \int_0^a T(x, b_2) \cos \alpha_v x dx \quad (A45)$$

The unknown coefficients $\tilde{A}_v, \tilde{B}_n, \tilde{C}_n, \tilde{D}_v$ can be determined in the same way as mentioned in section I1.3 .

A3. First wall with rear connected cooling channels

As an example the special case of a first wall with connected cooling channels at the rear part (fig.A8) is considered.

The solution of this problem is given by adding (A8) and (A33). The coefficients A_v are given in eq.(A25) and substituting ΛQ by qb_1

$$\tilde{A}_v = \frac{aqb_1 \lambda_{0n}}{2\pi} (\cosh \alpha_v b_1)^{-1} \sum_{n=1}^{\infty} \lambda_{nv} \left(\sum_{v=1}^{\infty} v \lambda_{nv}^2 \tanh \alpha_v b_1 \right)^{-1} \quad (A46)$$

follows.

In fig.A9 the isothermal lines for pure surface heat flux and pure volumetric heating are represented for $a_1=0.4$, $a_2=0.6$ and $a=1$.

For first wall constructions exposed to surface heat flux and volumetric heat sources due to neutron radiation the stationary temperature distribution can be computed by superposition of solutions for each heat source.

A4. Approximative relations for maximum temperature

The highest temperatures occur at the wall surface ($y=0, x= a/2$). Figure 10 shows the temperature T_{\max} normalized on $\frac{1}{2}Wb^2_1 \Lambda$ in case of pure volumetric heating for the structure shown in fig.A9 for different values

of $2a_1/a$ and b_1/a . The curves can be approximated by

$$T_{\max} \approx \frac{\dot{W}}{2\lambda} b_1^2 \left[1 + \left(0.35 \frac{a}{b_1} + 0.25 \left(\frac{a}{b_1} \right)^2 \right) \left(1 - \frac{2a_1}{a} \right)^2 \right] \quad (\text{A47})$$

In case of pure surface heat flux same calculations depicted in fig.A11 yield

$$T_{\max} \approx \frac{\dot{Q}}{\lambda} b_1 \left[1 + \left(0.177 \frac{a}{b_1} + 0.12 \left(\frac{a}{b_1} \right)^2 \right) \left(1 - \frac{2a_1}{a} \right)^2 \right] \quad (\text{A48})$$

In addition the maximum temperatures were computed in case of pure surface heat flux for two other geometries represented in fig.A12. Because the deviations of the results were less than 2% the curves plotted in fig.A12 represent both cases and one can write

$$T_{\max} \approx \frac{\dot{Q}}{\lambda} b_1 \left[1 + \left(0.0775 \frac{aB}{b_1} + 0.052 \left(\frac{aB}{b_1} \right)^2 \right) \left(1 - \frac{2a_1}{a} \right)^2 \right] \quad (\text{A49})$$

Appendix B

Influence of geometric shape on temperature and stress distribution

In this appendix results of temperature and stress calculations for different geometric First Wall shapes are presented. Stresses are mainly influenced by the thickness d of the FW front side and the thickness c of the FW rear side. So, besides the reference geometry

case 1 ($d= 8\text{mm}$, $c = 5\text{mm}$),

the combinations

case 2 ($d= 5\text{mm}$, $c = 5\text{mm}$),

case 3 ($d= 8\text{mm}$, $c = 8\text{mm}$),

case 4 ($d= 5\text{mm}$, $c = 8\text{mm}$),

have been considered.

Results for temperature distributions, distributions of stress fields σ_{xx} and σ_{zz} are given in contour plots in figs.B1-B3 for austenitic steel and in figs.B4-B6 for martensitic steel, respectively. Stresses in y-direction are of an amount of 10% up to 15% of that in the other directions and therefore not plotted.

In table 3 for austenitic and martensitic steel and the four different geometries maximum and minimum values are summarized. This table shows that stresses are decreasing with decreasing thickness d of the front plate and with increasing thickness c of rear side. So the best combination with respect to a minimization of thermal stresses is case 4.

Next the curvature radius R has been modified. The variation of $\sigma_{xx}(R)$ is shown in fig.B7 . A range of R from 0 to 6mm causes a range in σ of less than 11% . In y and z direction the deviation is at the most 15 and 7 MPa, respectively. The most suitable case is $R=2\text{mm}$, where $\sigma_{xx,\text{max}}=(504\text{MPa}/-463\text{MPa})$. On the other hand, $R= 6\text{mm}$ leads to $\sigma_{xx,\text{max}}=(601/-459\text{MPa})$ and $R=0$ results in $\sigma_{xx,\text{max}}=(517/-459\text{MPa})$. Although there is a change in the stresses for varying R , the influence is negligible in comparison to an improvement in stresses, which is available by broadening the FW behind the cooling channels.

Figures

Fig. A1 First wall element with inner cooling channels affected by surface heat flux

Fig. A2 Normalized stationary temperature distribution in a first wall with inner cooling channels for surface heating

Fig. A3 First wall element with slot shaped cooling channels affected by surface heat flux

Fig. A4 Normalized stationary temperature distribution in a first wall with slot shaped cooling channels for surface heating

Fig. A5 First wall element with rear connected cooling channels affected by surface heating

Fig. A6 Normalized stationary temperature distribution in a first wall with rear connected cooling channels for surface heating

Fig. A7 First wall element with inner cooling channels affected by volumetric heating

Fig. A8 First wall element with rear connected cooling channels affected by volumetric heating

Fig. A9 Isotherms in a first wall with rear connected cooling channels for volumetric heating

Fig. A10 Maximum temperature for the structure of fig. A8 for different geometrical portions (volumetric heating)

Fig. A11 Maximum temperature in a first wall element with rear connected cooling channels for several geometrical proportions (surface heating)

Fig. A12 Maximum temperature in a first wall with inner channels and slot shaped channels, respectively (surface heating)

Fig. B1 Contour plots of temperature distributions for austenitic steel (cases 2,3,4)

Fig. B2 Contour plots of thermal stress distributions σ_{xx} for austenitic steel (cases 2,3,4)

Fig. B3 Contour plots of thermal stress distributions σ_{zz} for austenitic steel (cases 2,3,4)

Fig. B4 Contour plots of temperature distributions for martensitic steel (cases 2,3,4)

Fig. B5 Contour plots of thermal stress distributions σ_{xx} for martensitic steel (cases 2,3,4)

Fig. B6 Contour plots of thermal stress distributions σ_{zz} for martensitic steel (cases 2,3,4)

Fig. B7 Maximum tensile stresses in x-direction versus curvature radius R

References

- [1] R.F. Mattas, D.L. Smith, "Model for life-limiting properties of fusion reactor structural materials," Nuclear Technology, 38(1978), 186-198.
- [2] W. Daenner, "Results of strategic calculations for optimizing the first wall life in a tokamak fusion reactor," Transact. 6th Intern. Conf. on Struct. Mech. in Reactor Techn., Paris, Aug. 1981, paper N4/1.
- [3] R.W. Watson, R.R. Peterson, W.G. Wolfer, "Lifetime analysis of fusion reactor first wall components," Transact. of the ASME, Journ. of Pressure Vessel Technology, 105(1983), 144-152.
- [4] A.O. Adegbulugbe, "Comparison of lifetime calculation for fusion reactor first walls based on two creep-fatigue design criteria," Nuclear Engineering and Design/Fusion 1(1984), 301-305.
- [5] T. Fett, A. Müller, D. Munz, H. Stamm, "Stress distribution and fatigue crack growth in pressurized tubes including the effect of swelling and radiation creep", in Fusion Technology 1984, Vol. 2, Proceedings of the 13 th SOFT 1984, 973-978.
- [6] T. Fett, D. Munz, "Stress and lifetime calculations for first wall and blanket structural components," Part I: Crack propagation in tubes, KfK 3875, 1985.
- [7] G. Vieider, W. Daenner, B. Haverkamp, "Design concepts for NET first wall and blankets", in Fusion Technology 1984, Vol. 2, Proceedings of the 13 th SOFT 1984, 1363-1368.
- [8] G. Vieider, A. Cardella, "Estimated thermal fatigue limits for the first wall of NET", Proceedings of the IAEA Technical Committee Meeting on Lifetime Predictions for the First Wall and Blanket Structure of Fusion Reactors, 5-7. Nov.1985, Karlsruhe, 149-150.
- [9] - ADINAT , ADINA Engineering, Inc., Waterton, Mass.; Report AE 81-1 (Sept. 1981)

- [10]- ADINA , ADINA Engineering, Inc., Watertown, Mass.; Report AE 81-2 (Sept. 1981)
- [11] R.D. Watson, "The impact of inelastic deformation, radiation effects, and fatigue damage on fusion reactor first wall lifetime", Thesis, University of Wisconsin, 1981, UWFDM-460.
- [12] T.Horie, T. Aruga, N. Miki, A. Minato, M. Seki, K. Shiraishi, S. Tsujimura, T. Watanabe, T. Tone , "An analytical and experimental study on lifetime predictions for fusion reactor first walls and divertor plates", Proceedings of the IAEA-TCM on Lifetime Predictions for the First Wall and Blanket Structure of Fusion Reactors, Karlsruhe, 5-7 November 1985, 107-133.
- [13] K. Ehrlich, "Irradiations creep and interrelation with swelling in austenitic stainless steels", Journ. of Nuclear Materials 100(1981), 149-166.
- [14] E.R. Gilbert, J.F. Bates , "Dependence of irradiation creep on temperature and atom displacements in 20% cold worked type 316 stainless steel", Journ. of Nuclear Materials 65(1977),204-209.
- [15] L.C. Walters, G.L. McVay, G.D. Hudman, in: Proc. Intern. Conf. on Radiation Effects in Breeder Reactor Structural Materials, Scottsdale, AZ, 1977, Eds. M.L. Bleiberg and J.W. Bennet, 277-294.
- [16] K. Ehrlich, private communication
- [17] H. Th. Klippel, B. van der Schaaf, W. van Witzenburg, "Thermal shock effects on type 316L austenitic steel and vanadium base alloys", Proceedings of the IAEA-TCM on Lifetime Predictions for the First Wall and Blanket Structure of Fusion Reactors, Karlsruhe, 5-7 November 1985, 59-70.
- [18] T.A. Cruse, P.M. Besuner, "Residual life prediction for surface cracks in complex structural details", Journal of Aircraft, 12(1975), 369-375.

- [19] C. Mattheck, P. Morawietz, D. Munz, "Stress intensity factor at the deepest point of a semi-elliptical surface crack in plates under stress gradients", Int. Journ. of Fracture 23(1983),201-212.
- [20] T. Fett, H. Stamm, "Berechnung gewichtet gemittelter Spannungsintensitätsfaktoren für den halbelliptischen Oberflächenriß", Primärbericht 03.01.01P47A ,KfK, Karlsruhe,1986.
- [21] J.C. Newman, I.S. Raju, "An empirical stress-intensity factor equation for the surface crack", Engng. Fract. Mech.,15(1981),185-192.
- [22] M.O. Speidel, "Fatigue crack growth at high temperatures," Proceedings of the Symposium on high-temperature materials in gas turbines, Baden, Switzerland, 207-251,1974.
- [23] G.R. Odette, D. Frey, "Development of mechanical property correlation methodology for fusion environments," Journal of Nuclear Materials 85,86 (1979), 817-822.
- [24] W.G. Wolfer, R.H. Jones, "Flow and fracture of alloys in the fusion environment," University of Wisconsin Report UWFDM-429 (August 1981) .
- [25] H. Ehrlich, private communication
- [26] F. Görner, C. Mattheck, D. Munz, " Change in geometry of surface cracks during alternating tension and bending," Z. Werkstofftech. 14 (1983), 11-18.

F I G U R E S

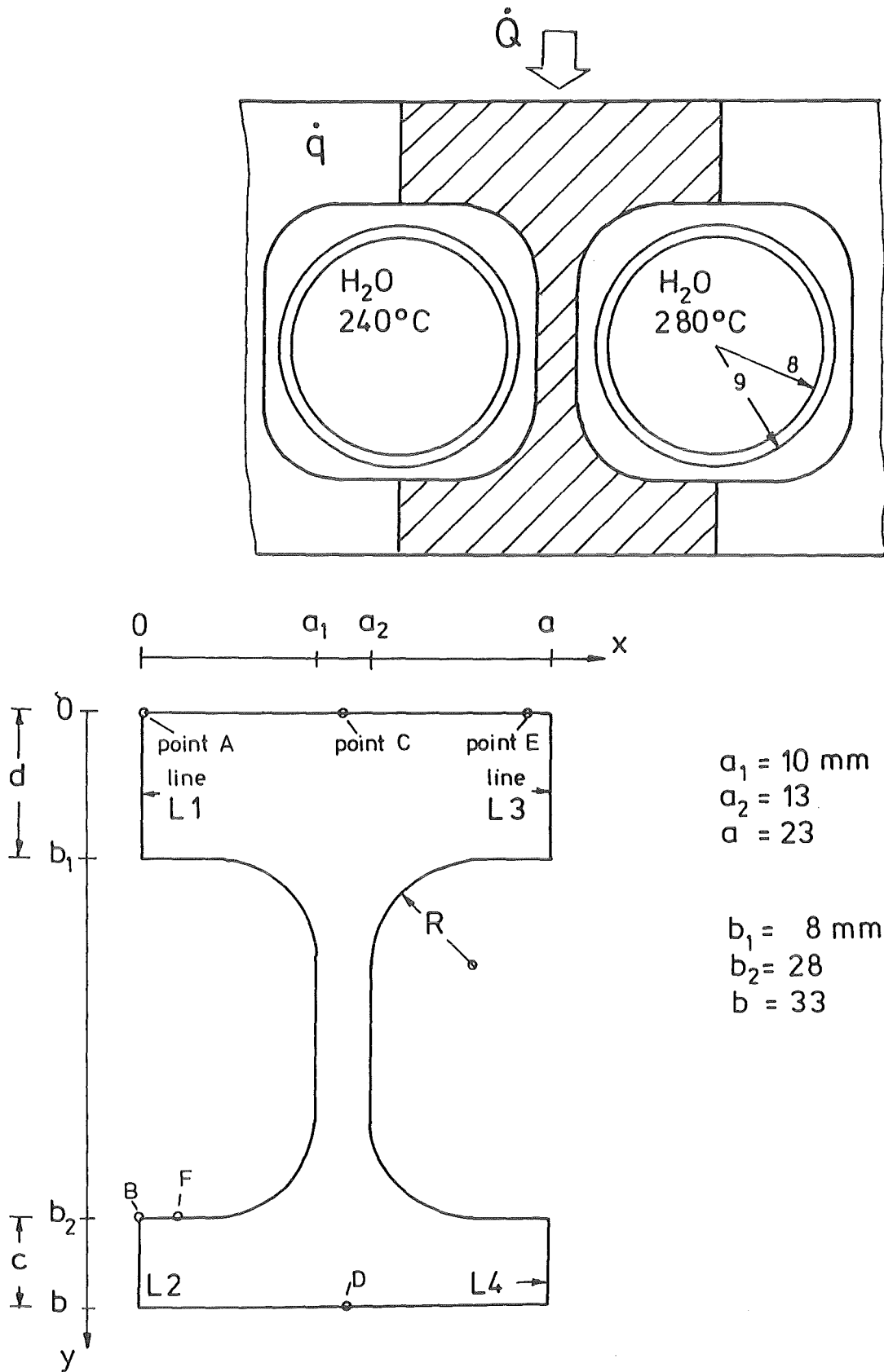


Fig.1 First wall , geometric data

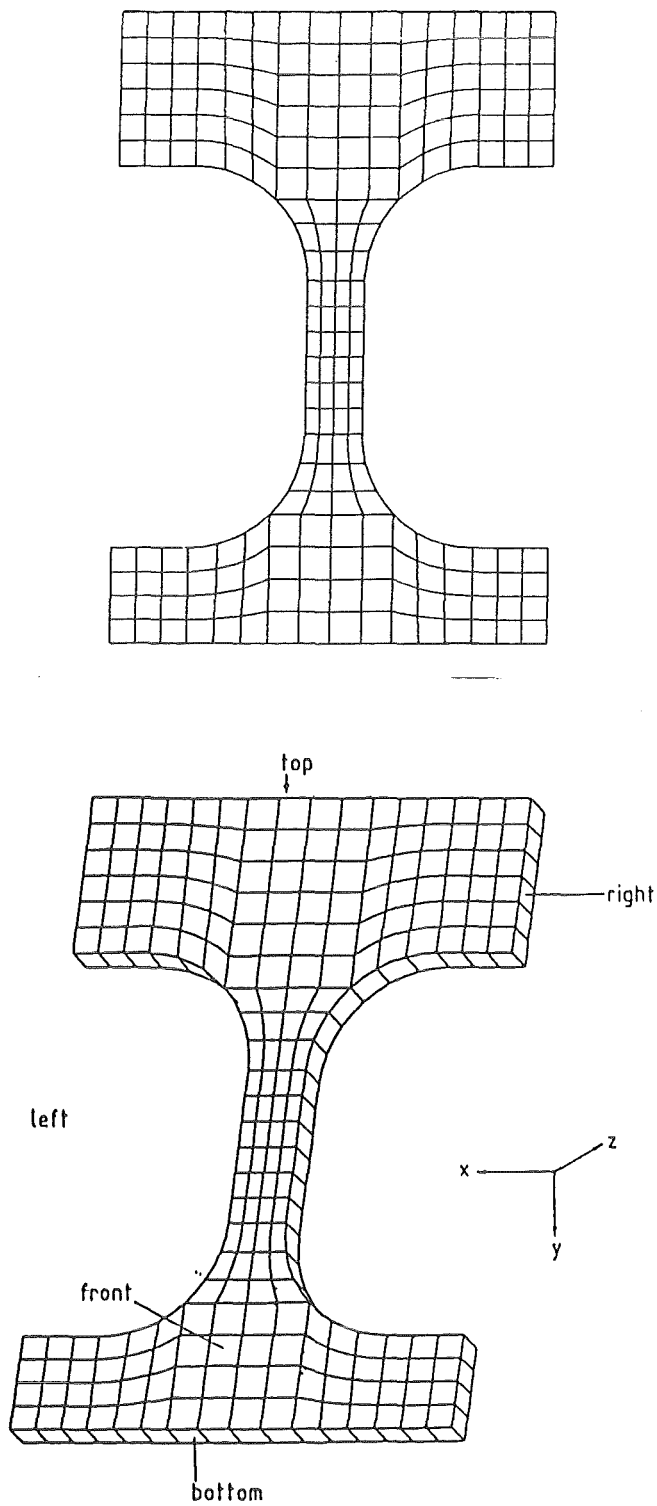


Fig.2 Finite element meshes used in 2D and 3D calculations

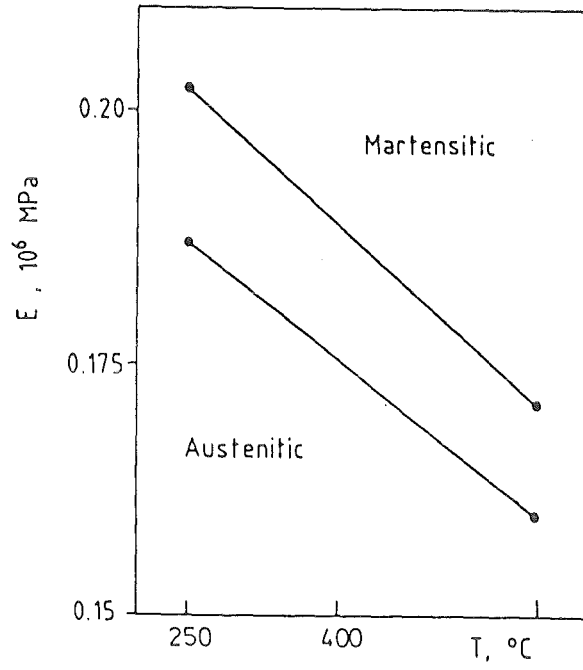


Fig.3 Temperature dependence of Young's moduli

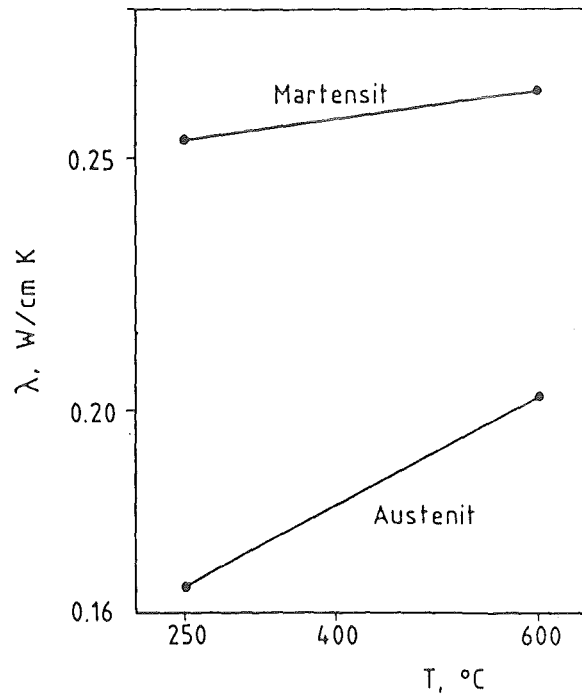


Fig.4 Temperature dependence of thermal conductivity

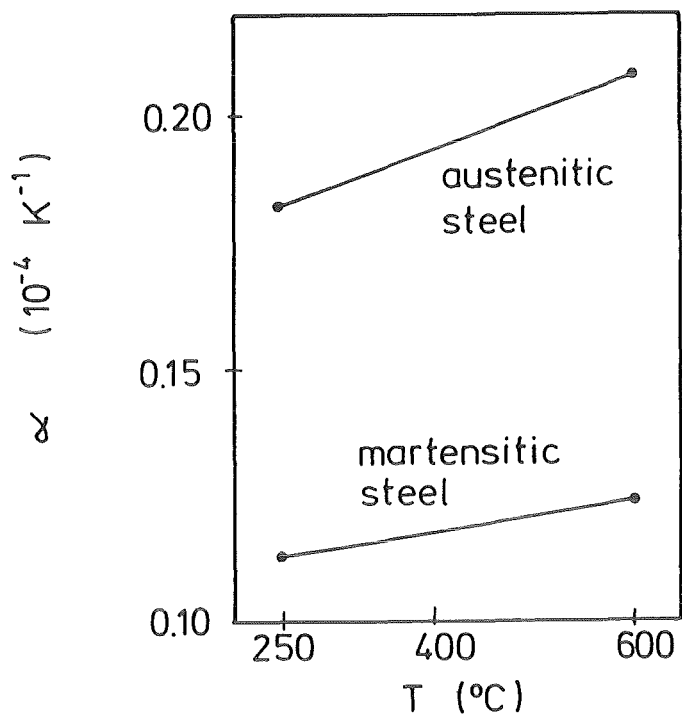


Fig.5 Temperature dependence of the coefficient of thermal expansion

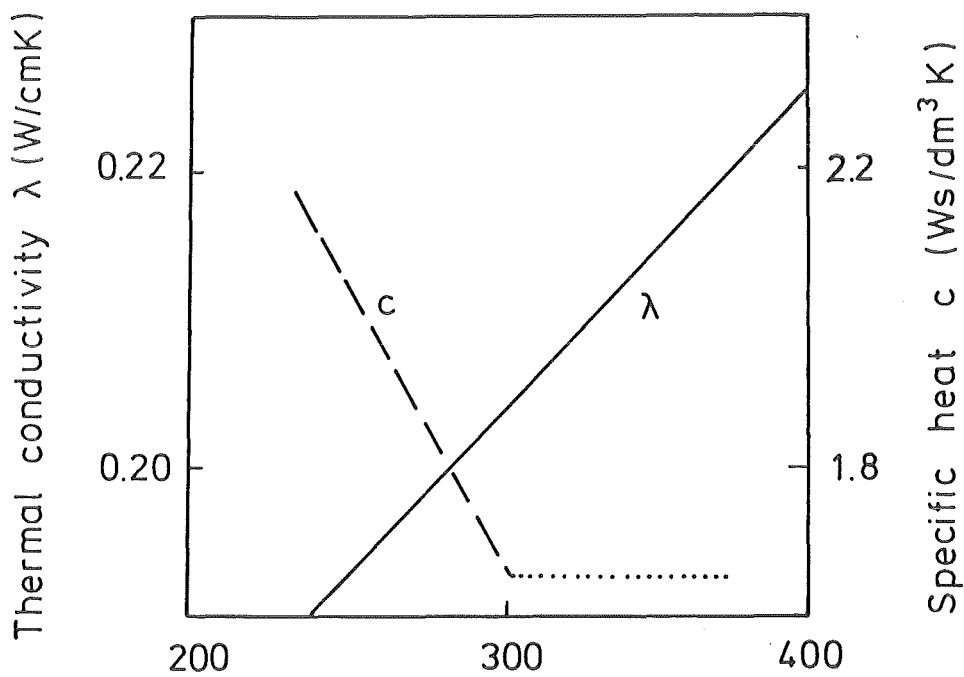


Fig.6 Material data for $\text{Li}_{17}\text{Pb}_{83}$

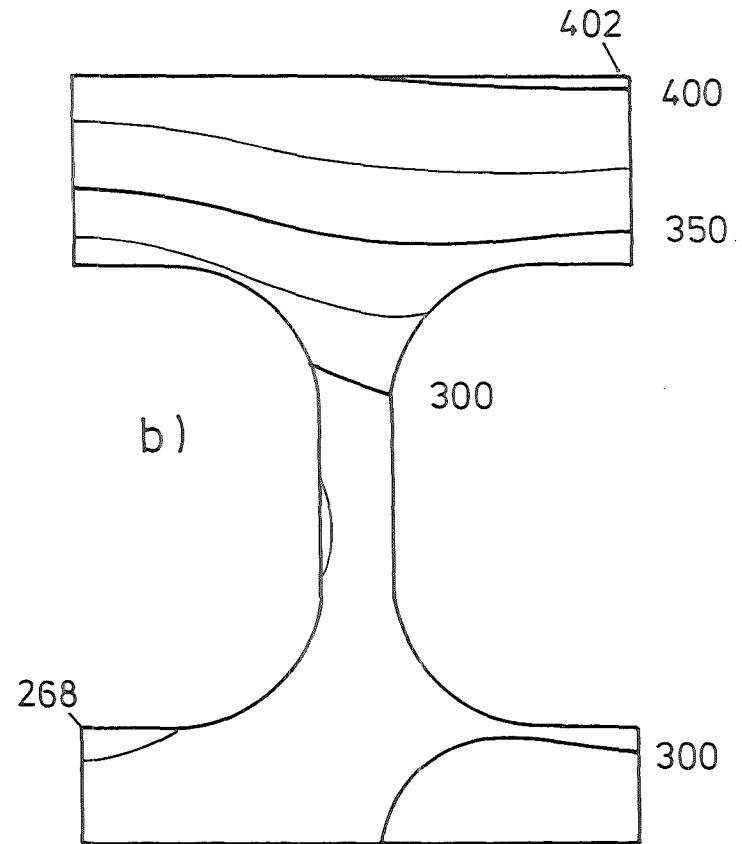
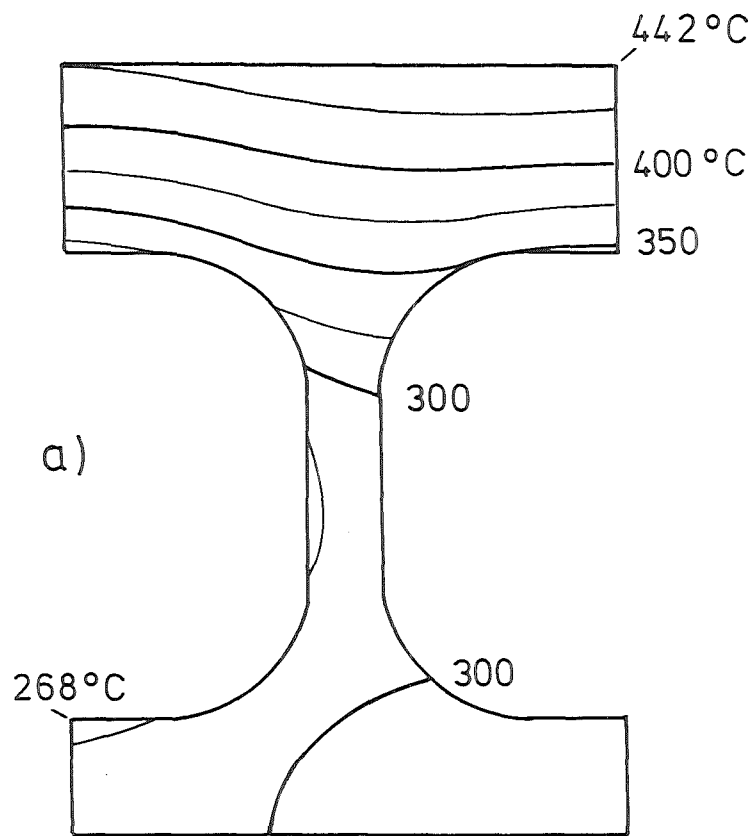


Fig.7 Temperature distribution at the end of plasma burn,
 a) austenitic steel
 b) martensitic steel

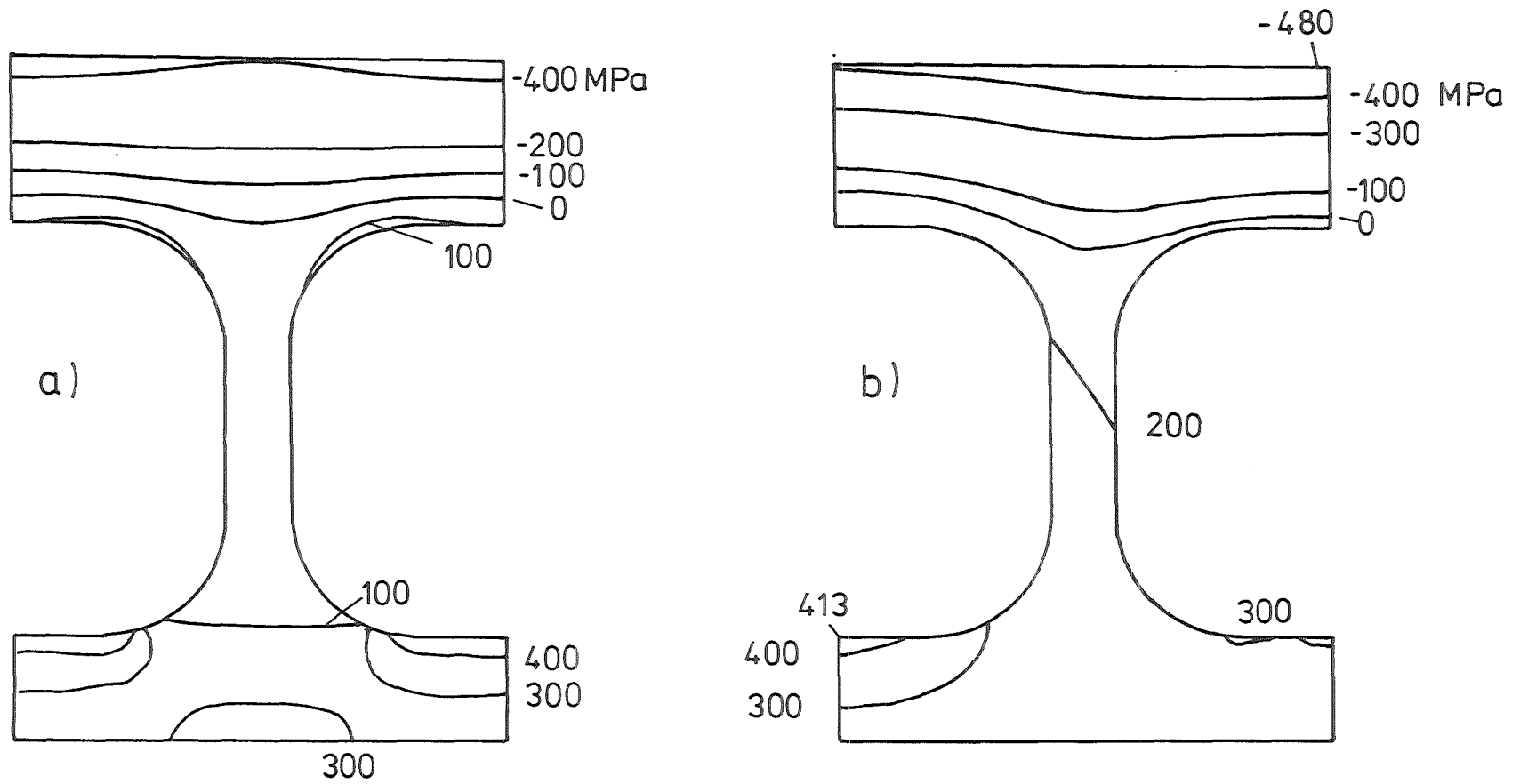


Fig.8 Thermal stress distributions, austenitic steel, steady state
 a) stresses in x- direction
 b) stresses in z- direction

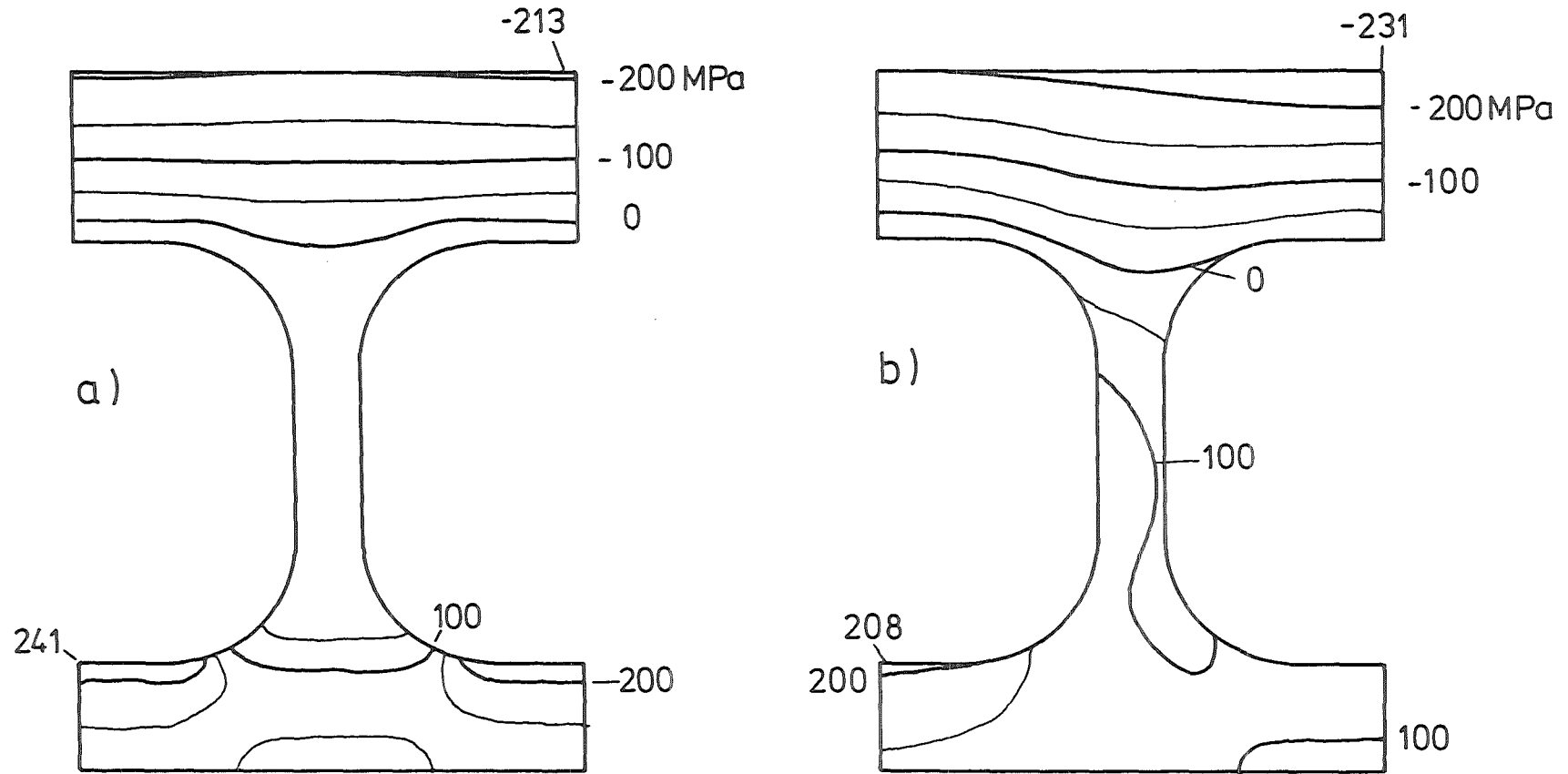


Fig.9 Thermal stress distributions, martensitic steel, steady state
 a) stresses in x- direction
 b) stresses in z- direction

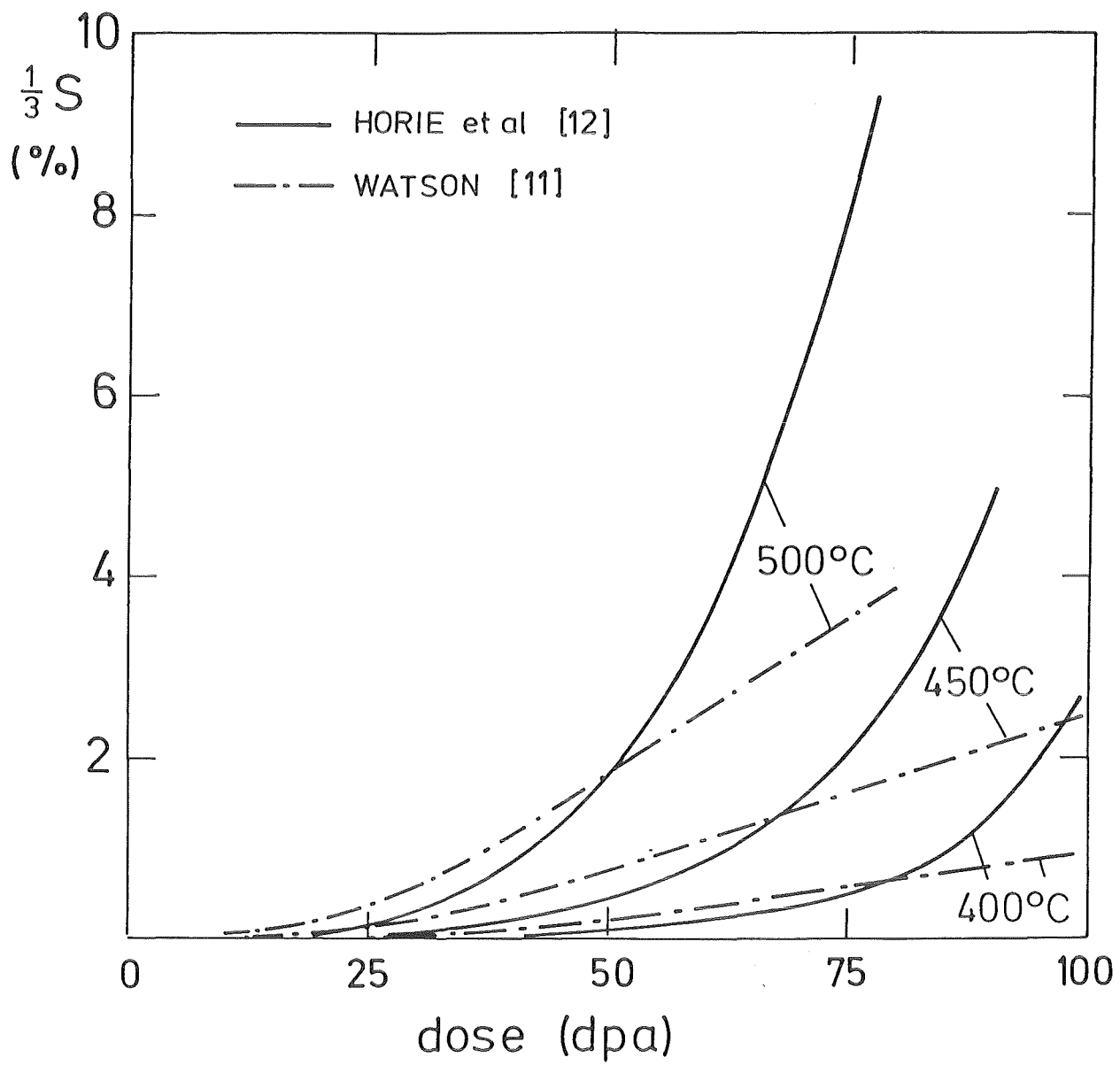


Fig.10 Comparison of swelling formulas for SS316CW

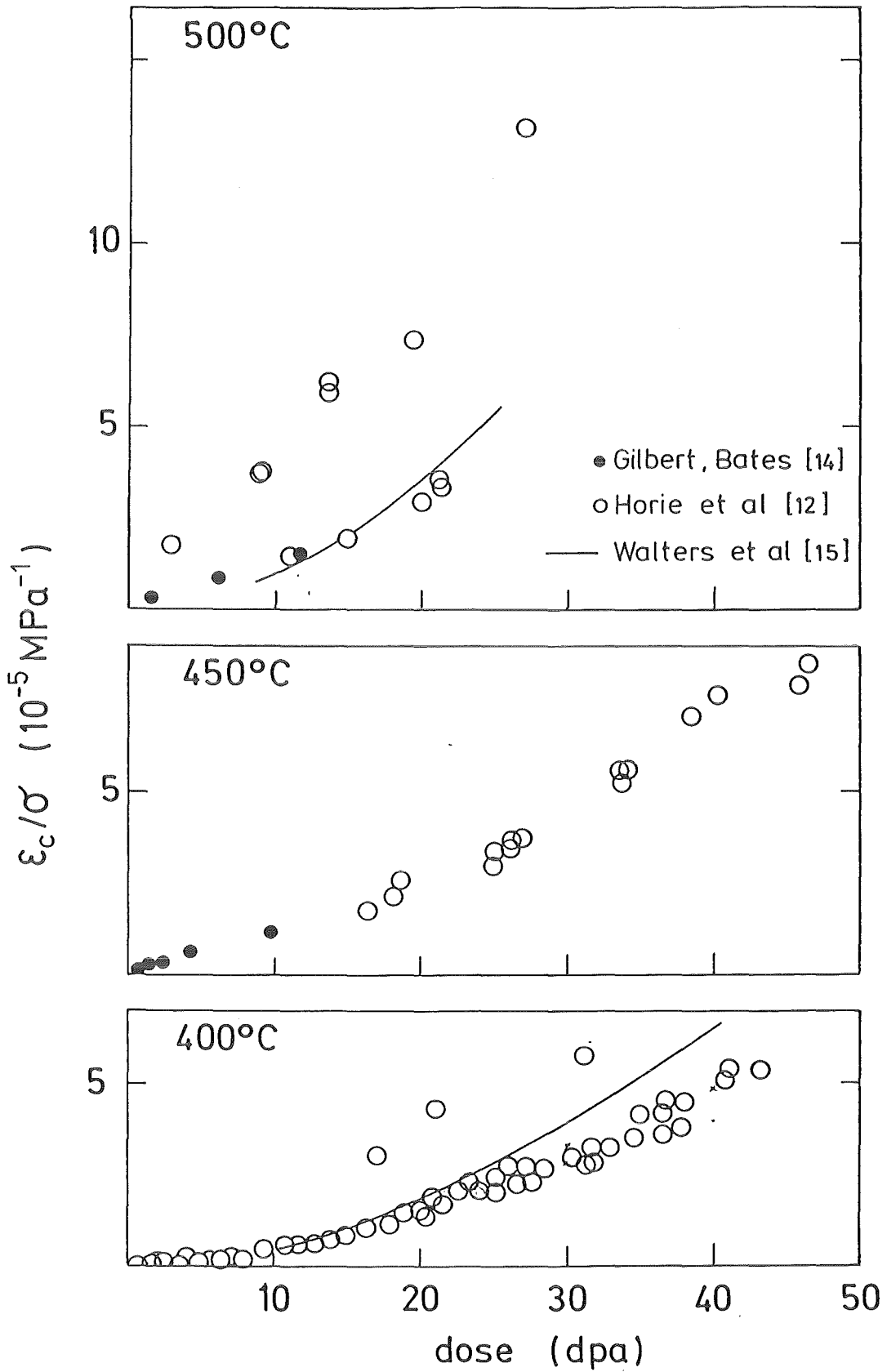


Fig.11 Literature data on irradiation creep for SS316CW

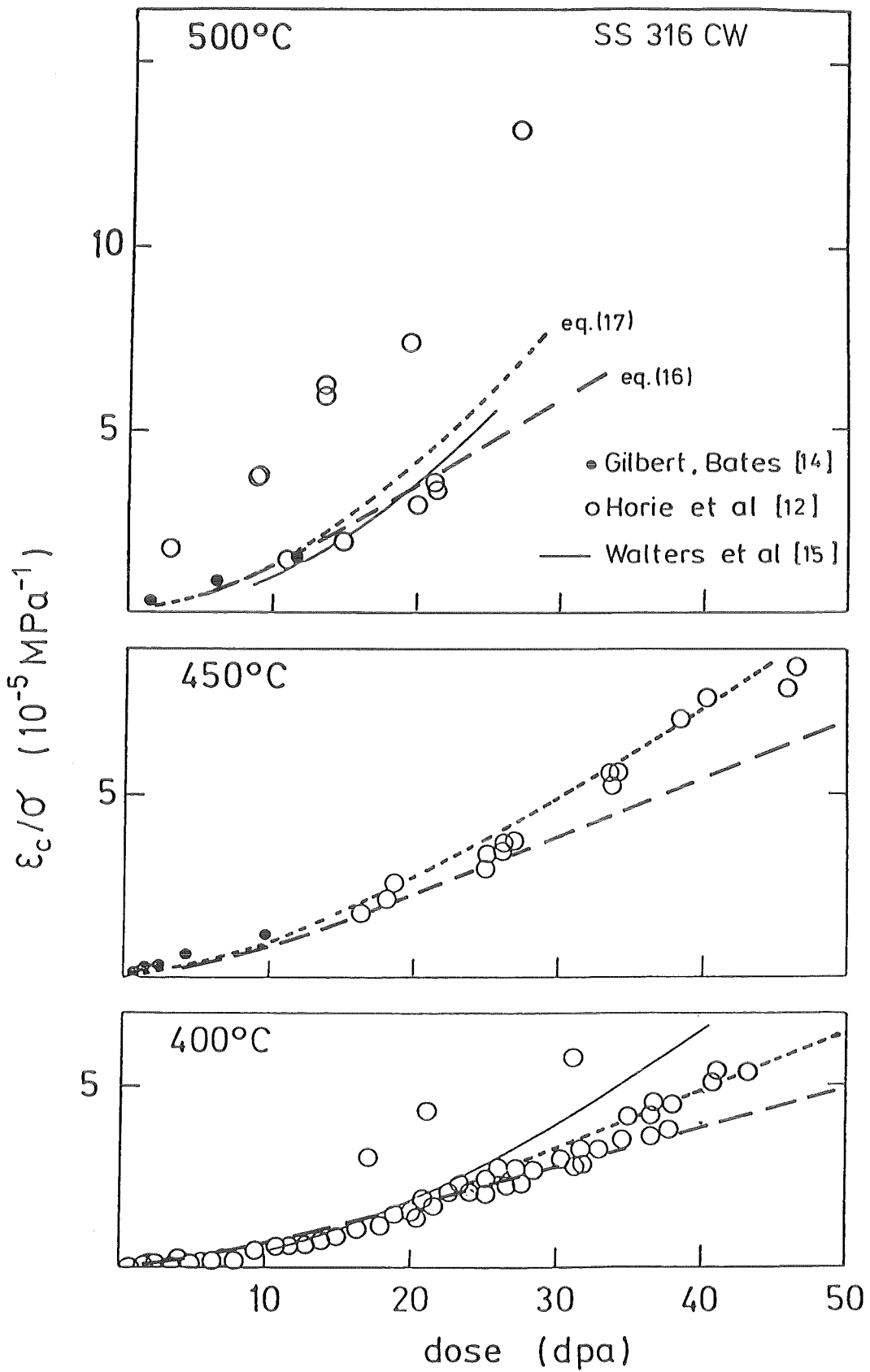


Fig.12 Description of irradiation creep data by eqs.(16) and (17)

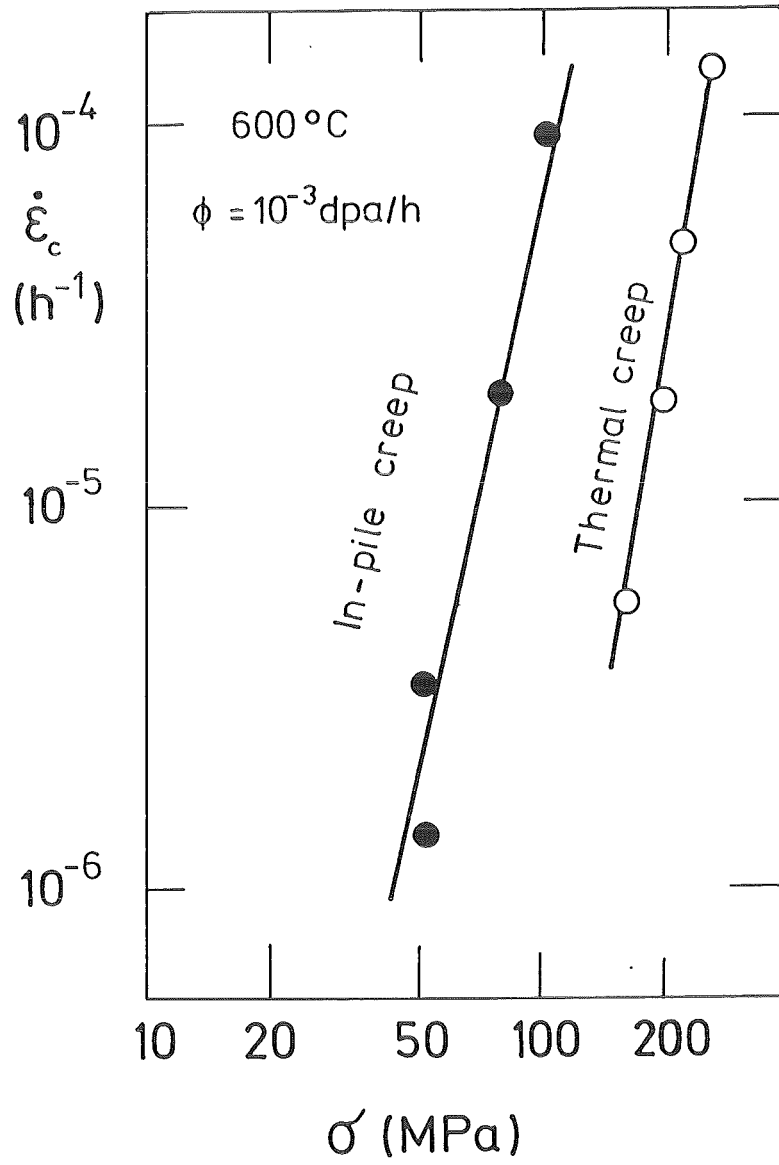


Fig.13 Creep measurements on martensitic steel 1.4914 [16]

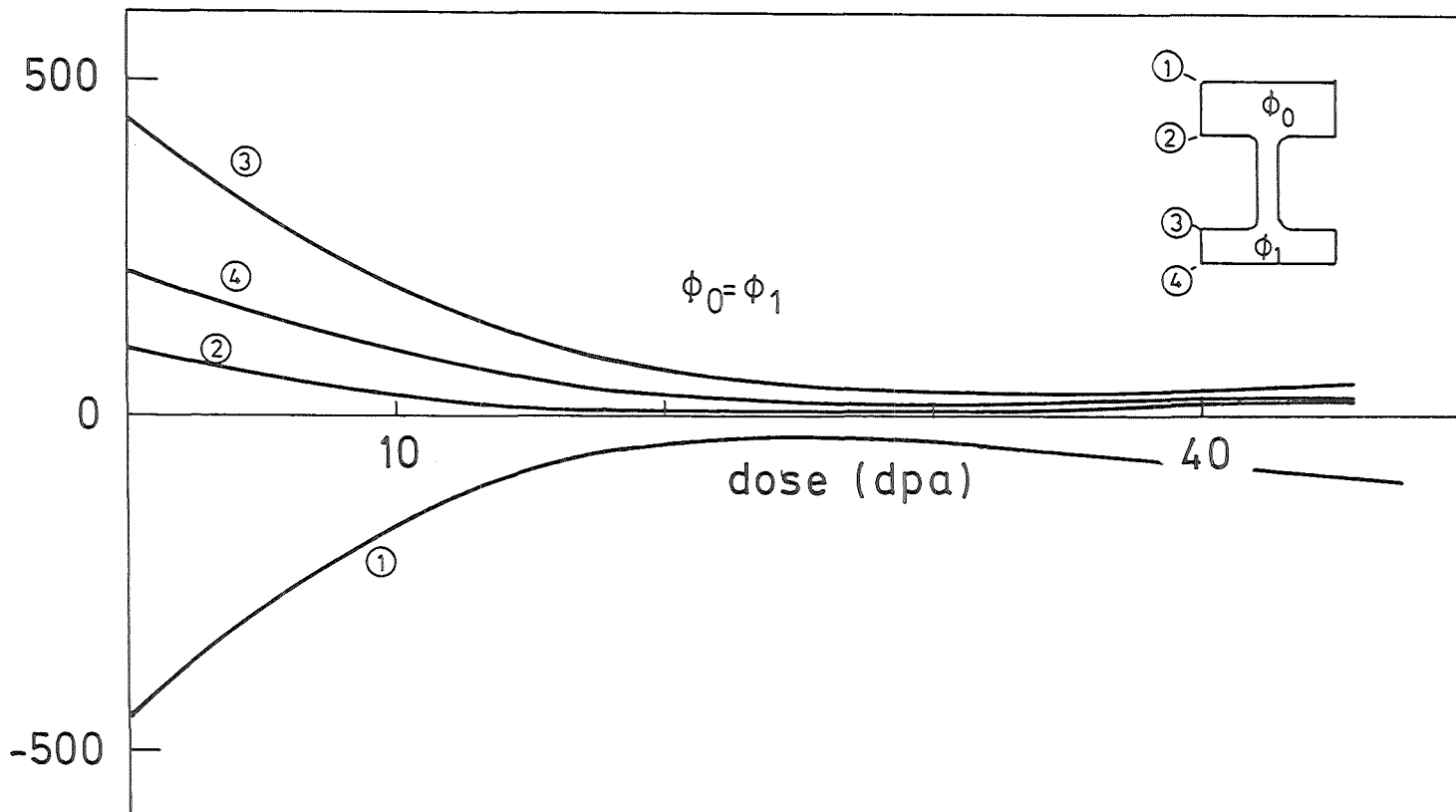


Fig.14 Stress development at various locations of the wall
for SS316CW

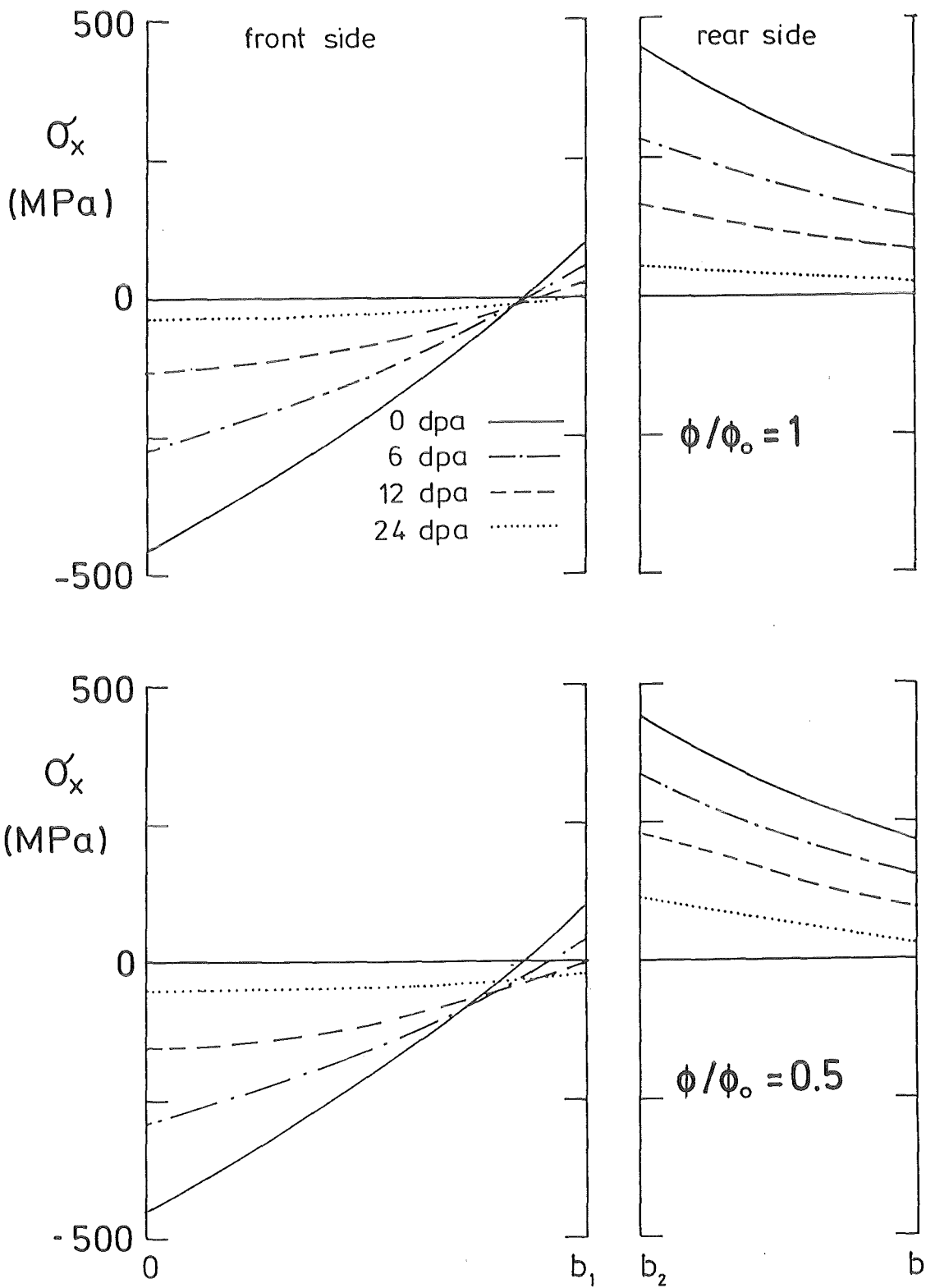


Fig.15 Stress distributions in the wall for an unshaded and a 50% shaded neutron dose in the rear wall part (316CW)

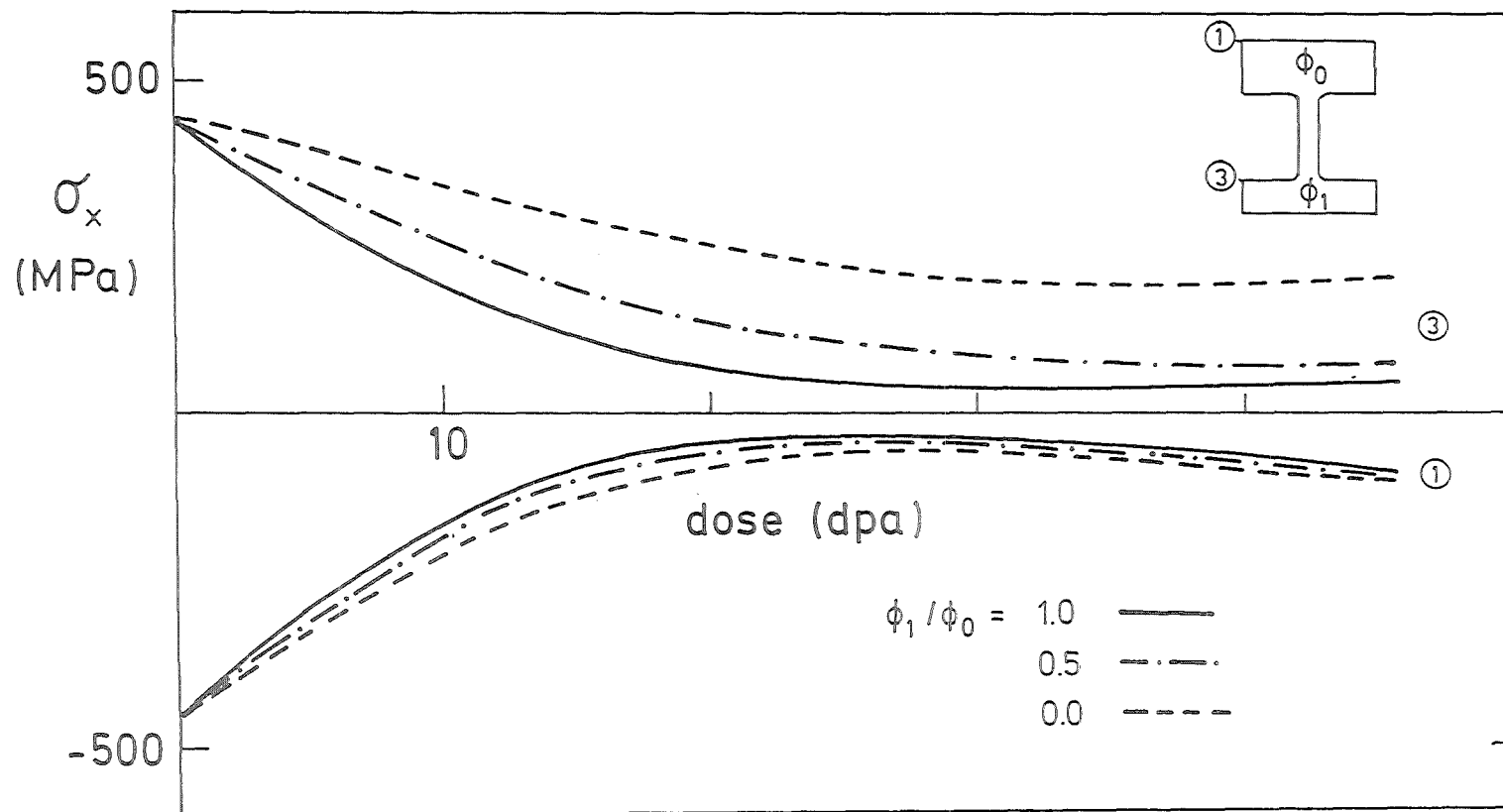


Fig.16 Influence of partially shaded neutron dose in the rear wall part on the stresses (SS316CW)

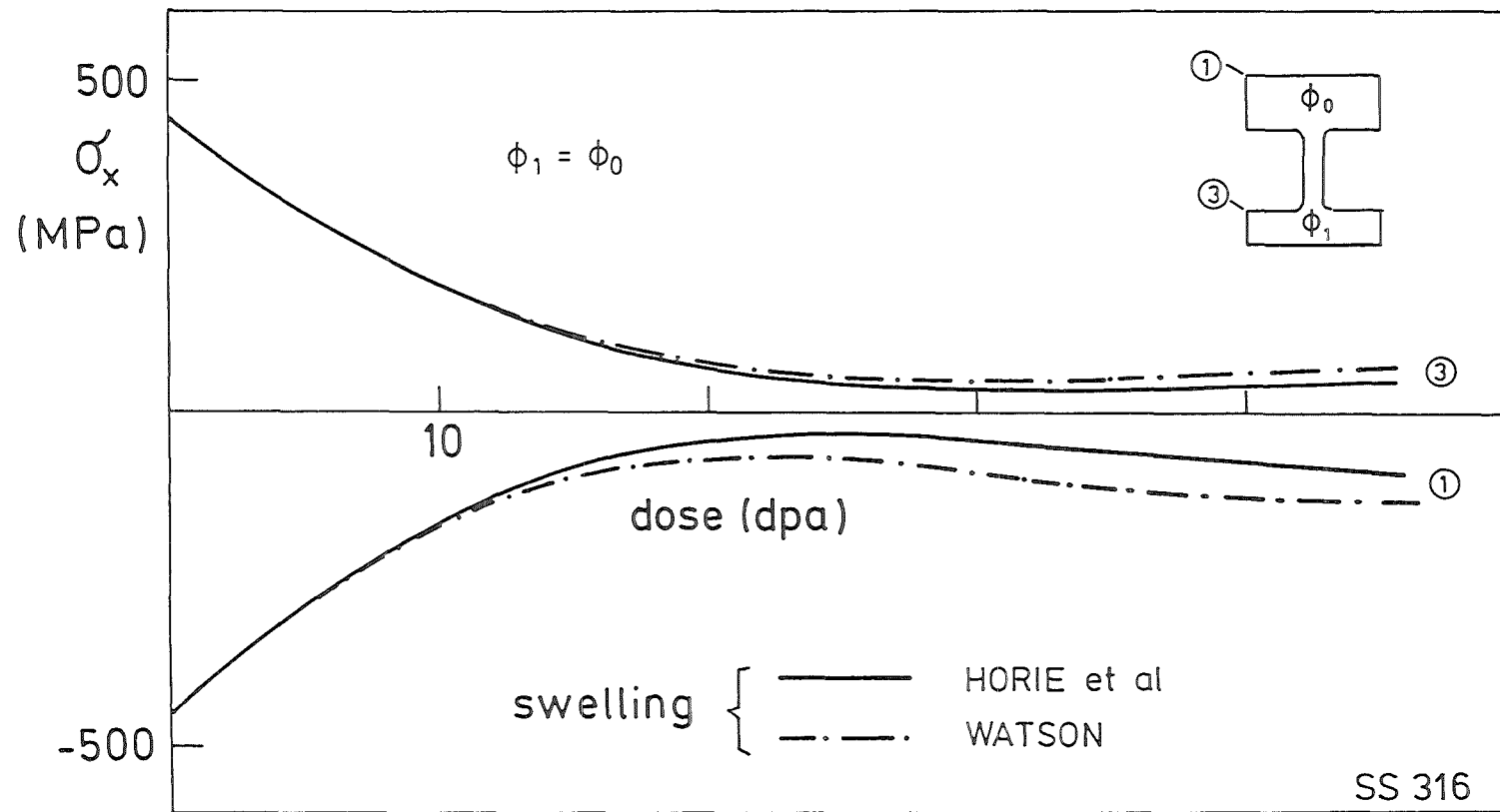


Fig.17 Stresses at two locations for different swelling formulaes

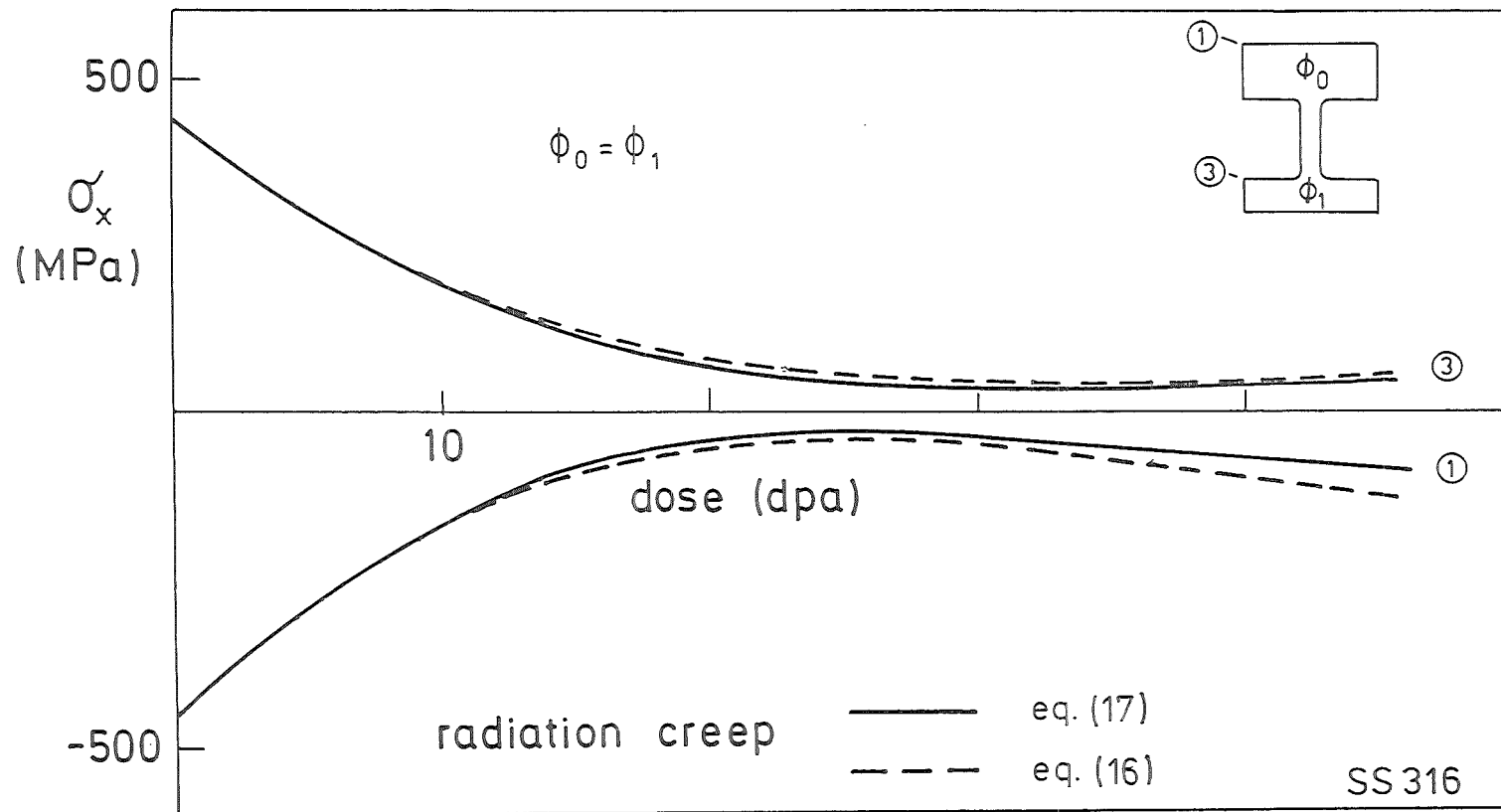


Fig.18 Stresses at two locations calculated with radiation creep laws eq.(16) and (17)

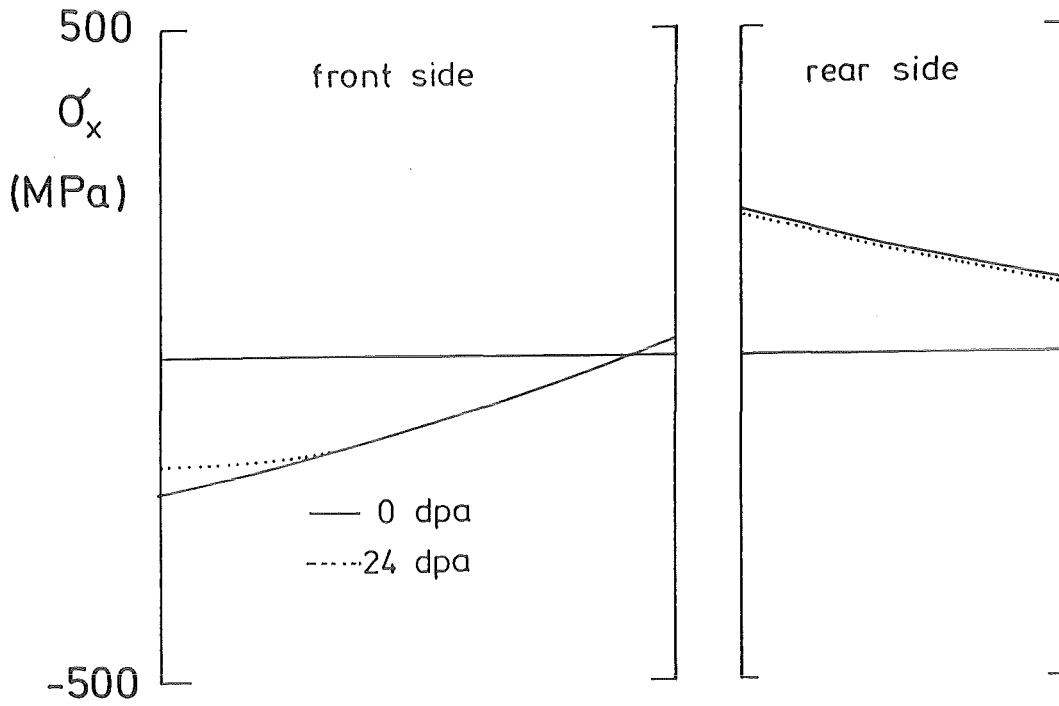


Fig.19 Stress distribution in the wall for 1.4914

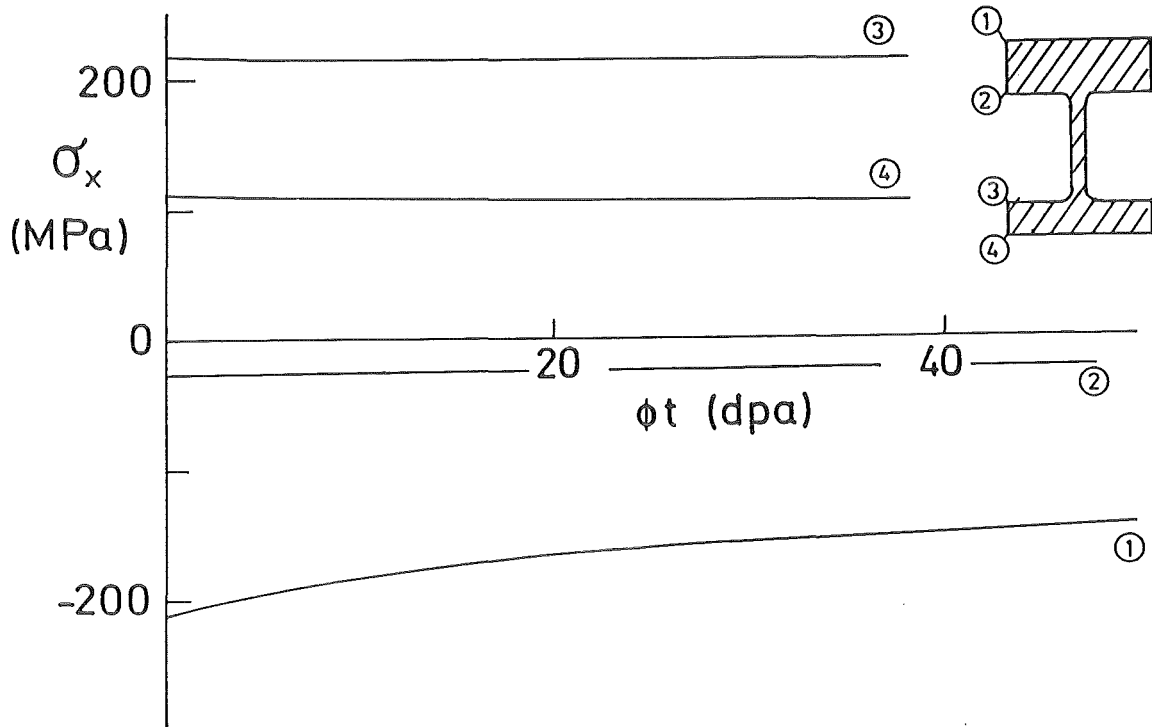


Fig.20 Dose dependent stresses in the wall for 1.4914

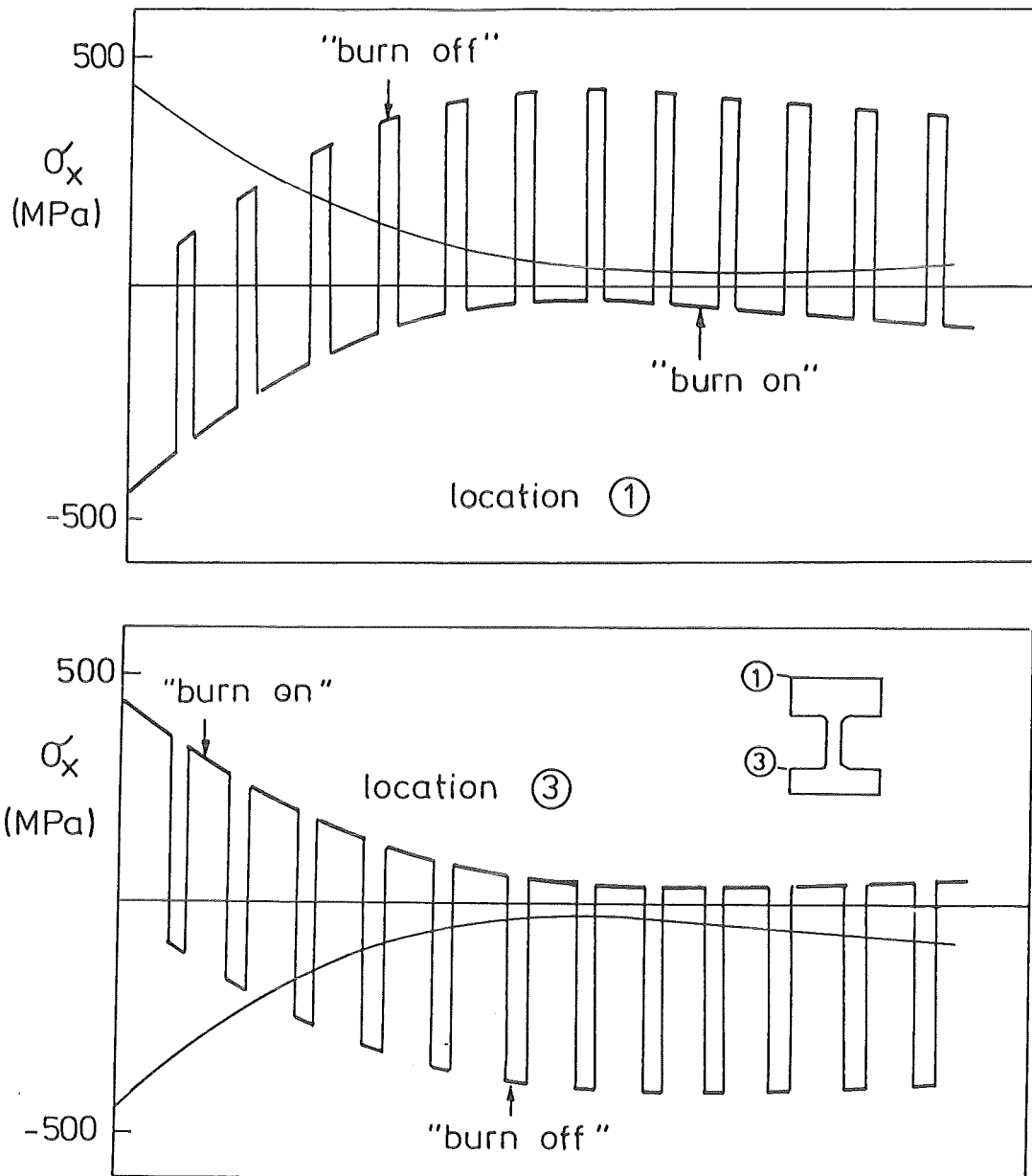


Fig.21 Cyclic stresses in the wall (SS316CW) due to cyclic reactor operation

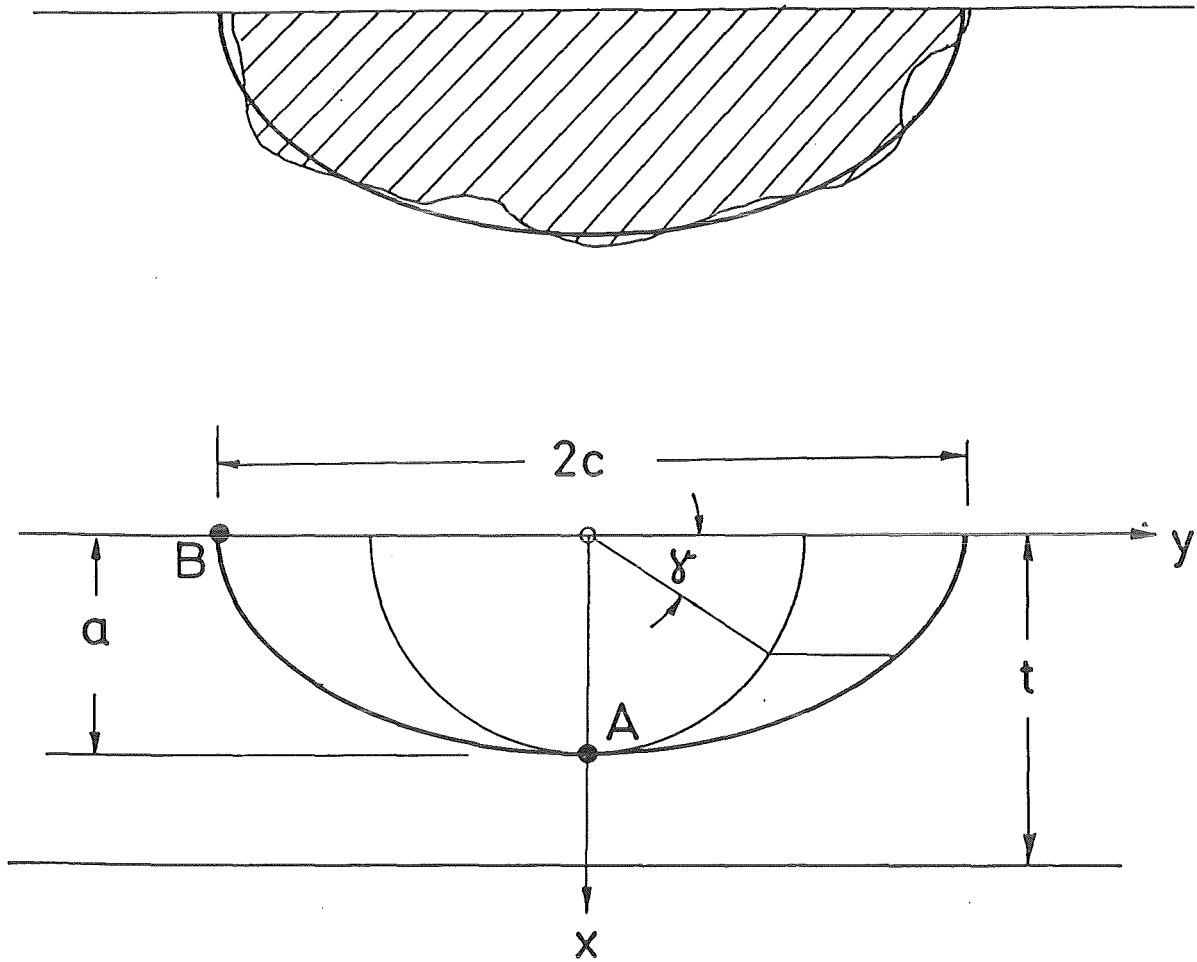


Fig.22 Model a real surface crack by a semi-elliptic crack

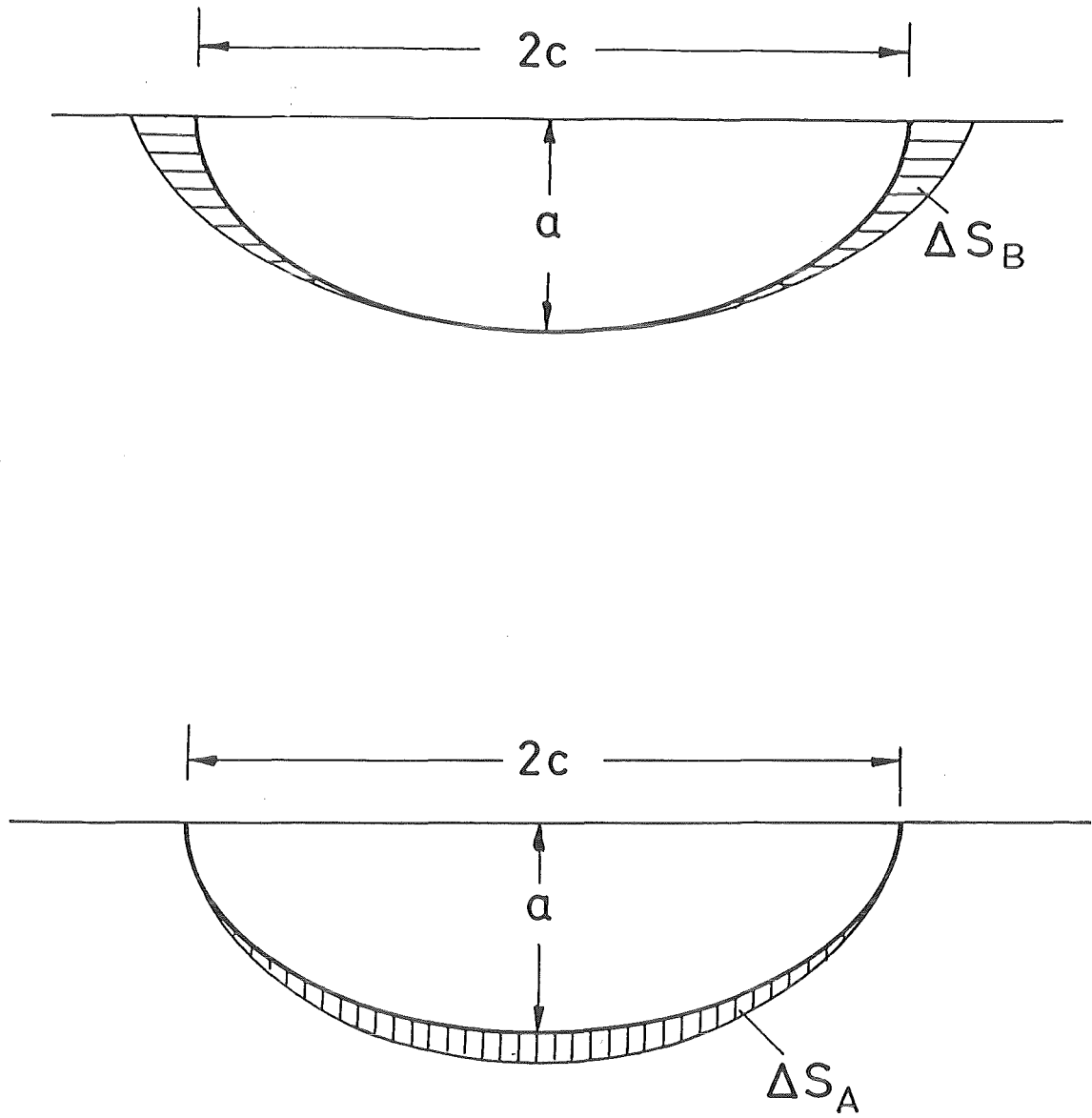


Fig.23 Crack increments during crack extension

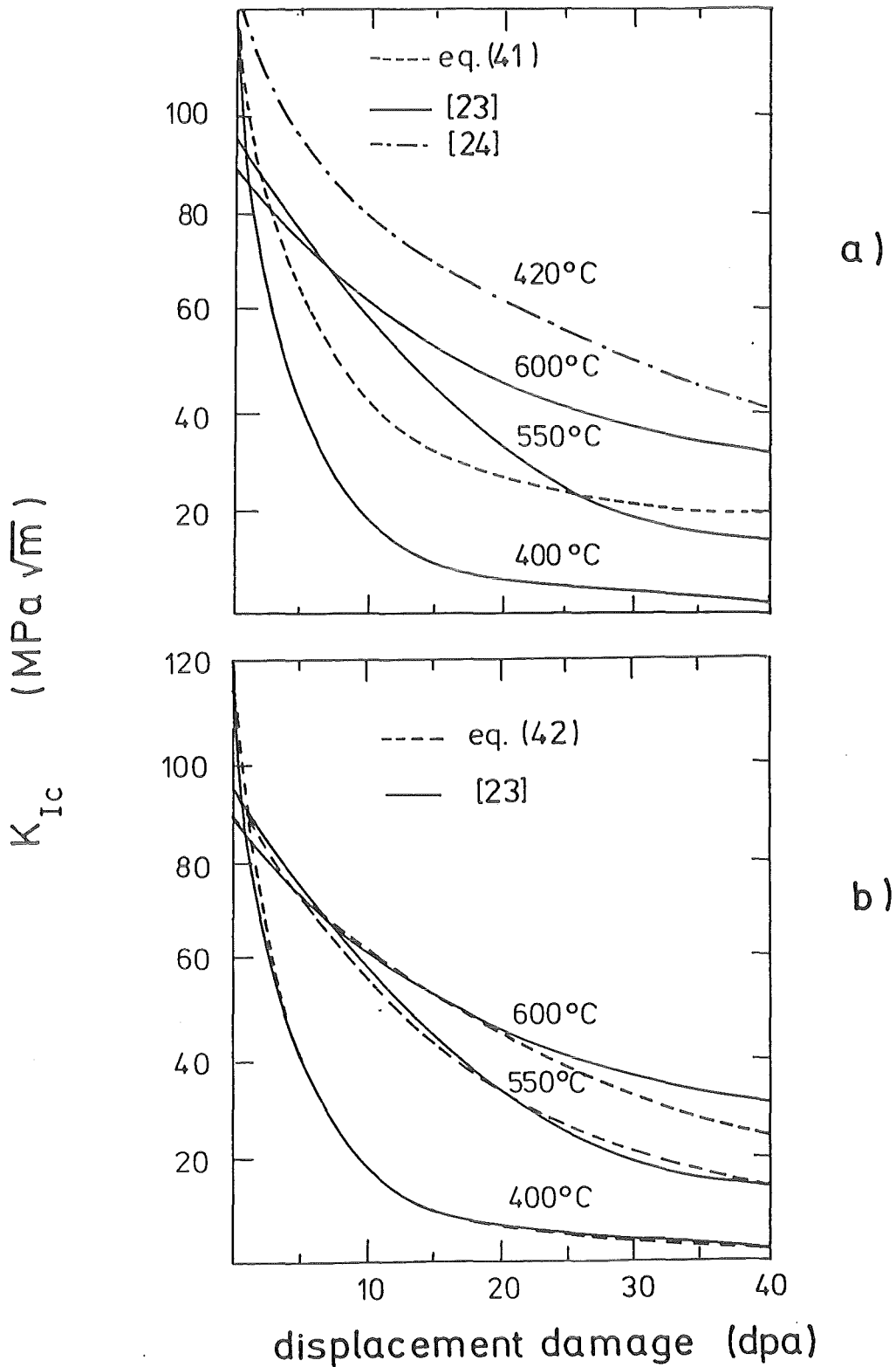


Fig.24 Irradiation embrittlement for SS316CW concluded from tensile test data

a) dependencies proposed by ODETTE and FREY [23] and WOLFER and JONES [24]

b) comparison with eq.(42)

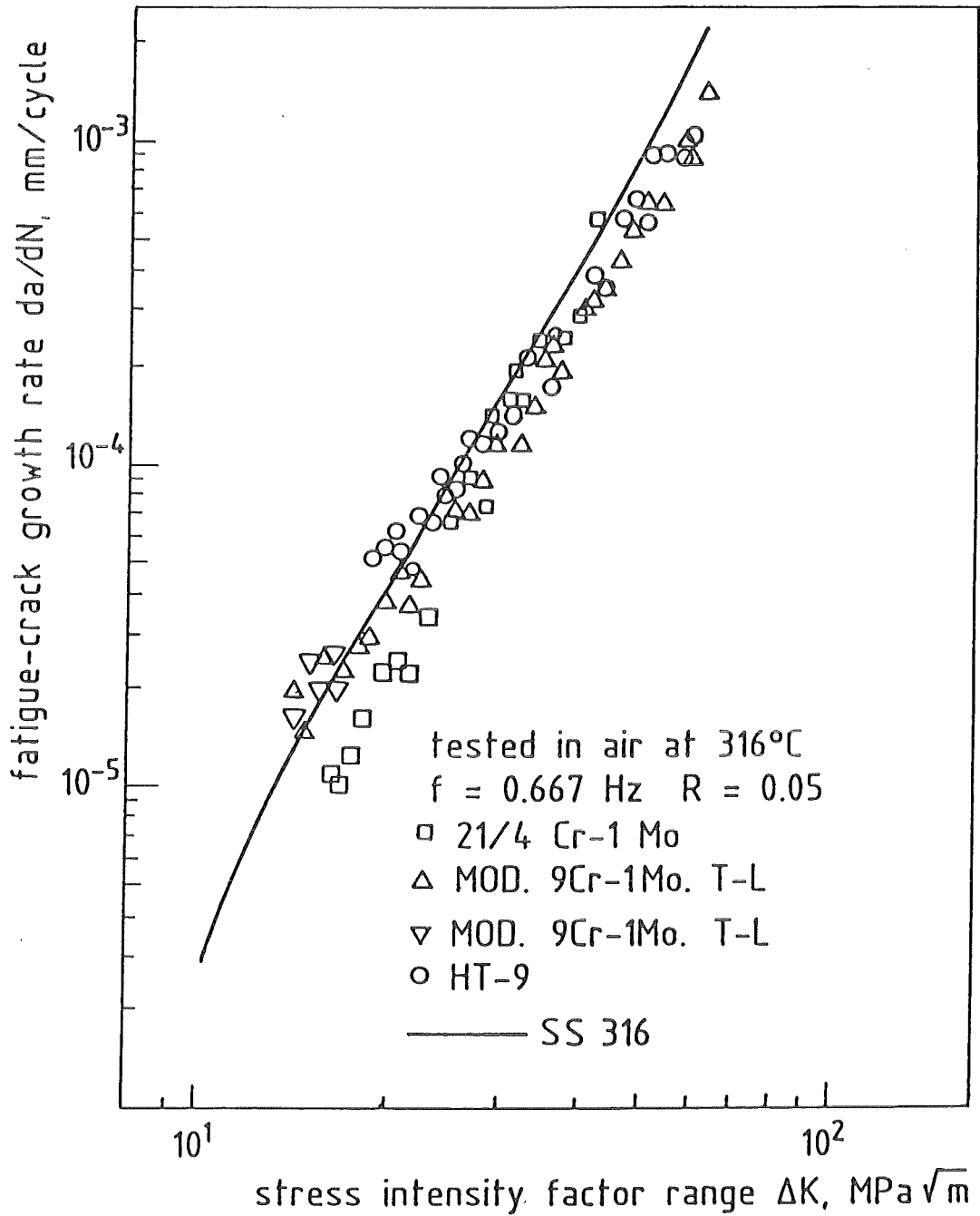


Fig.25 Fatigue crack growth results for martensitic steels [25] compared with the results for SS316 [11]

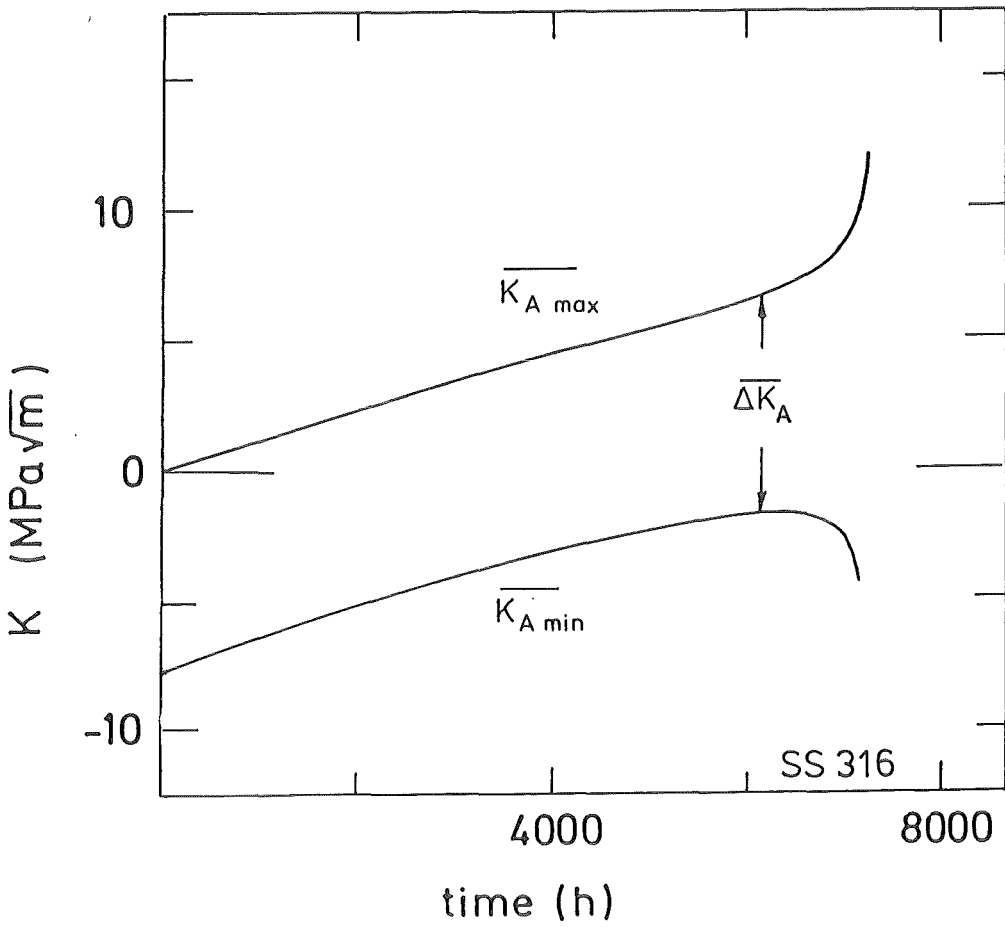
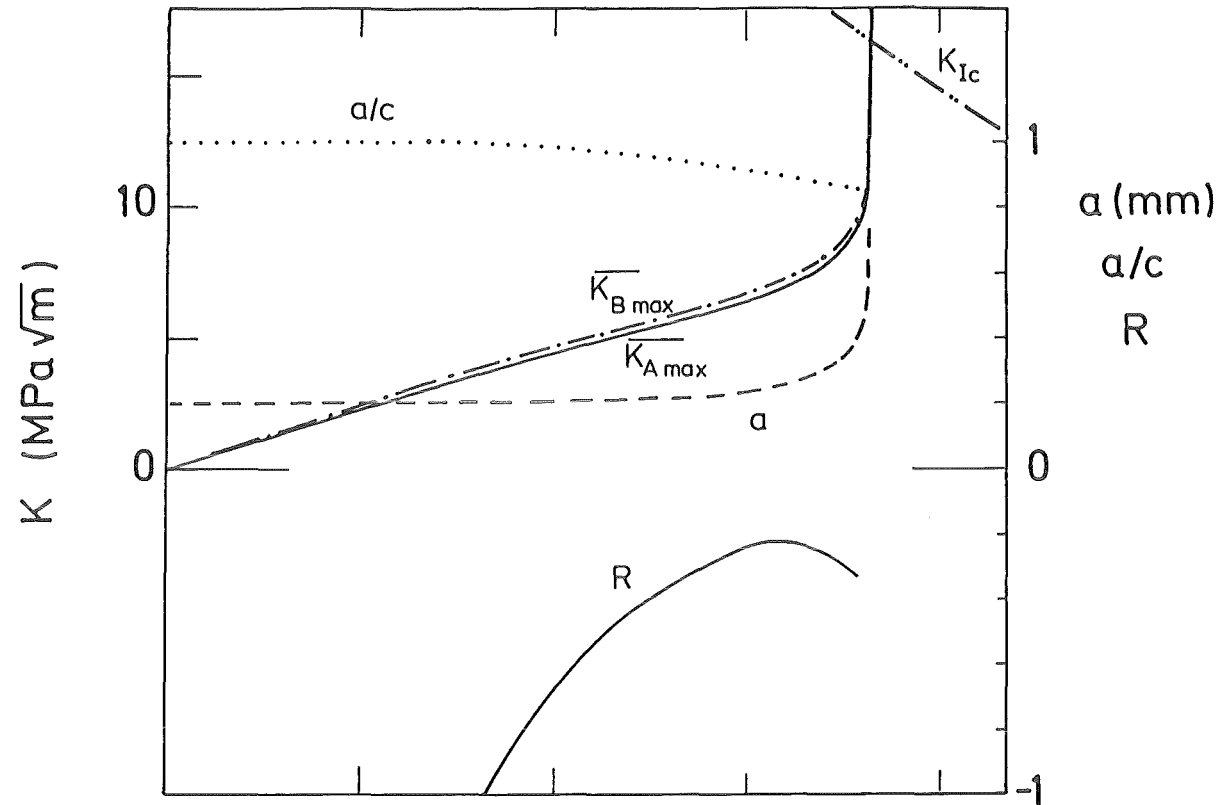


Fig.26 Development of a semi-circular surface crack situated at the plasma faced surface

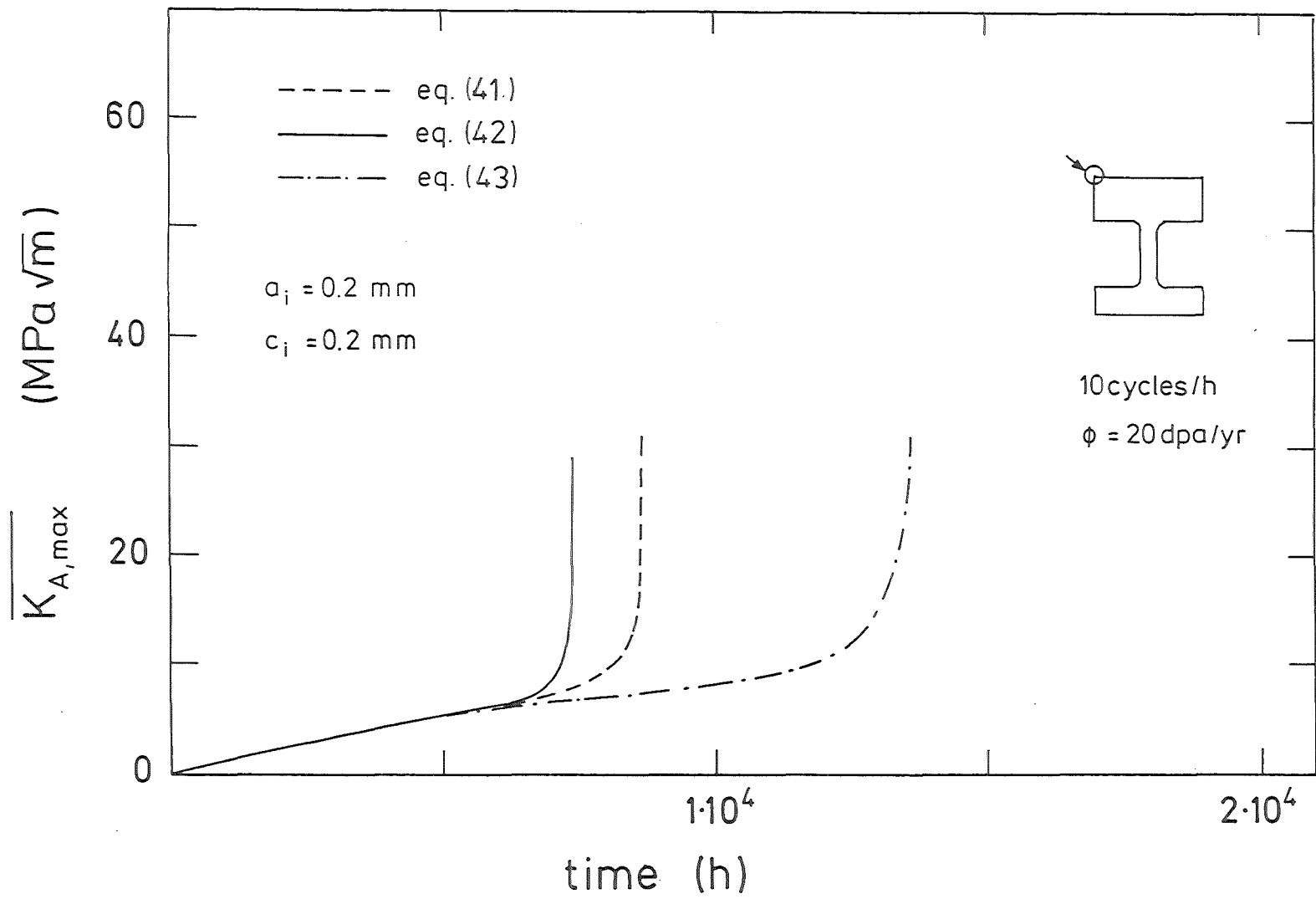


Fig.27 Influence of the embrittlement formulation on the maximum averaged stress intensity factor $\overline{K_{A,max}}$ for SS316CW

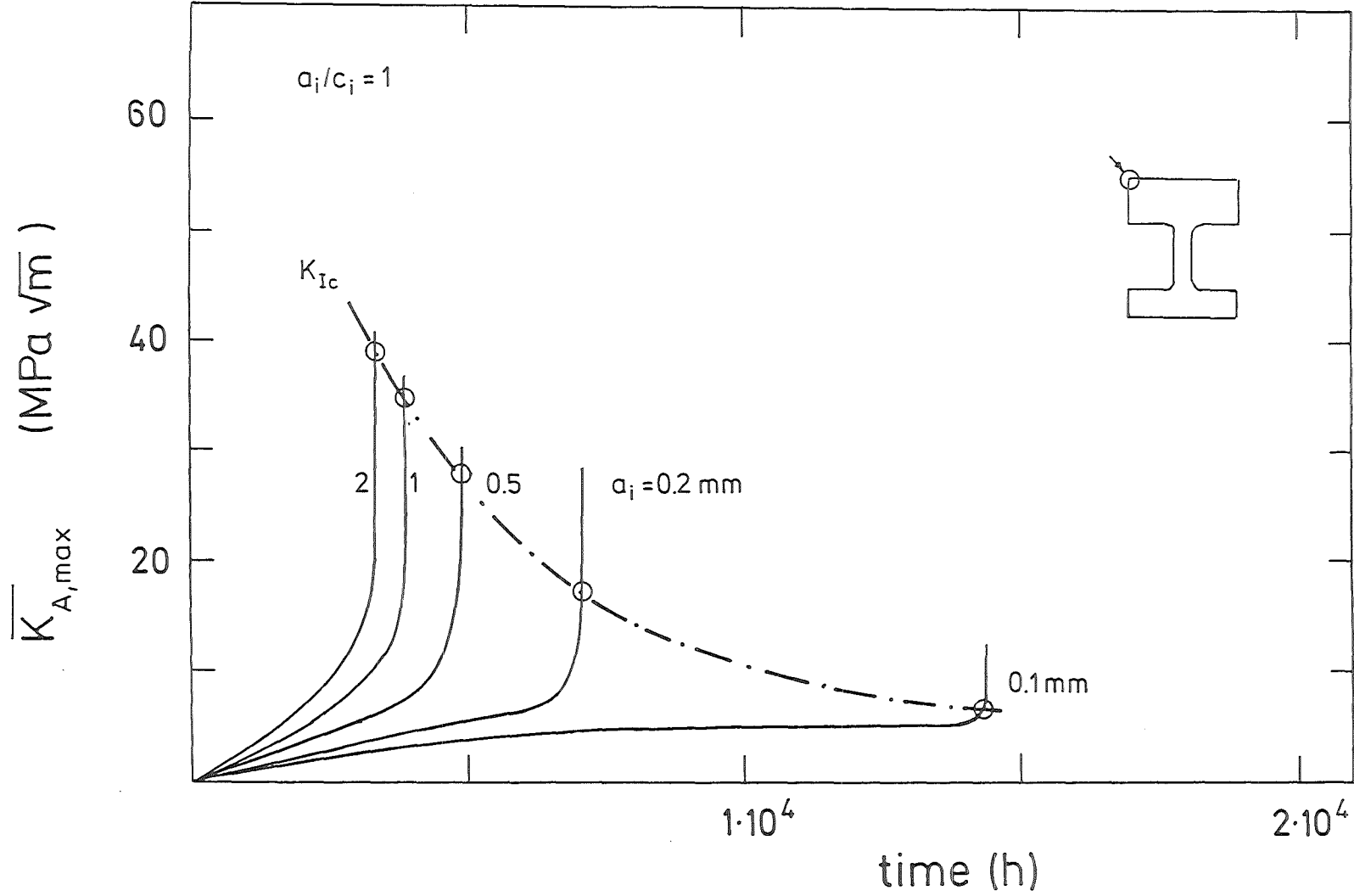


Fig.28 Influence of the crack depth on lifetime for SS316CW

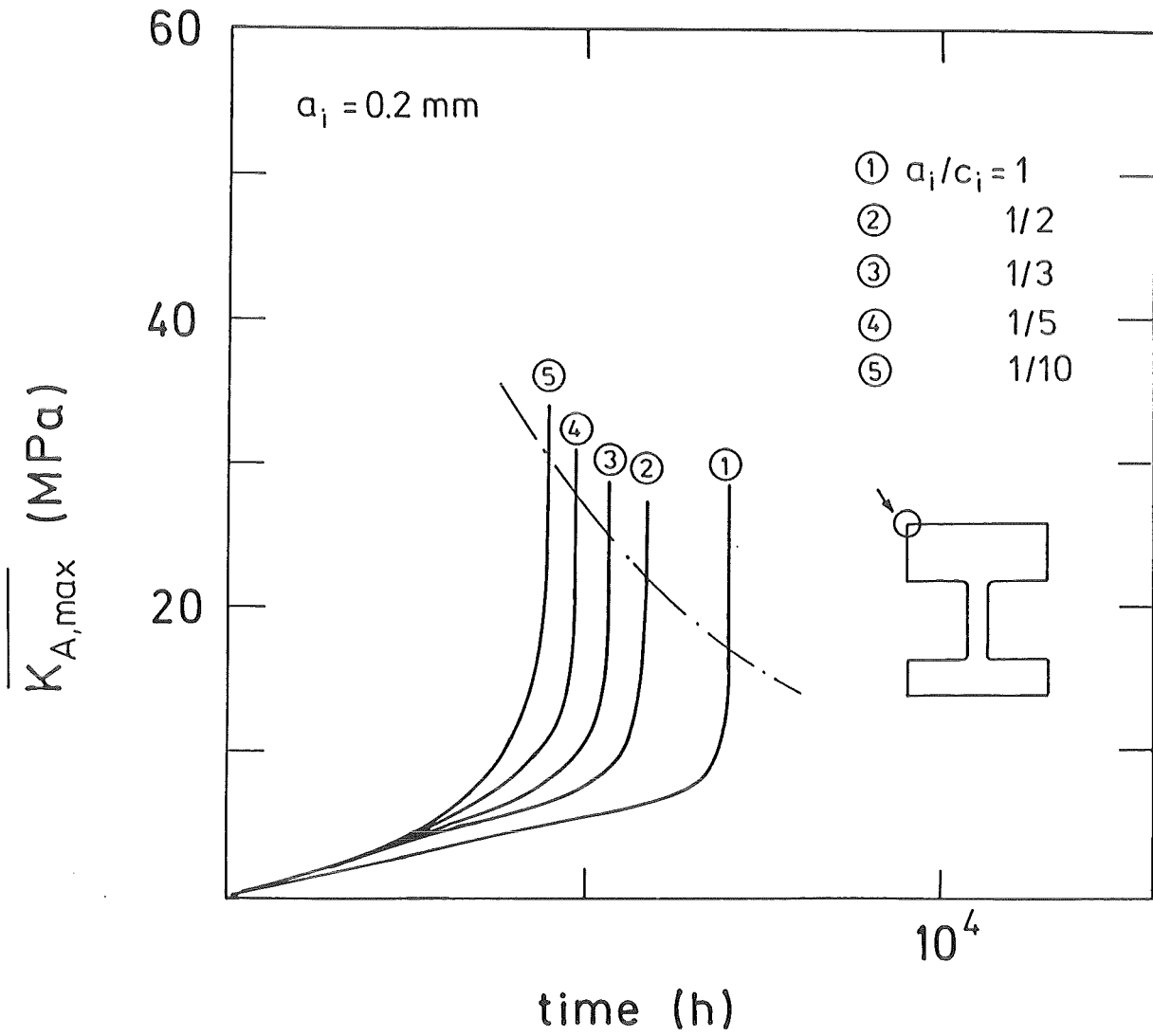


Fig.29 Influence of the initial aspect ratio a_i/c_i on life time for SS316CW

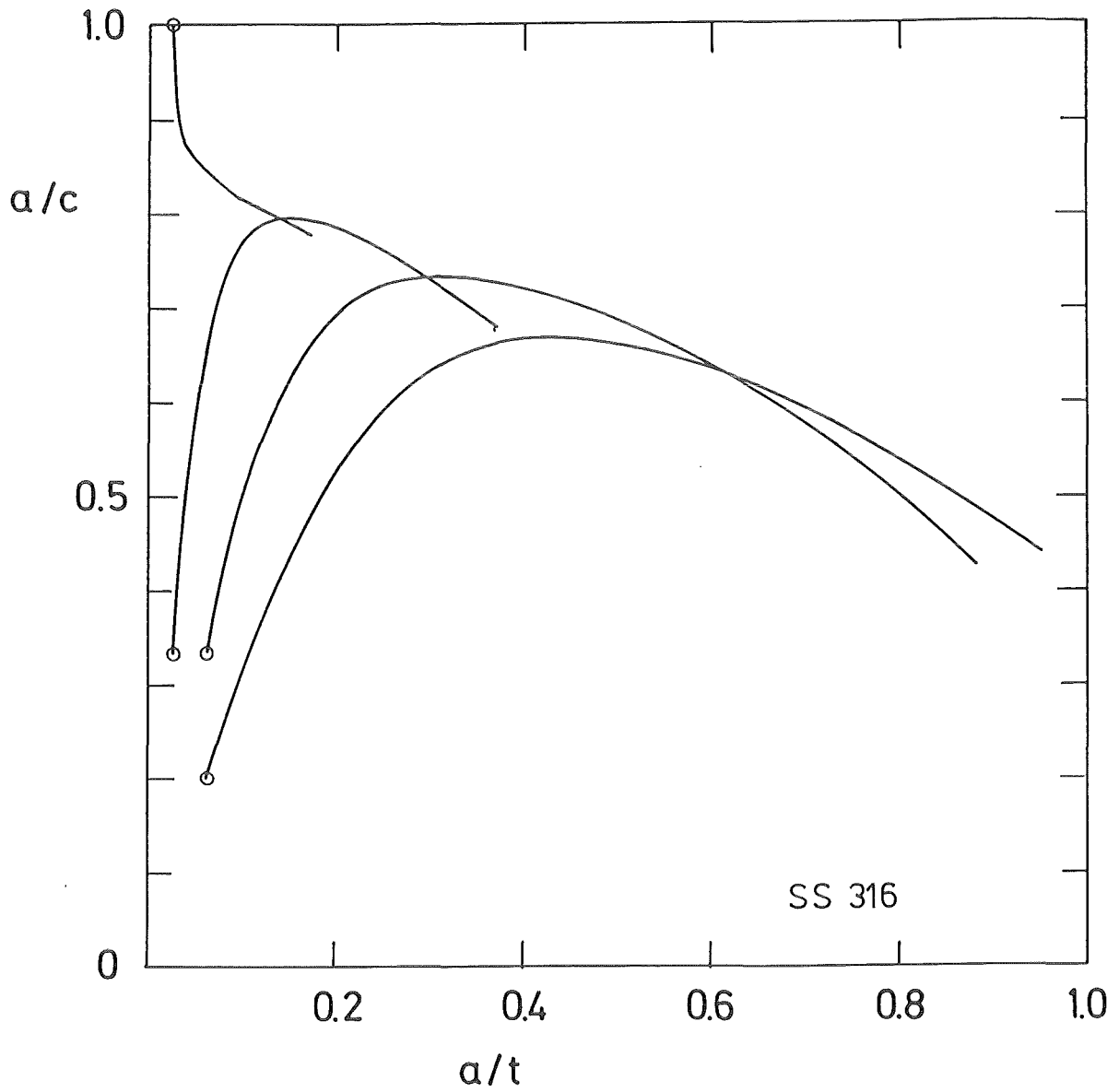


Fig.30 Change of ellipticity during crack extension

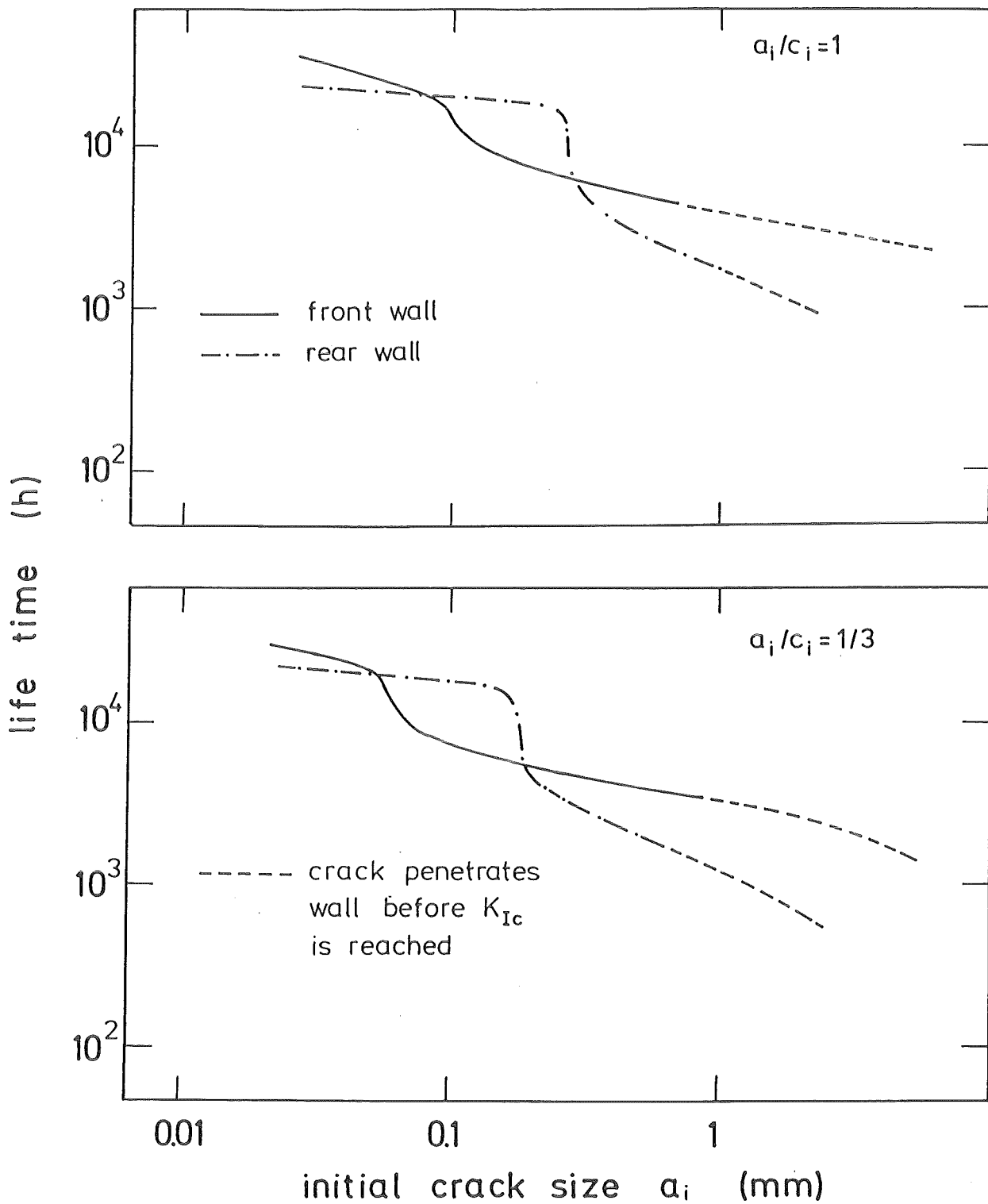


Fig.31 Lifetime in dependence of the initial crack size a_i for cracks situated in the front and rear part of the first wall for SS316CW

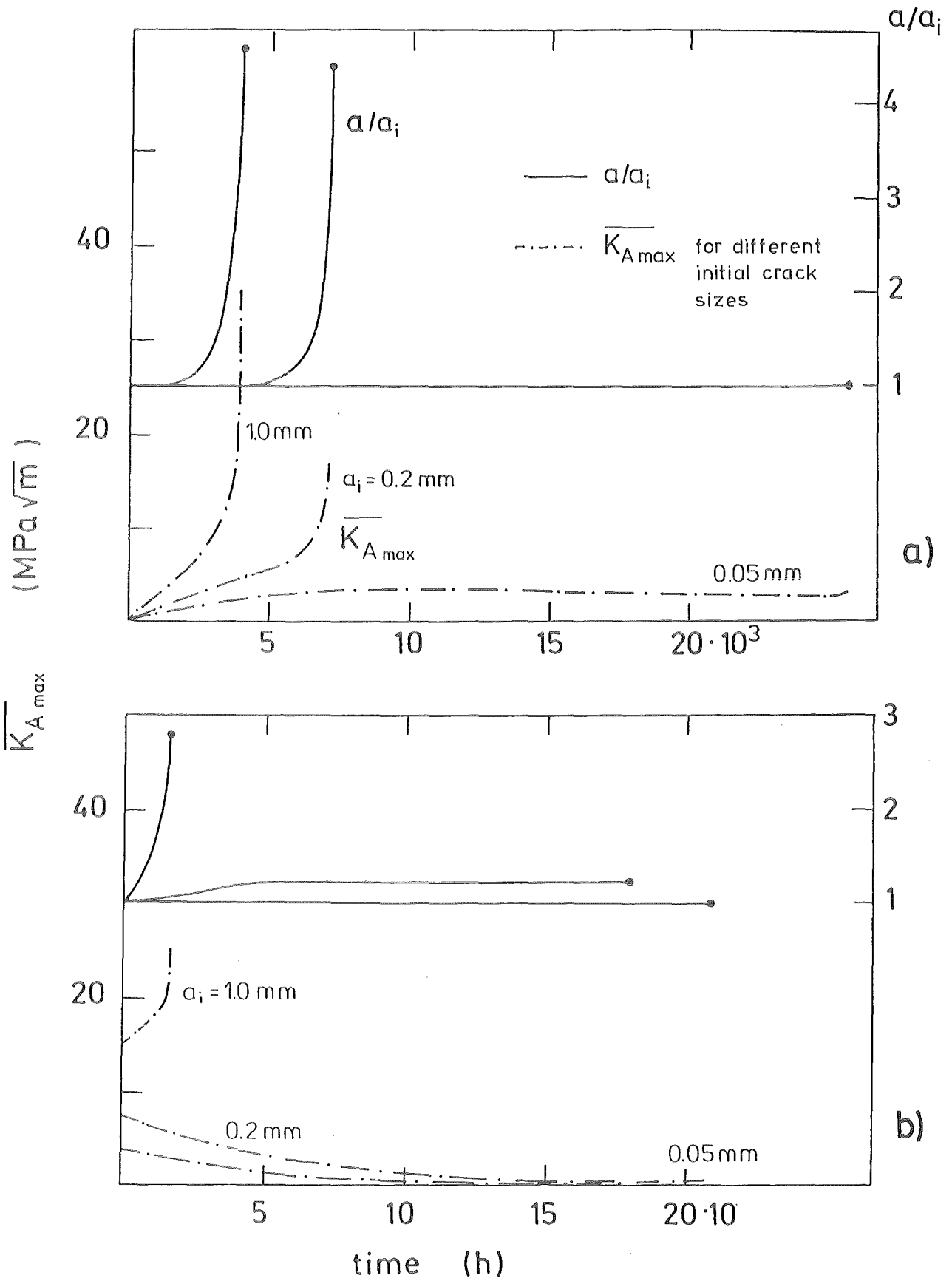


Fig.32 Maximum K-values and normalized crack sizes for cracks in the front part (a) and cracks in the backward part (b) of the wall (SS316CW)

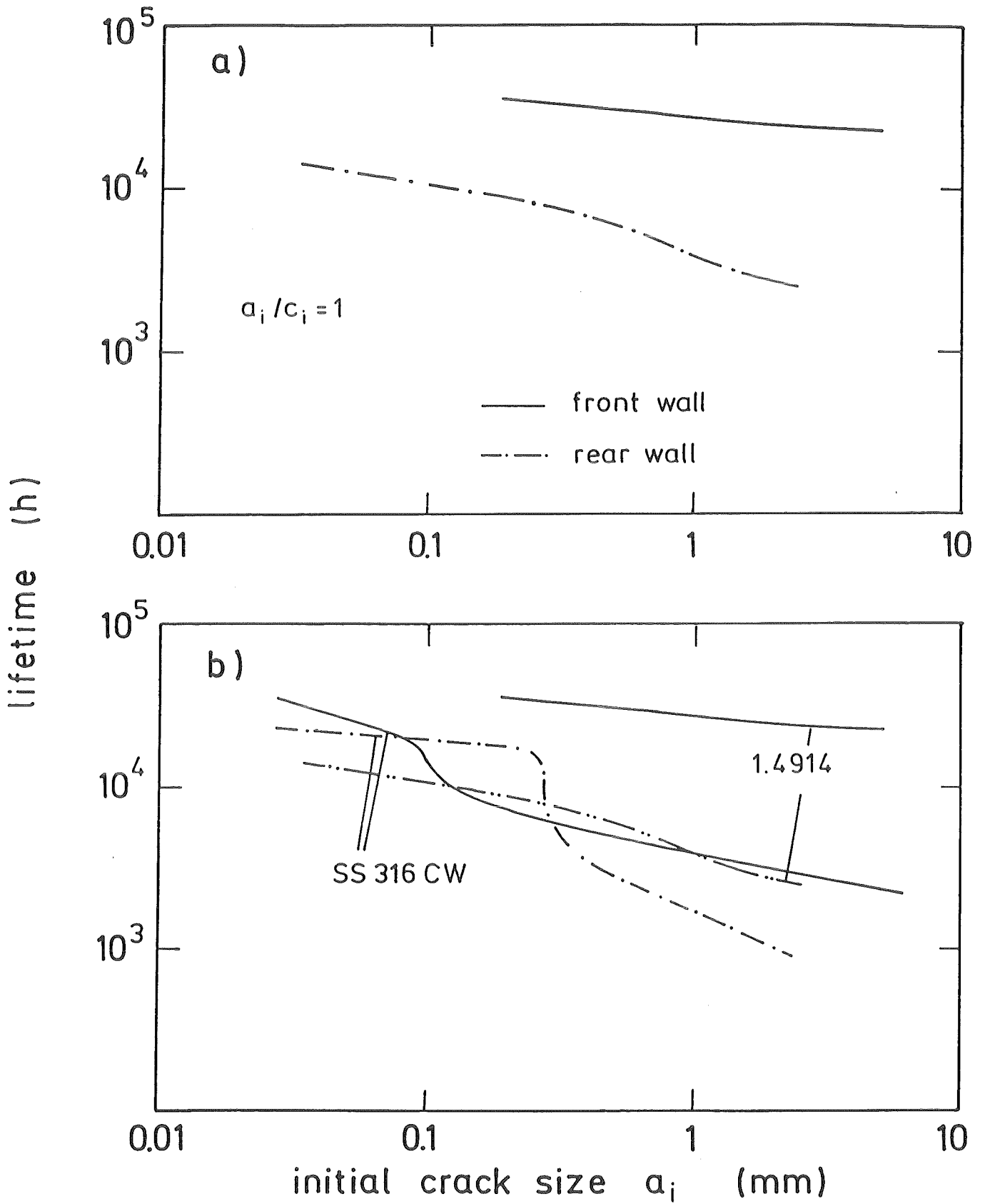


Fig.33 a) Lifetime diagramm for 1.4914

b) Comparison of lifetime data SS316CW/1.4914

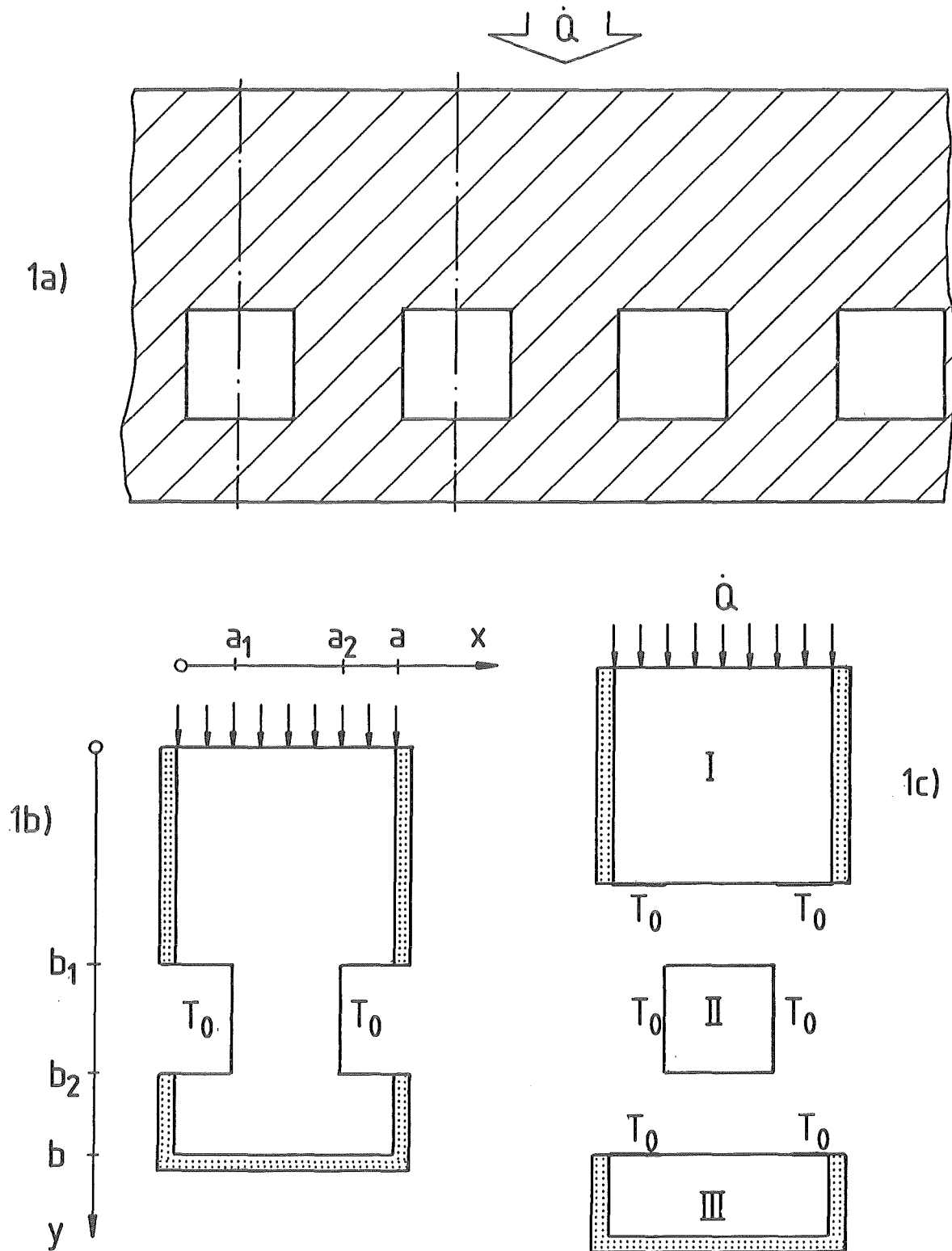


Fig. A1 First wall element with inner cooling channels affected by surface heat flux

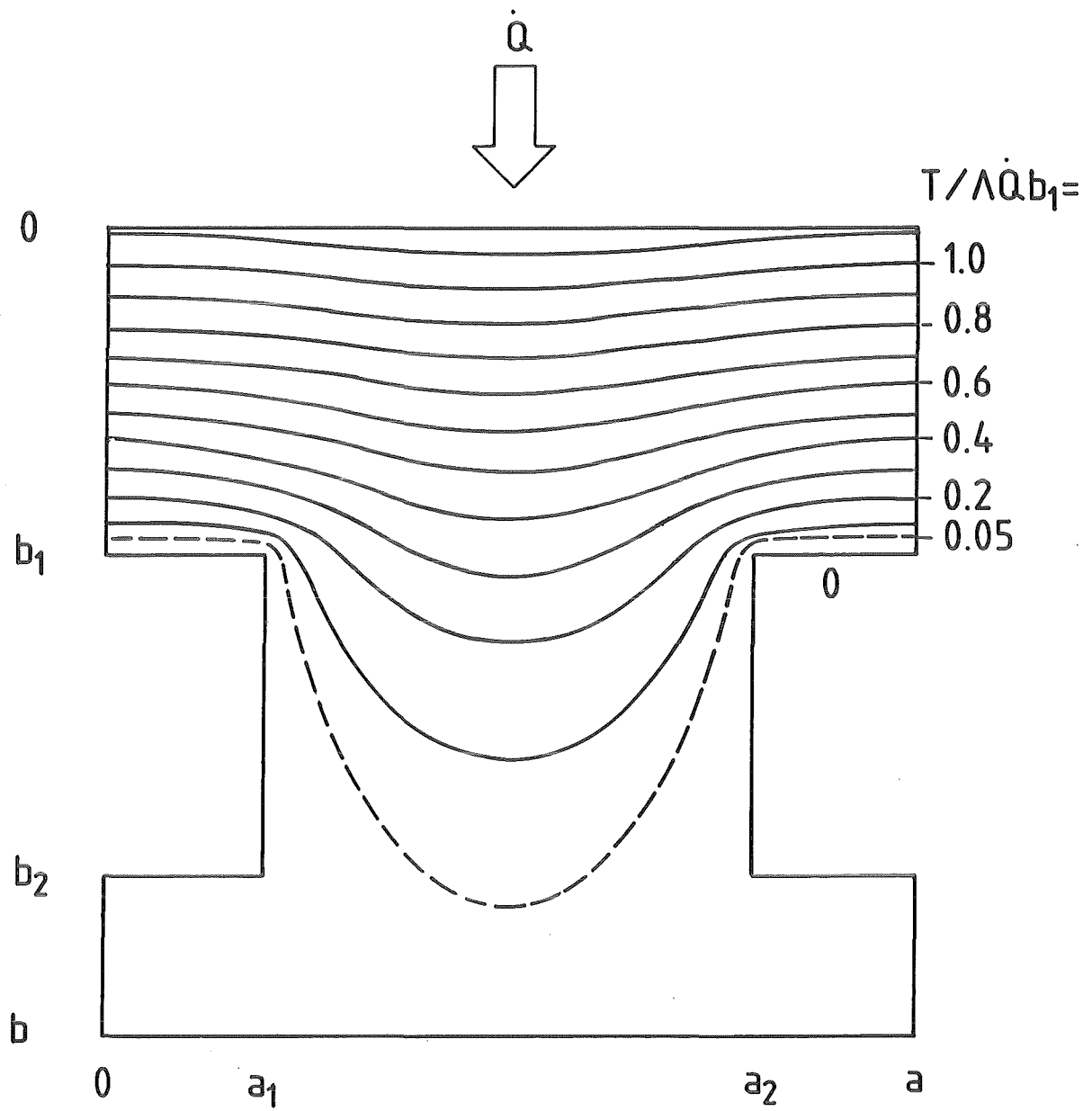


Fig. A2 Normalized stationary temperature distribution in a first wall with inner cooling channels for surface heating

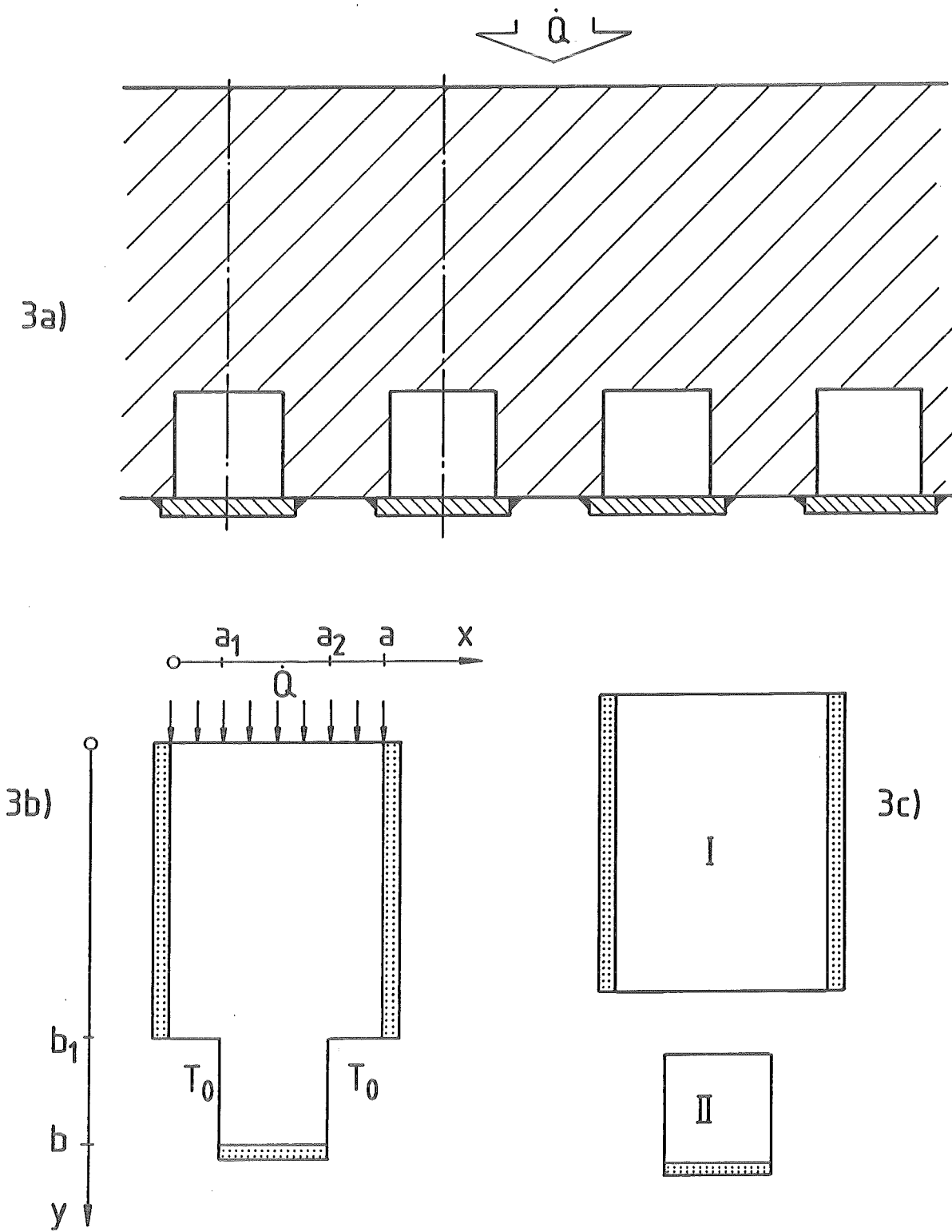


Fig. A3 First wall element with slot shaped cooling channels affected by surface heat flux

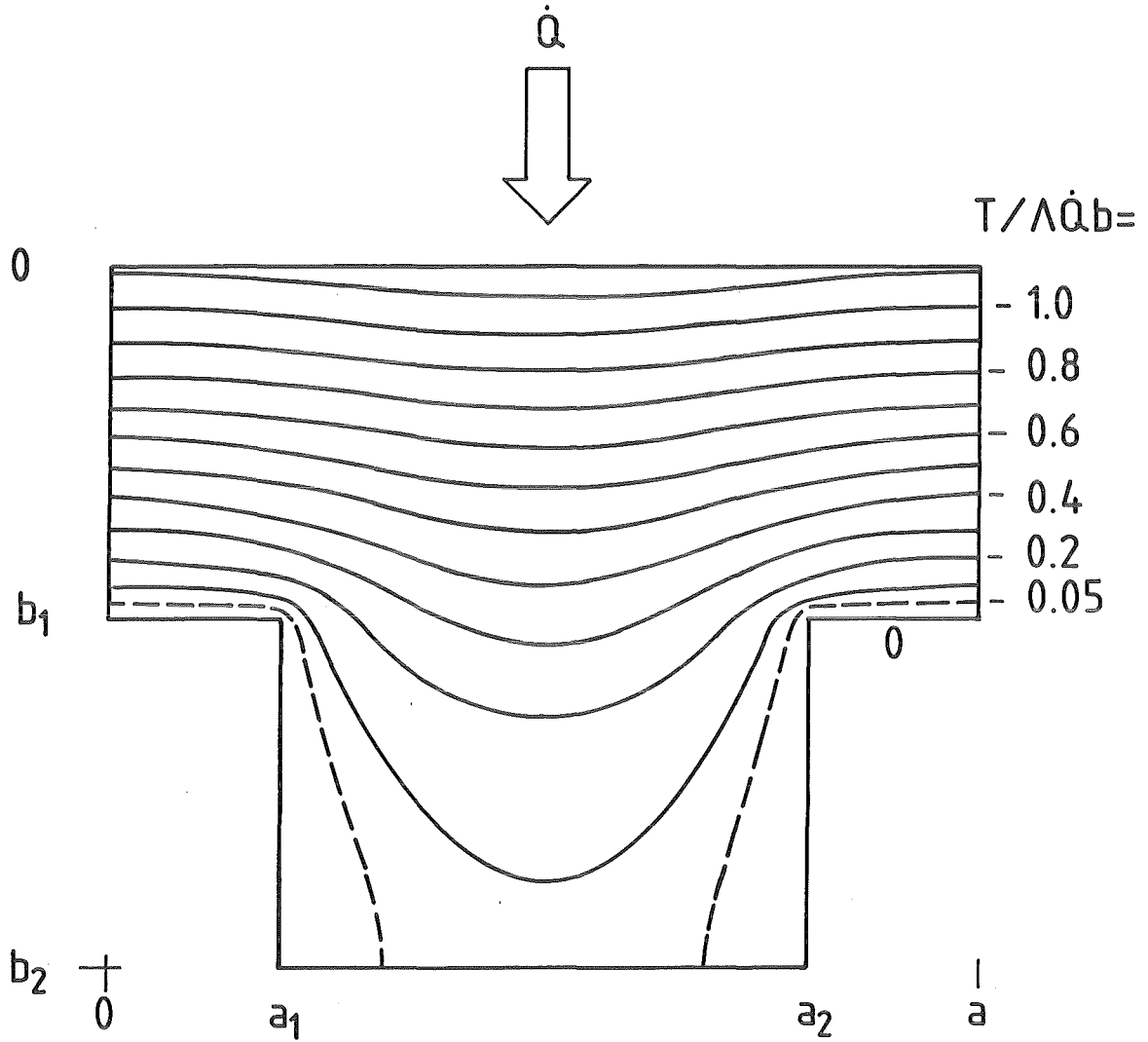


Fig. A4 Normalized stationary temperature distribution in a first wall with slot shaped cooling channels for surface heating

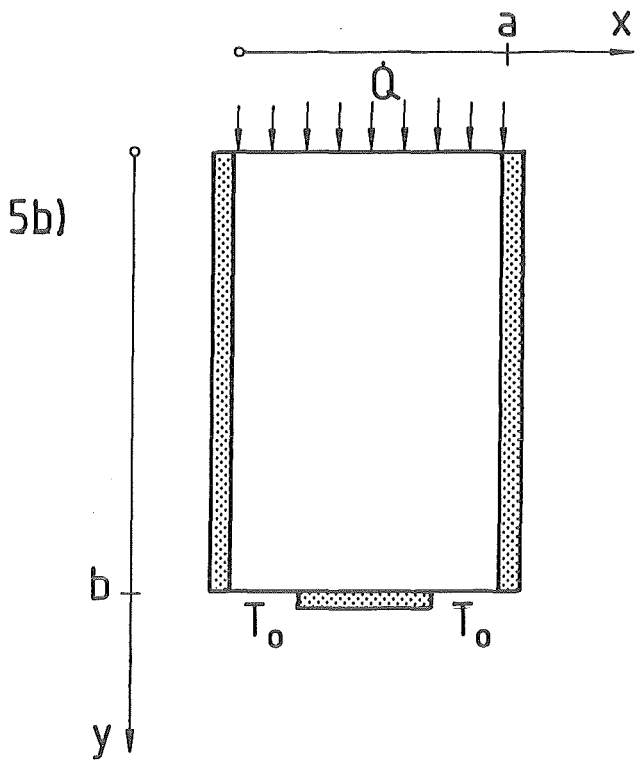
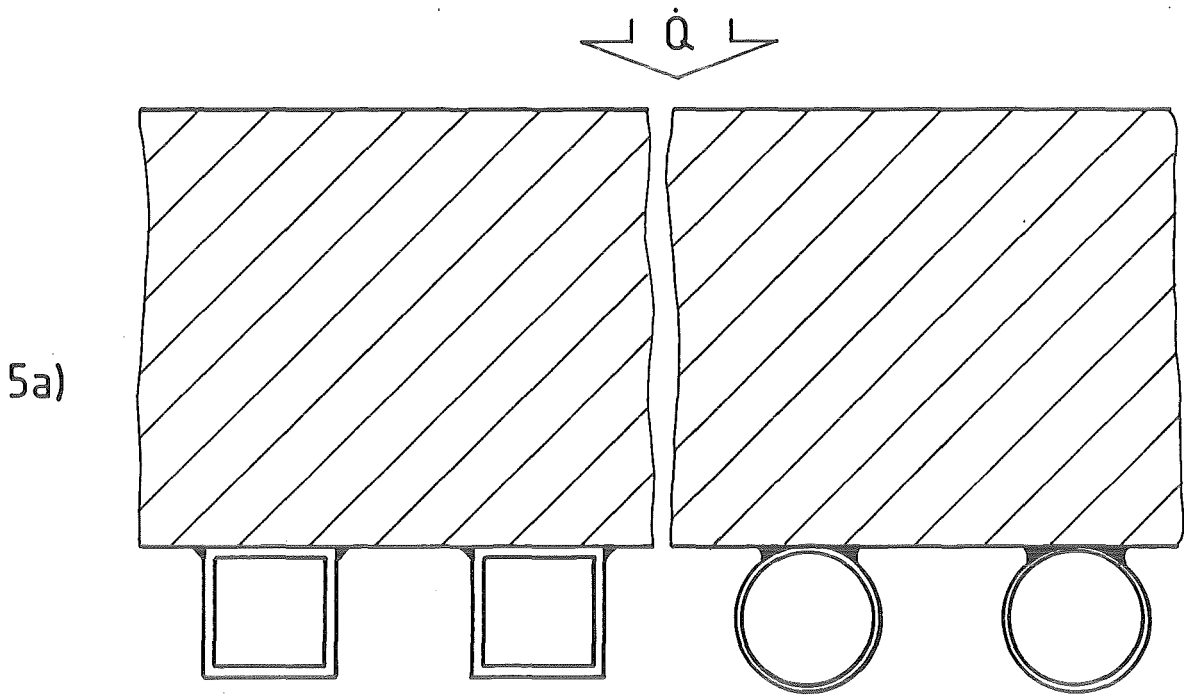


Fig. A5 First wall element with rear connected cooling channels affected by surface heating

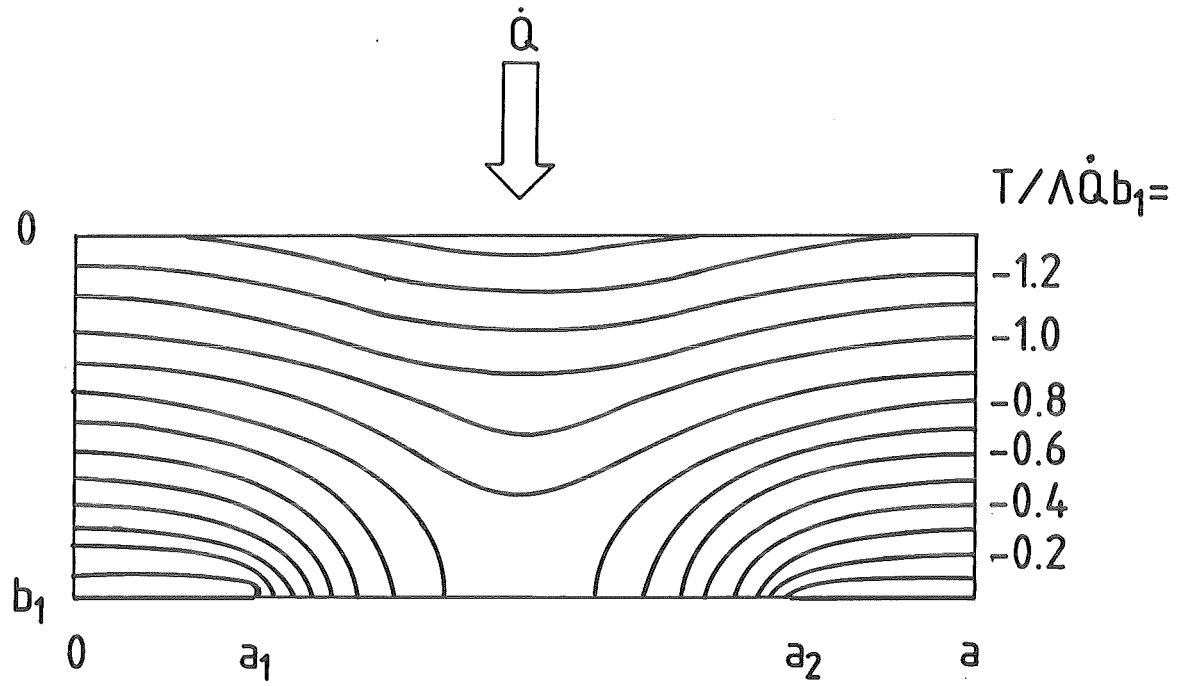


Fig. A6 Normalized stationary temperature distribution in a first wall with rear connected cooling channels for surface heating

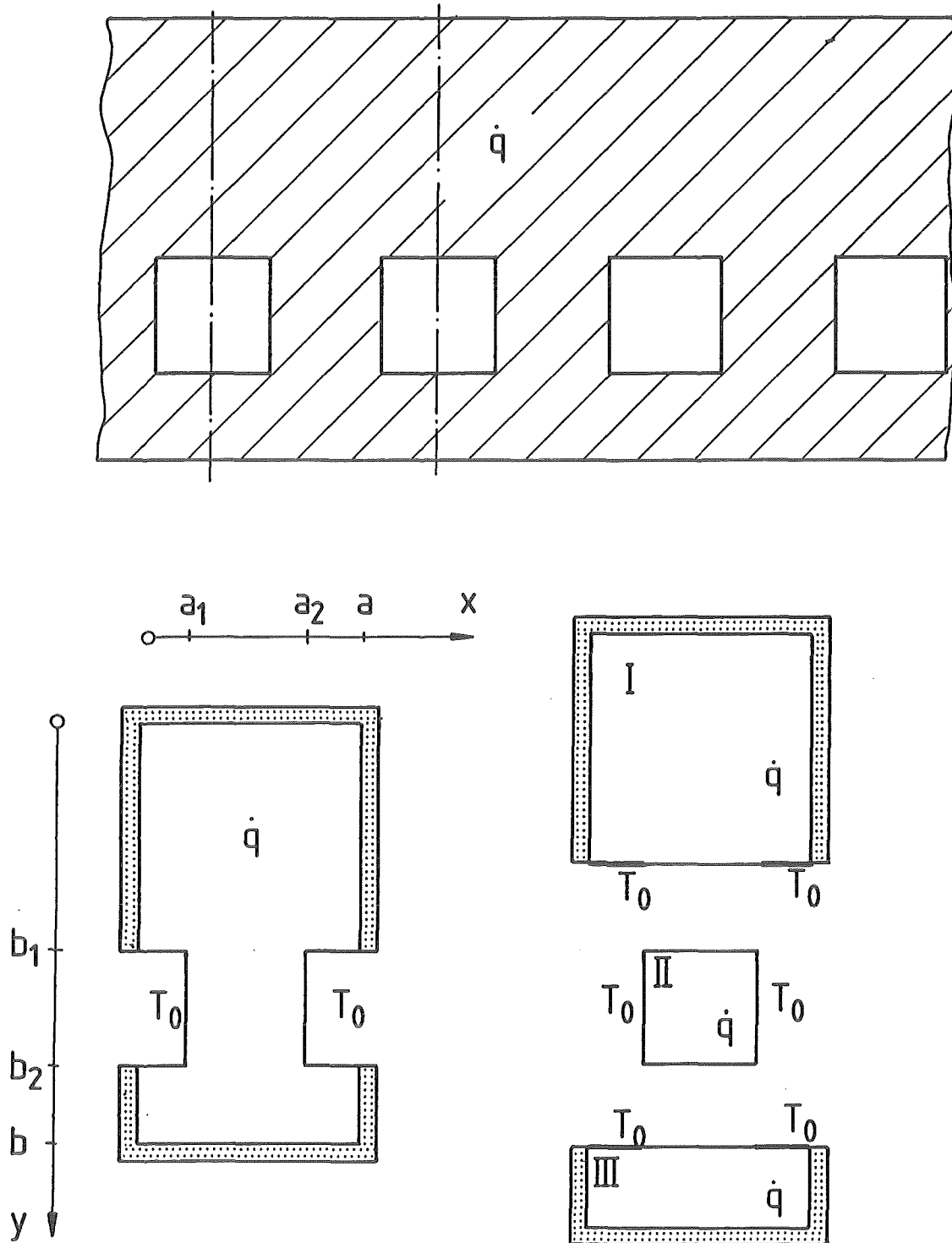


Fig. A7 First wall element with inner cooling channels affected by volumetric heating

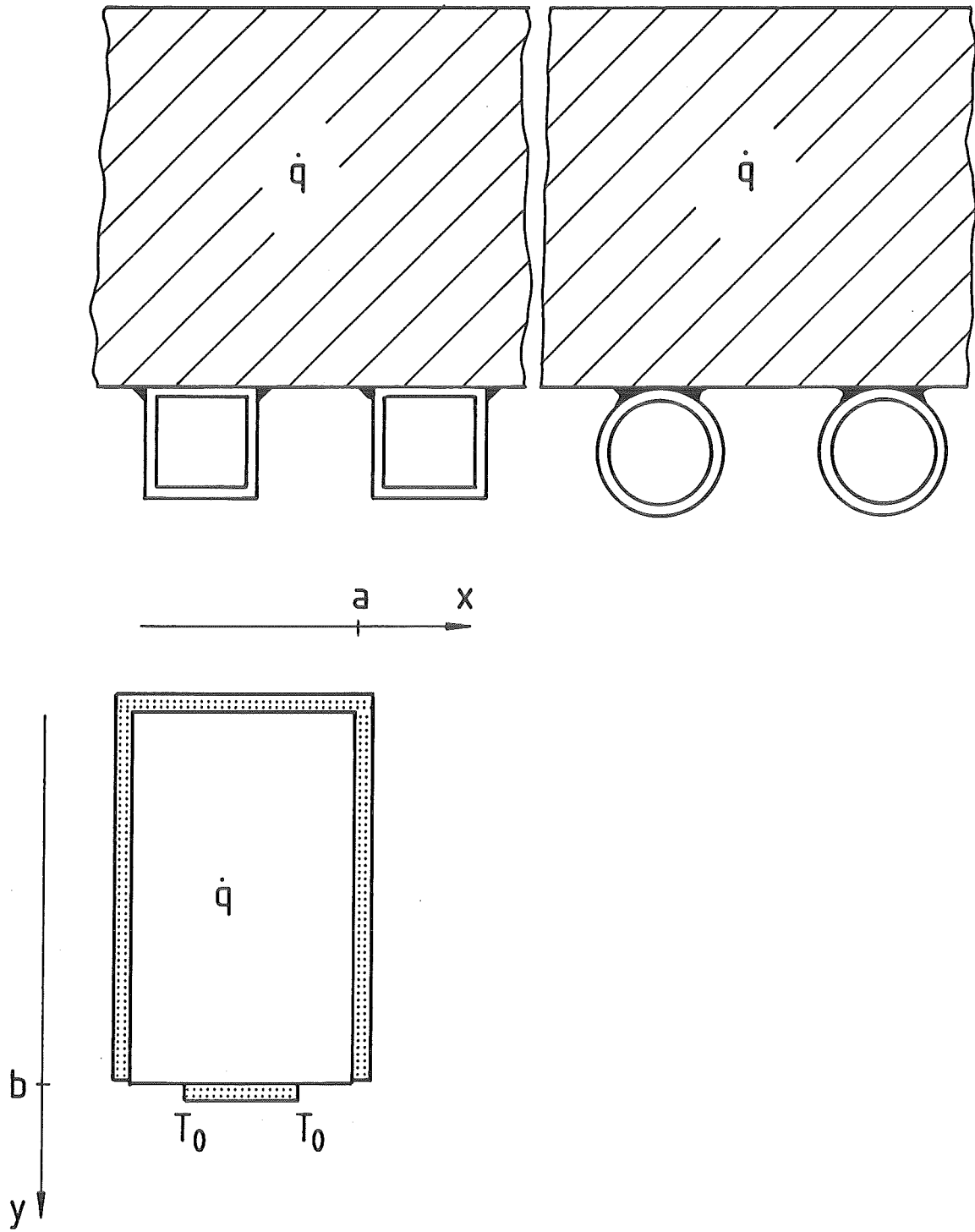


Fig. A8 First wall element with rear connected cooling channels affected by volumetric heating

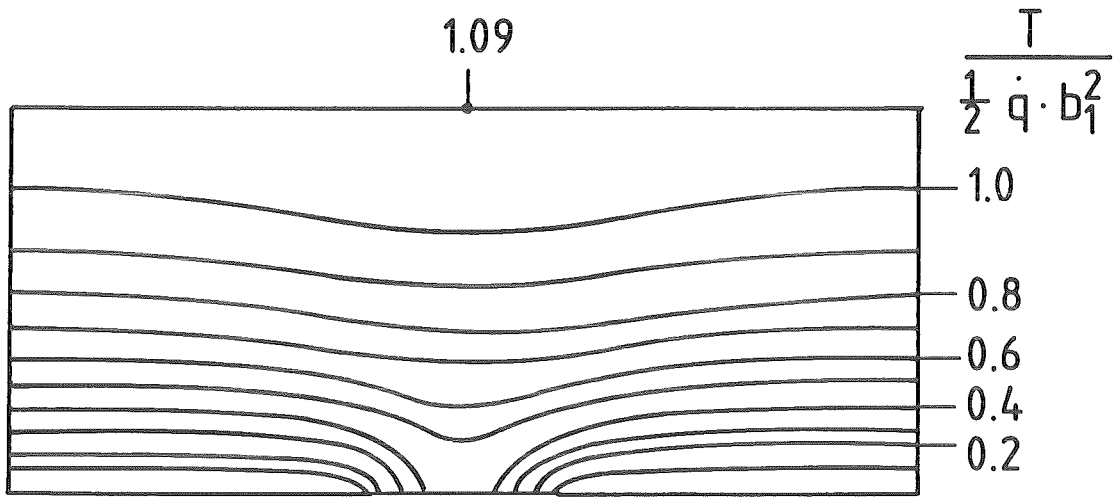


Fig. A9 Isotherms in a first wall with rear connected cooling channels for volumetric heating

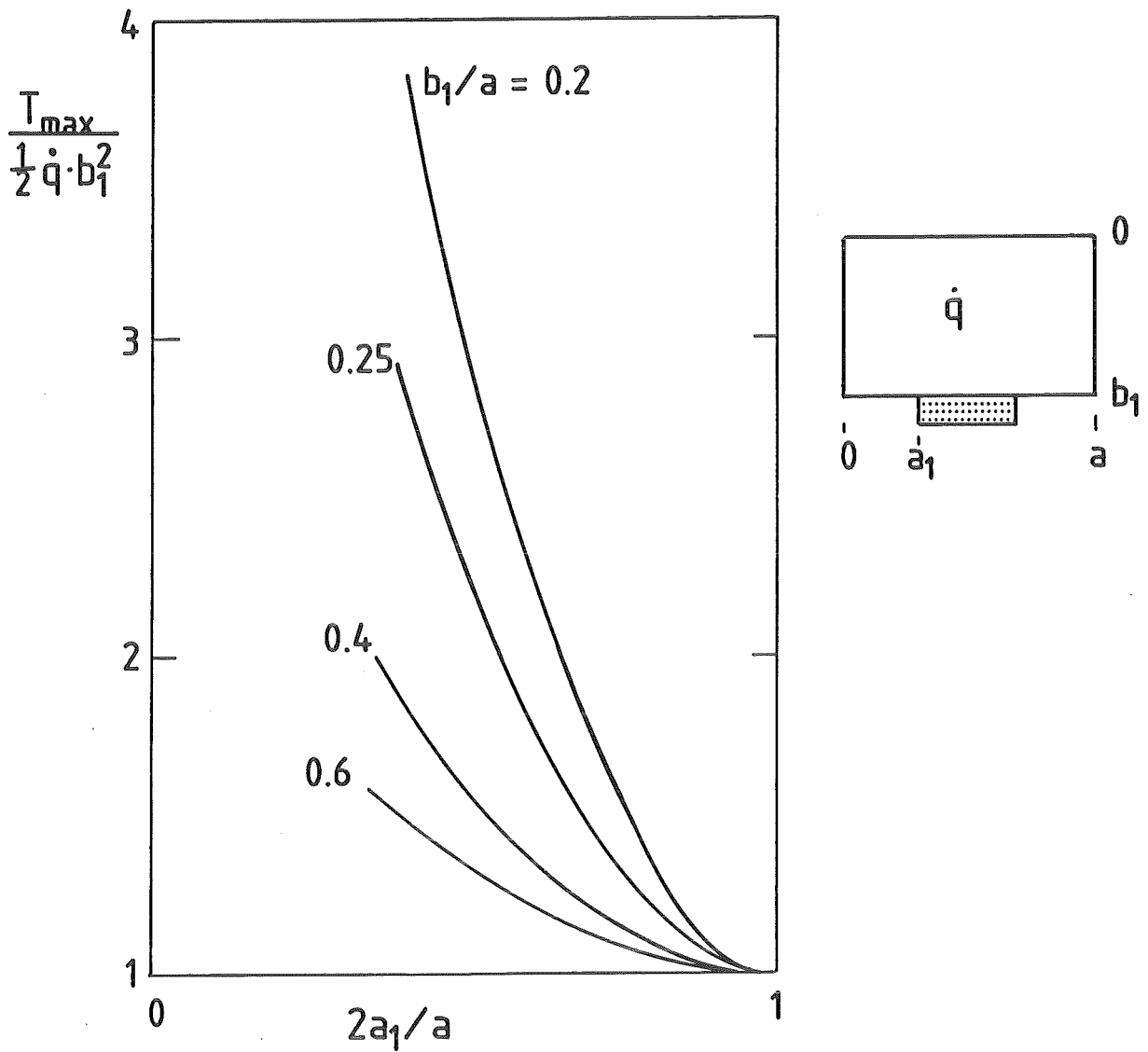


Fig. A10 Maximum temperature for the structure of fig. A8 for different geometrical portions (volumetric heating)

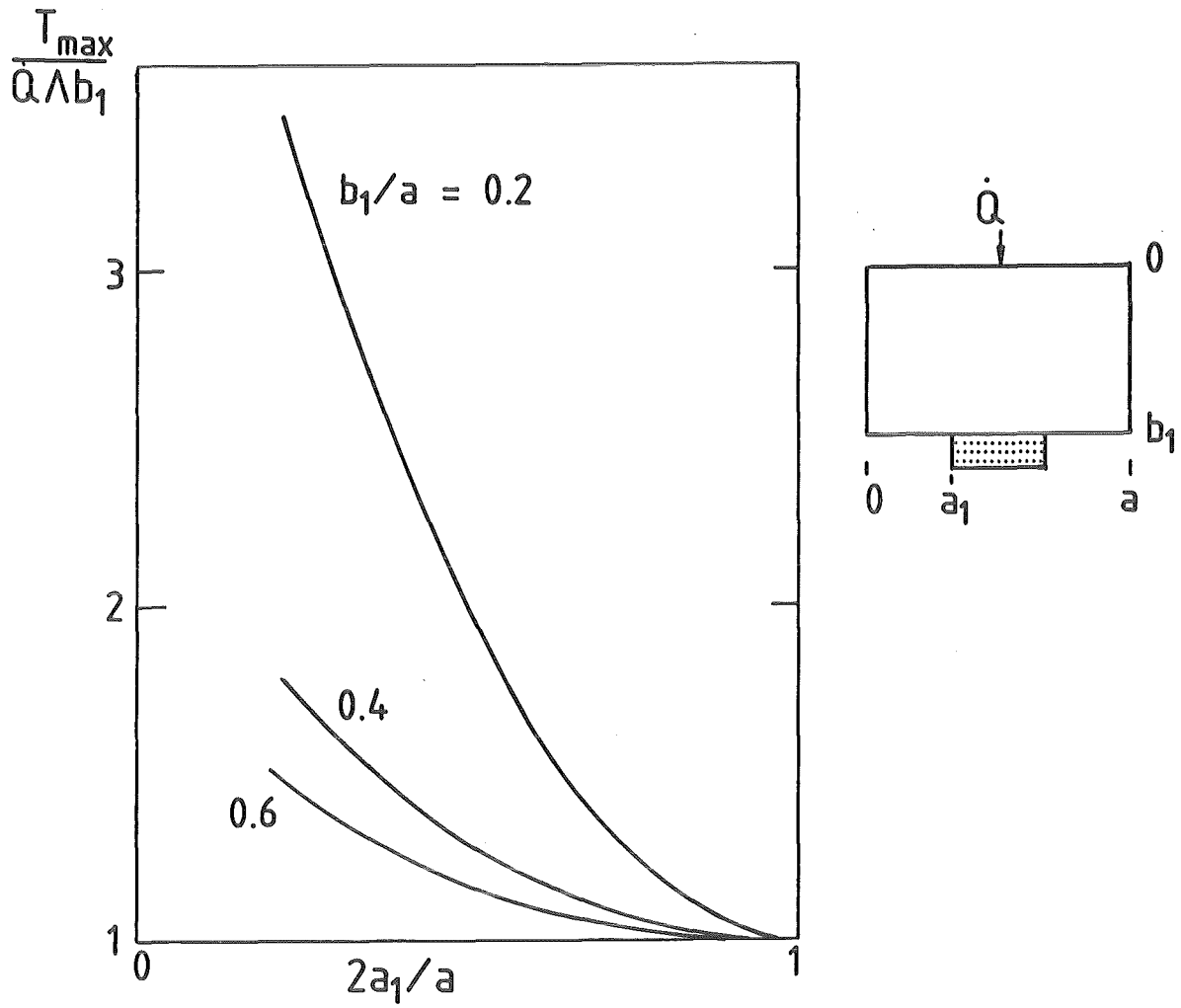


Fig. A11 Maximum temperature in a first wall element with rear connected cooling channels for several geometrical proportions (surface heating)

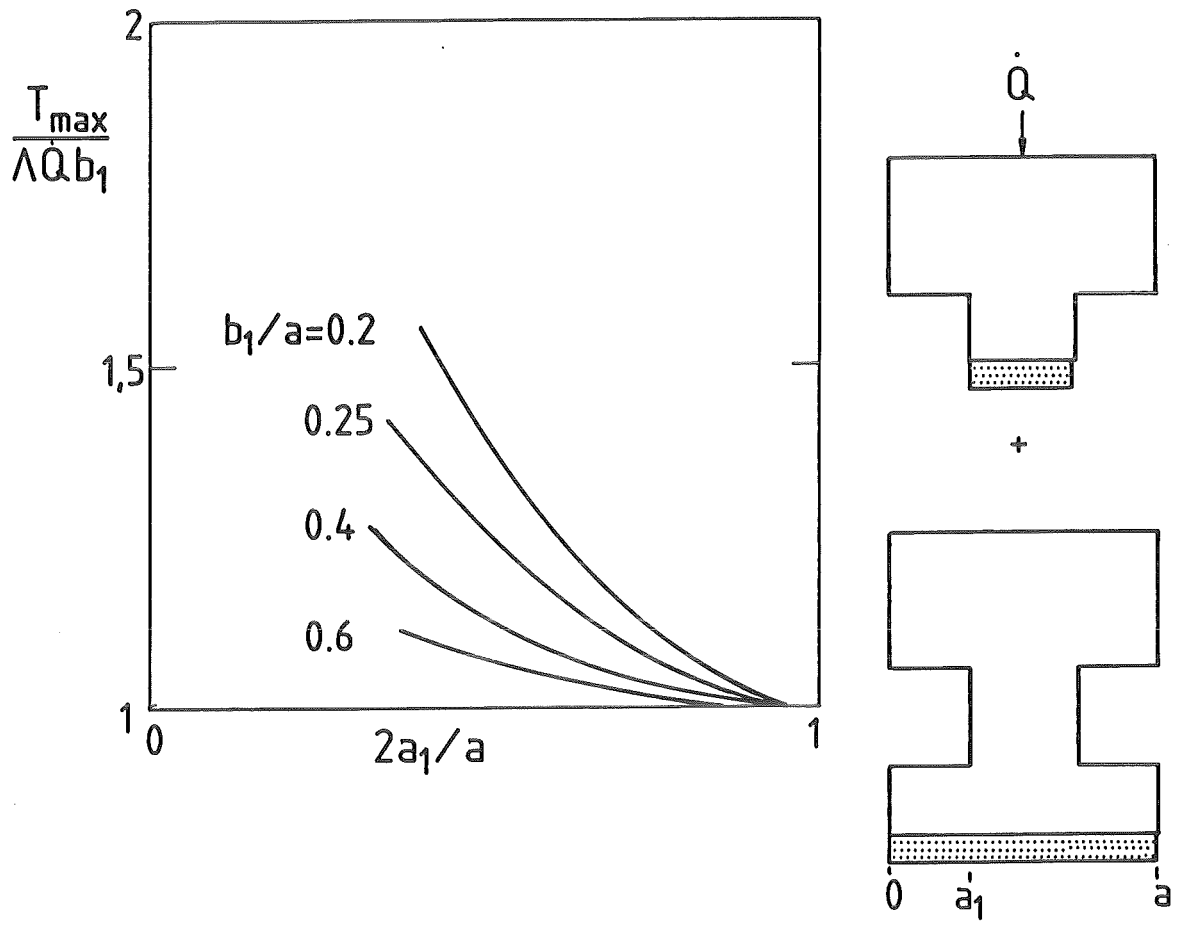


Fig. A12 Maximum temperature in a first wall with inner channels and slot shaped channels, respectively (surface heating)

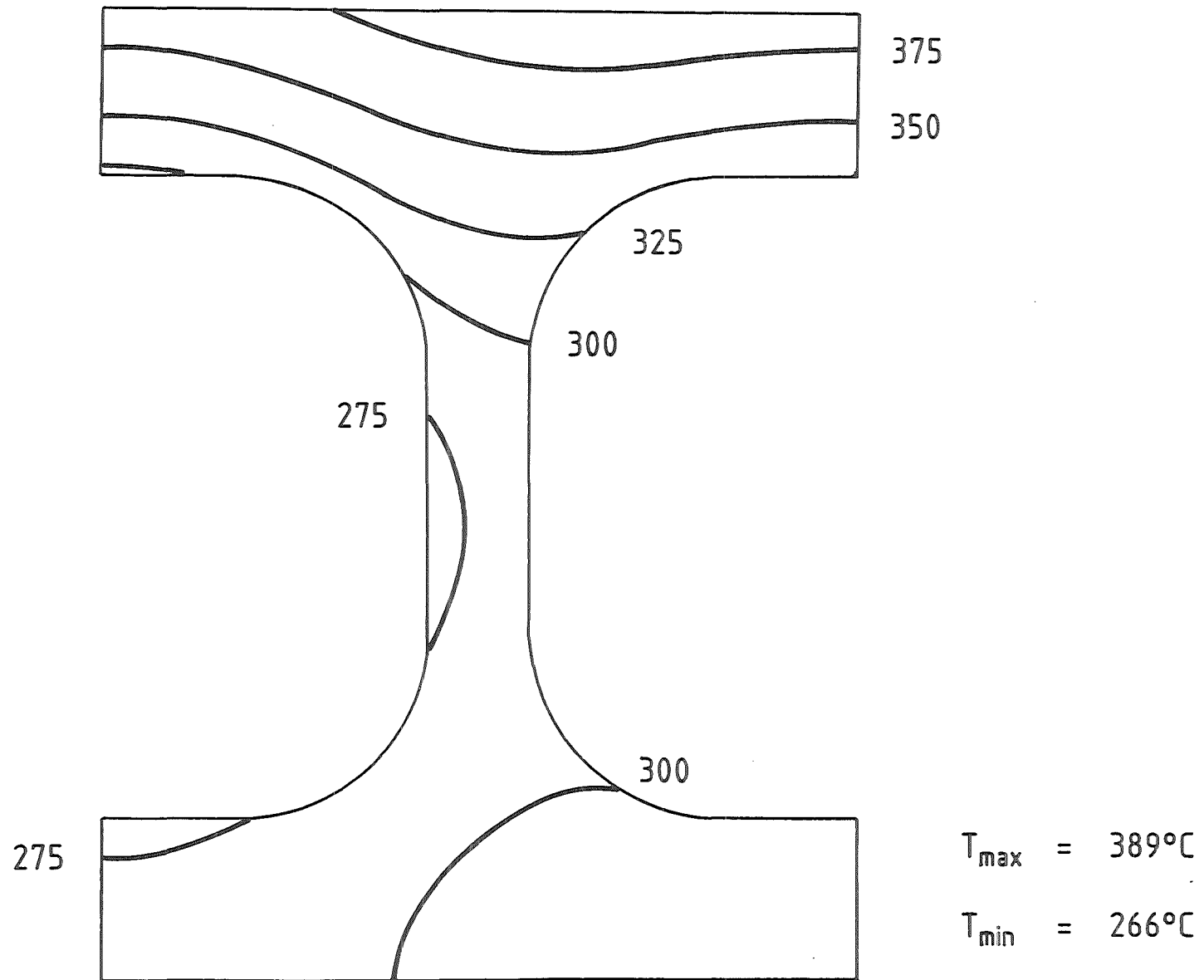


Fig. B1.2 Contour plot of temperature distribution for austenitic steel (case 2)

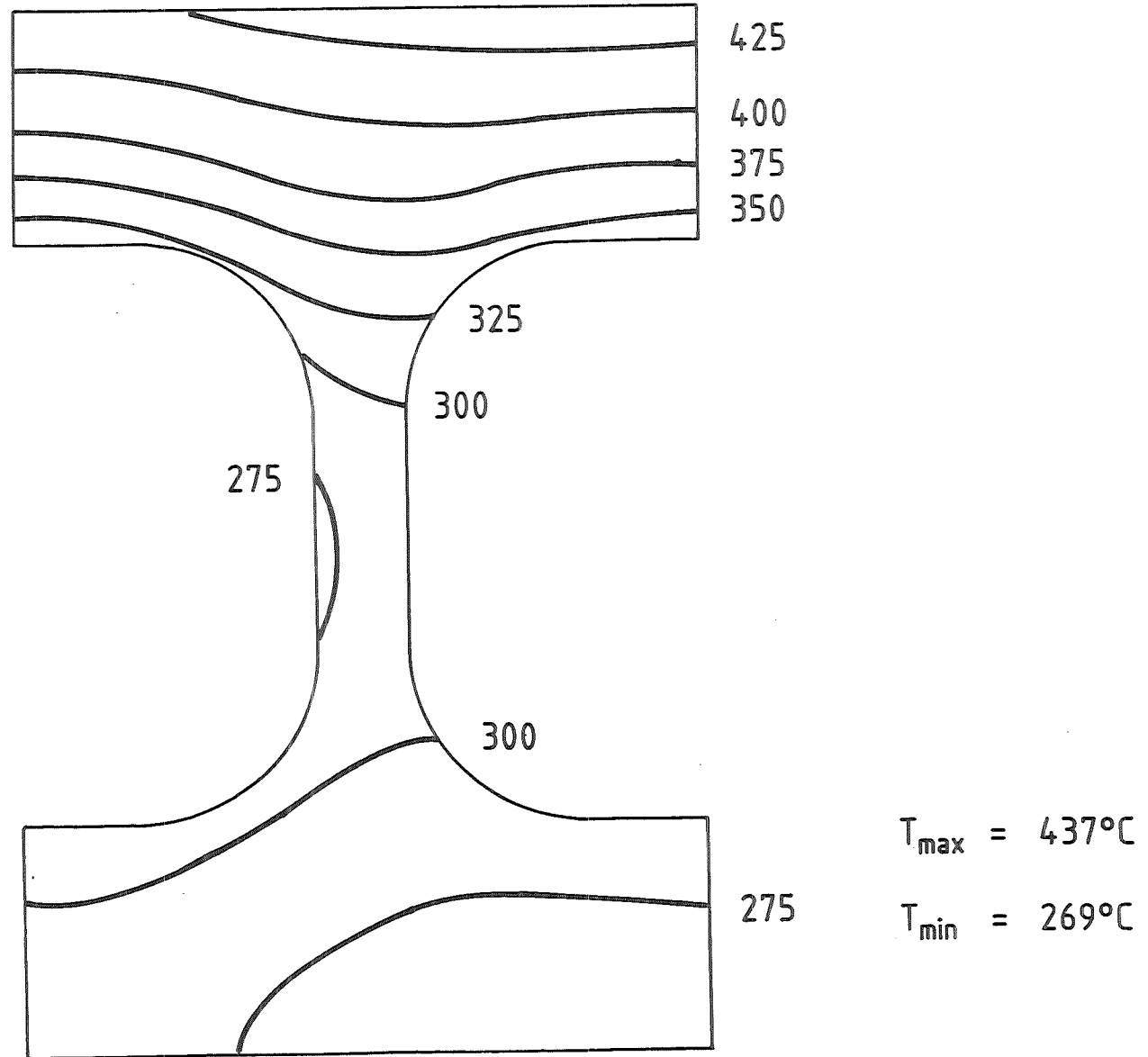
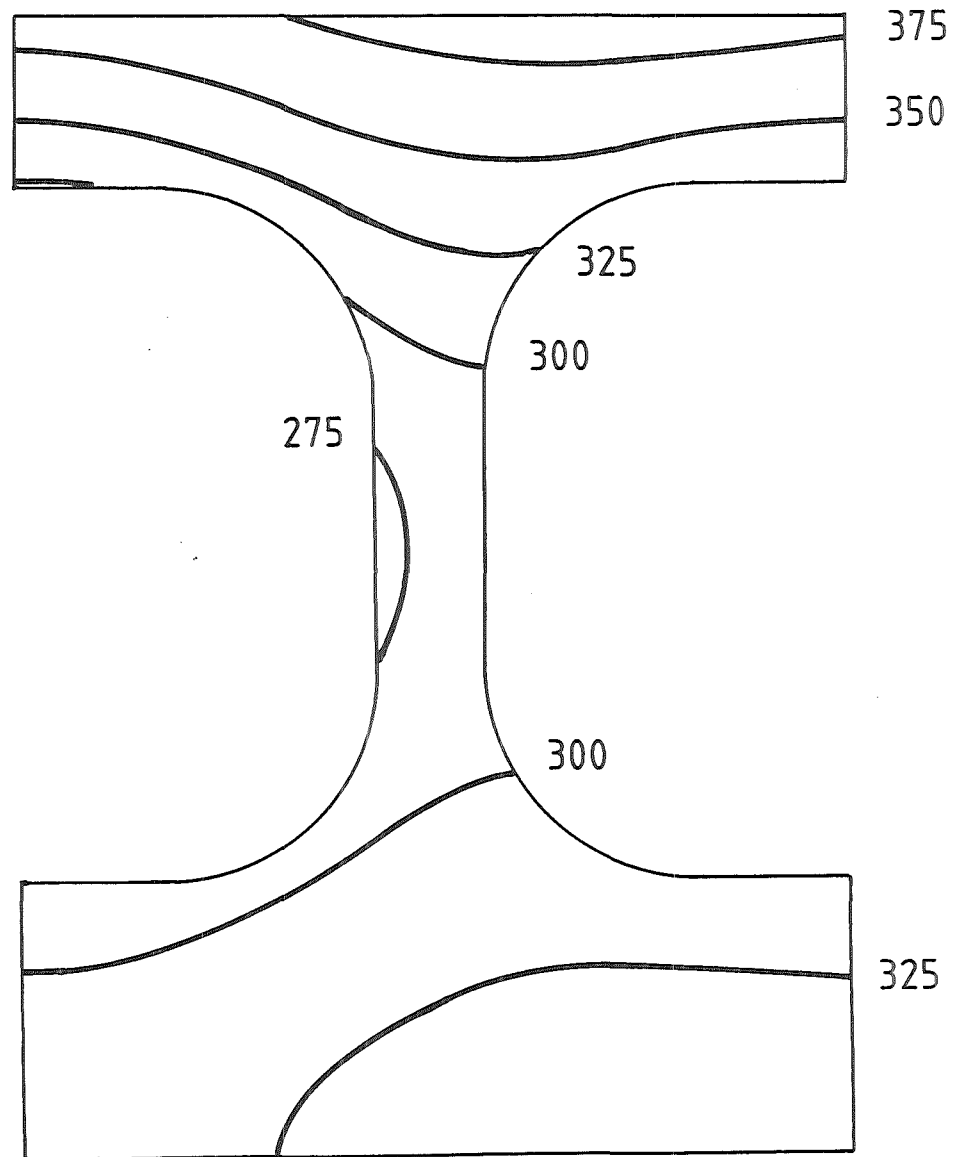


Fig: B1.3 Contour plot of temperature distribution for austenitic steel (case 3)



$$T_{\max} = 390^{\circ}\text{C}$$

$$T_{\min} = 268^{\circ}\text{C}$$

Fig. B1.4 Contour plot of temperature distribution for austenitic steel (case 4)

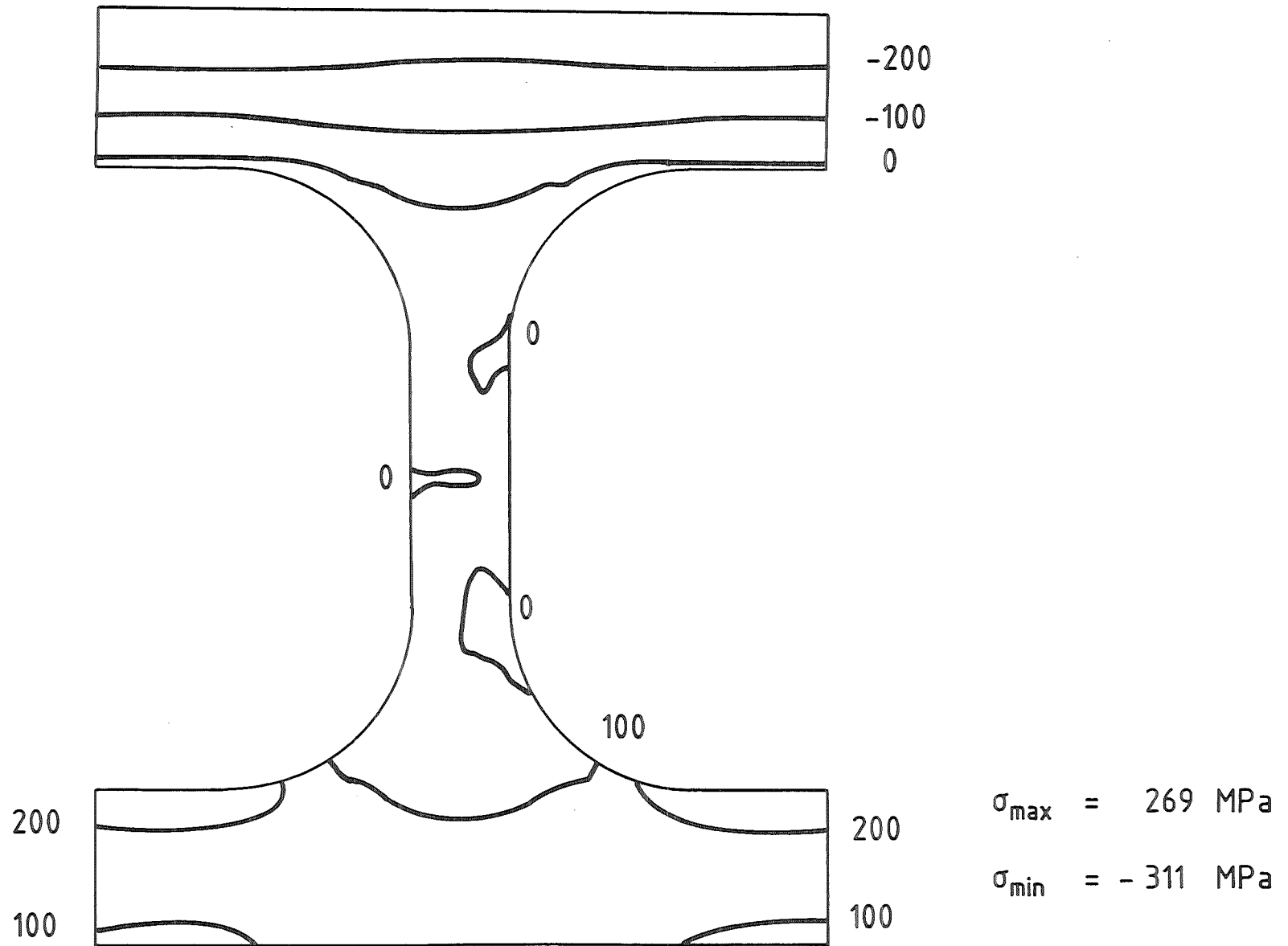


Fig. B2.2 Contour plot of thermal stress distribution σ_{xx} for austenitic steel (case 2)

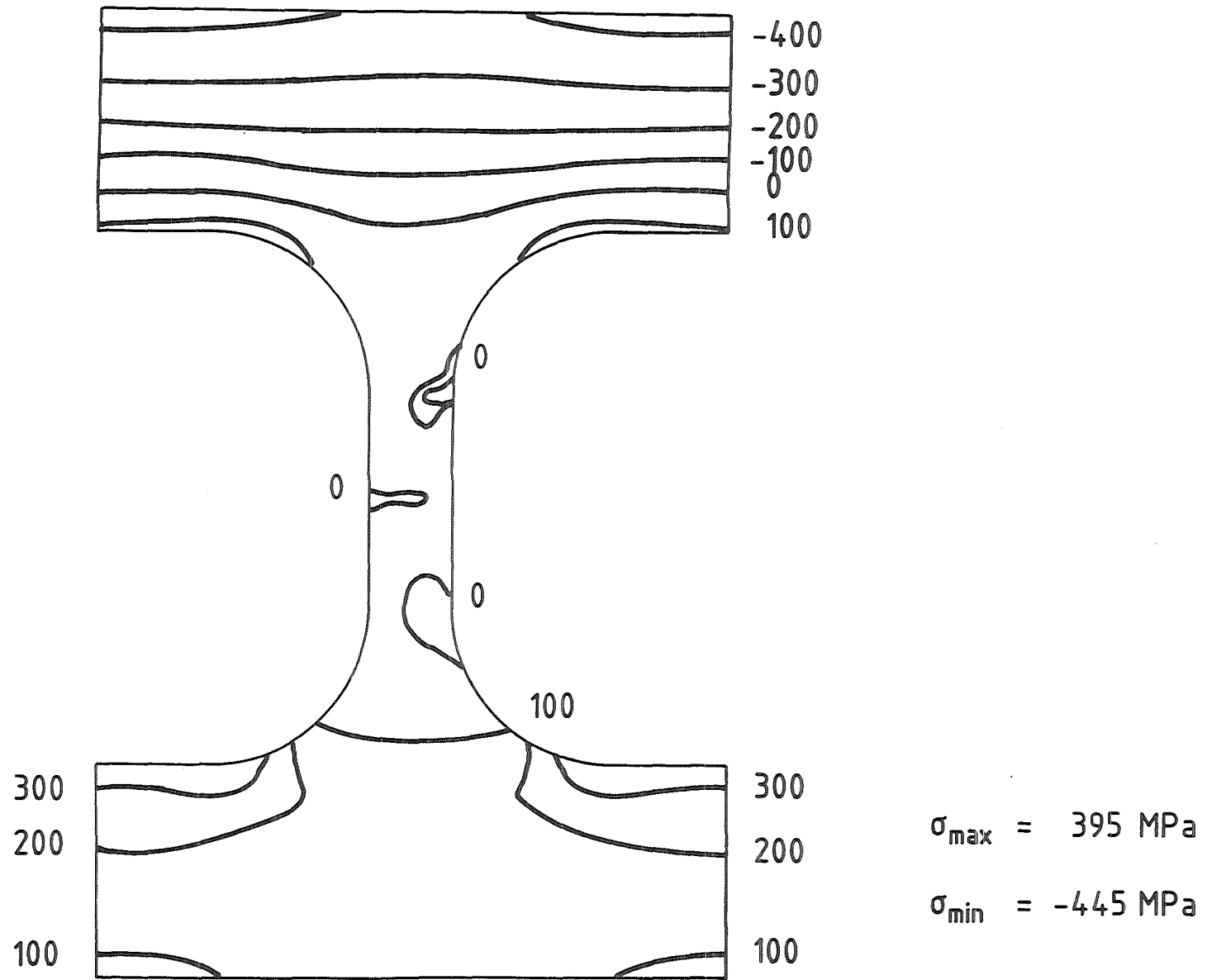


Fig. B2.3 Contour plot of thermal stress distribution σ_{xx} for austenitic steel (case 3)

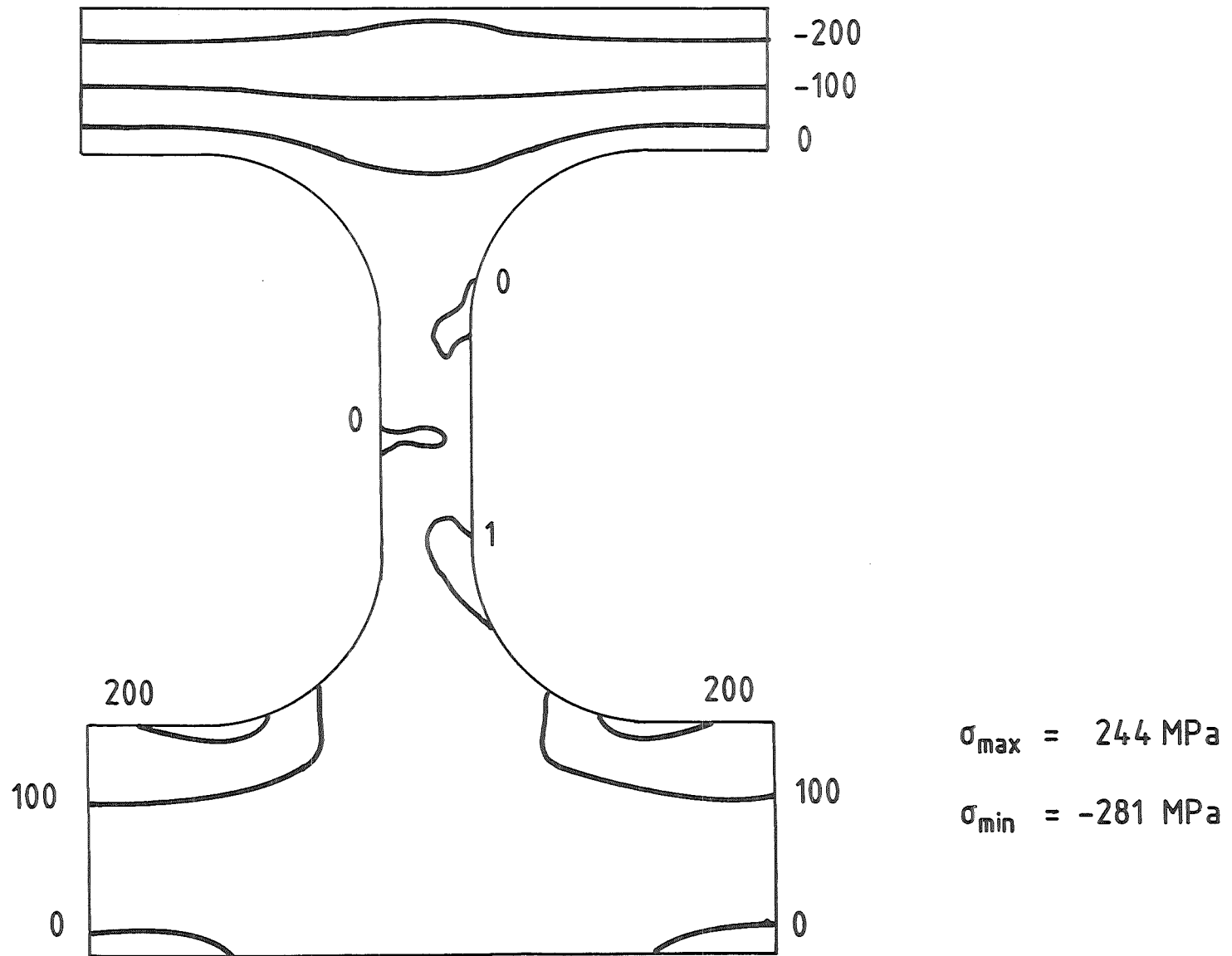


Fig. B2.4 Contour plot of thermal stress distribution σ_{xx} for austenitic steel (case 4)

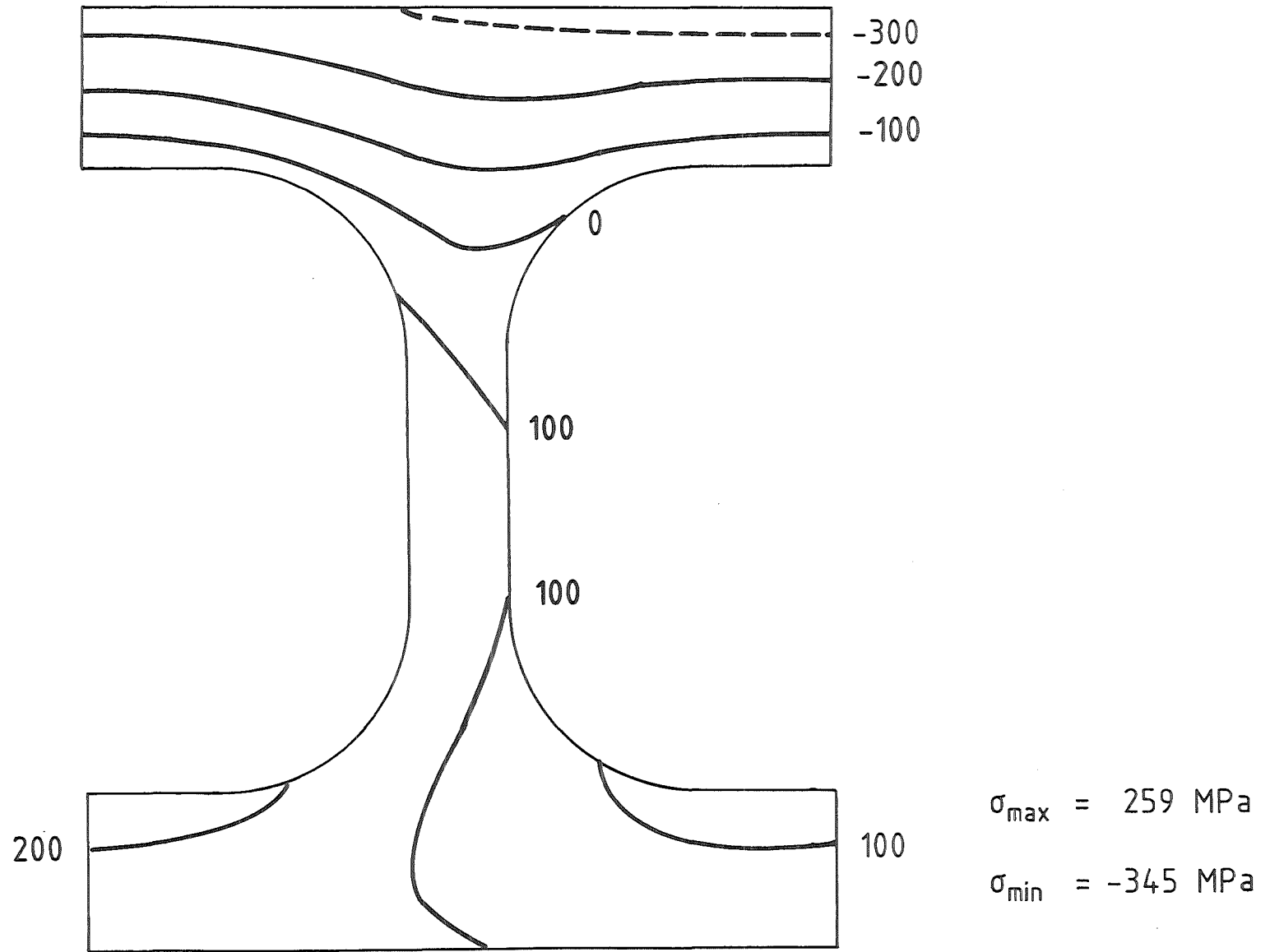


Fig. B3.2 Contour plot of thermal stress distribution σ_{zz} for austenitic steel (case 2)

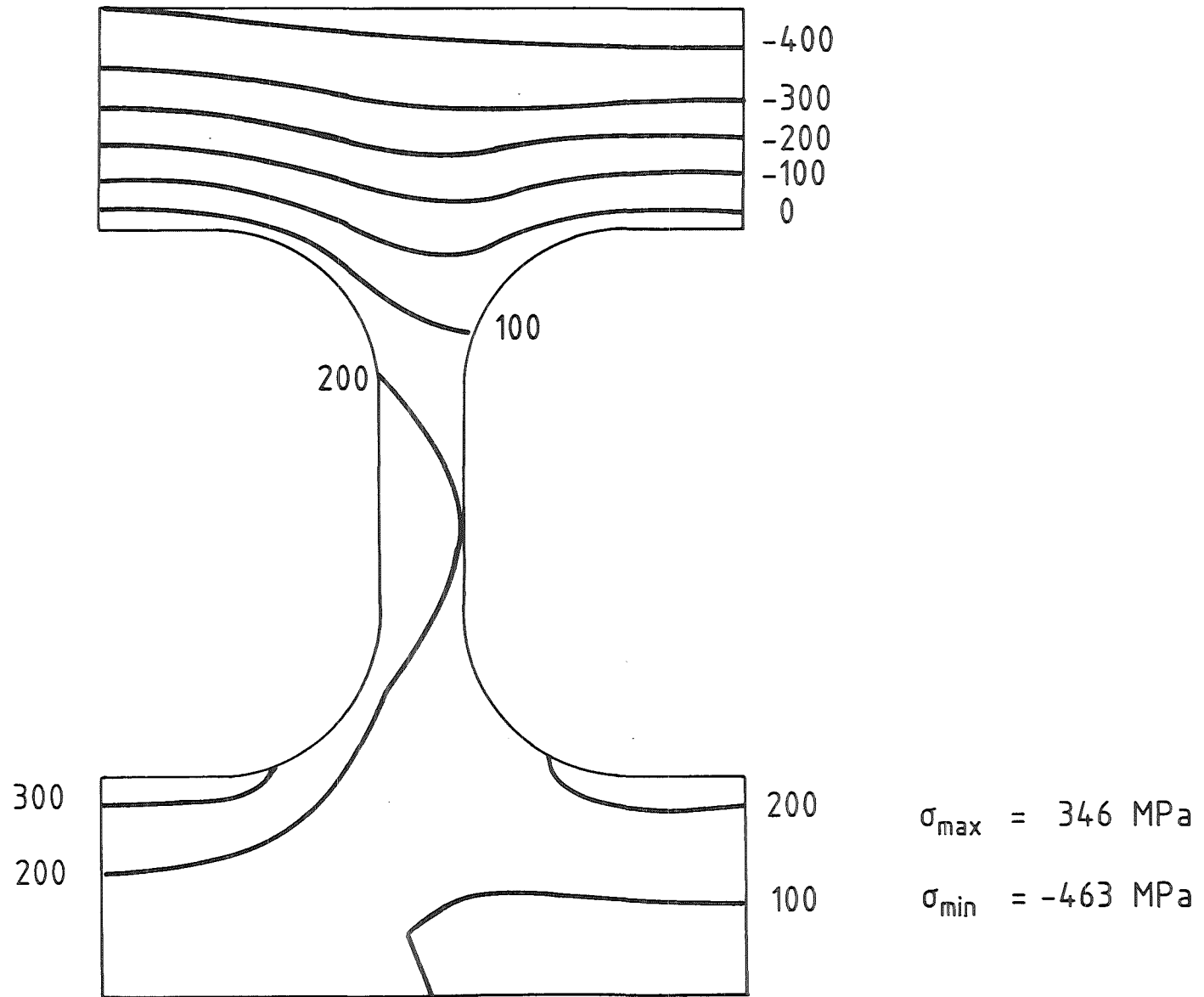


Fig. B3.3 Contour plot of thermal stress distribution σ_{zz} for austenitic steel (case 3)

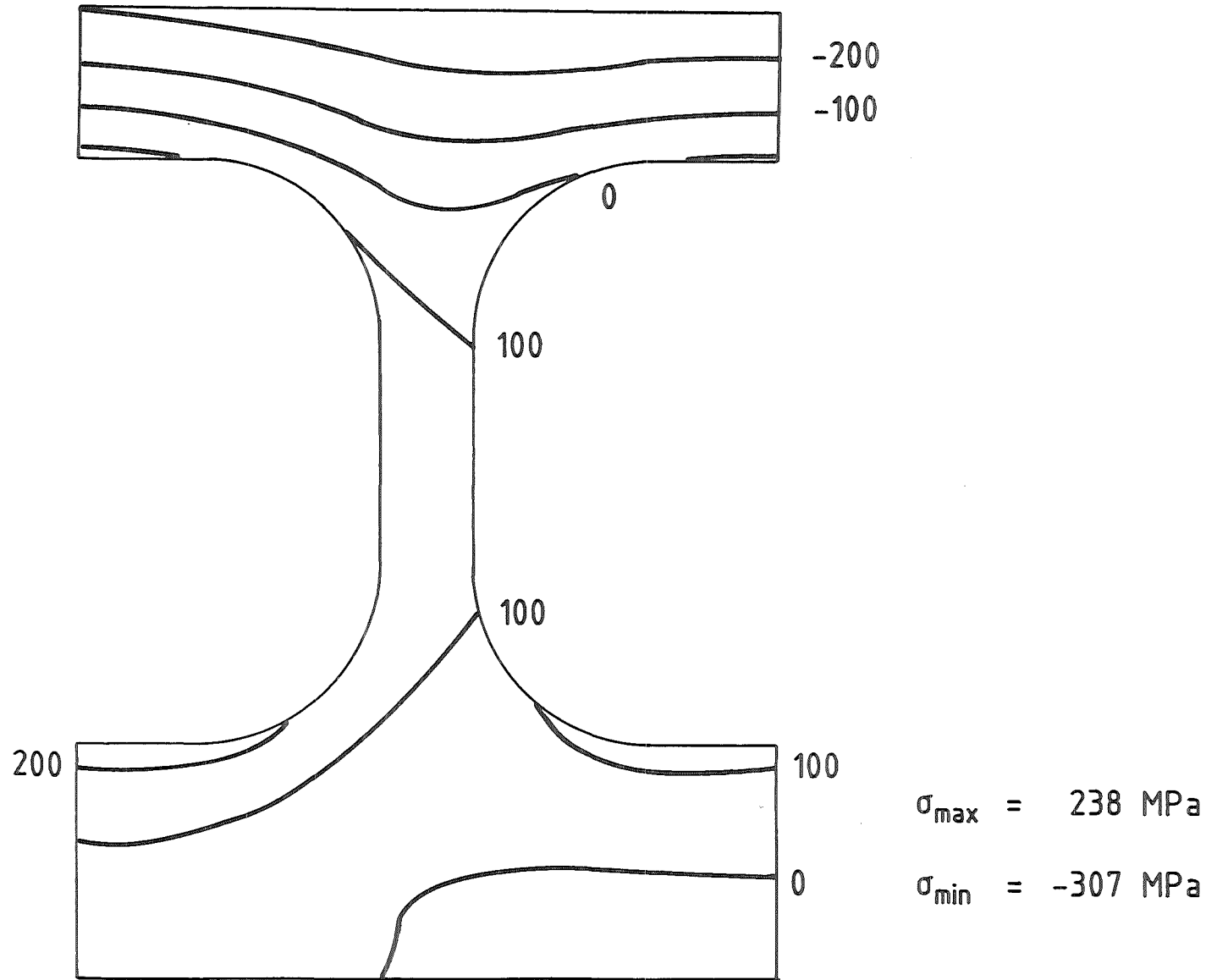


Fig. B3.4 Contour plot of thermal stress distribution σ_{zz} for austenitic steel (case 4)

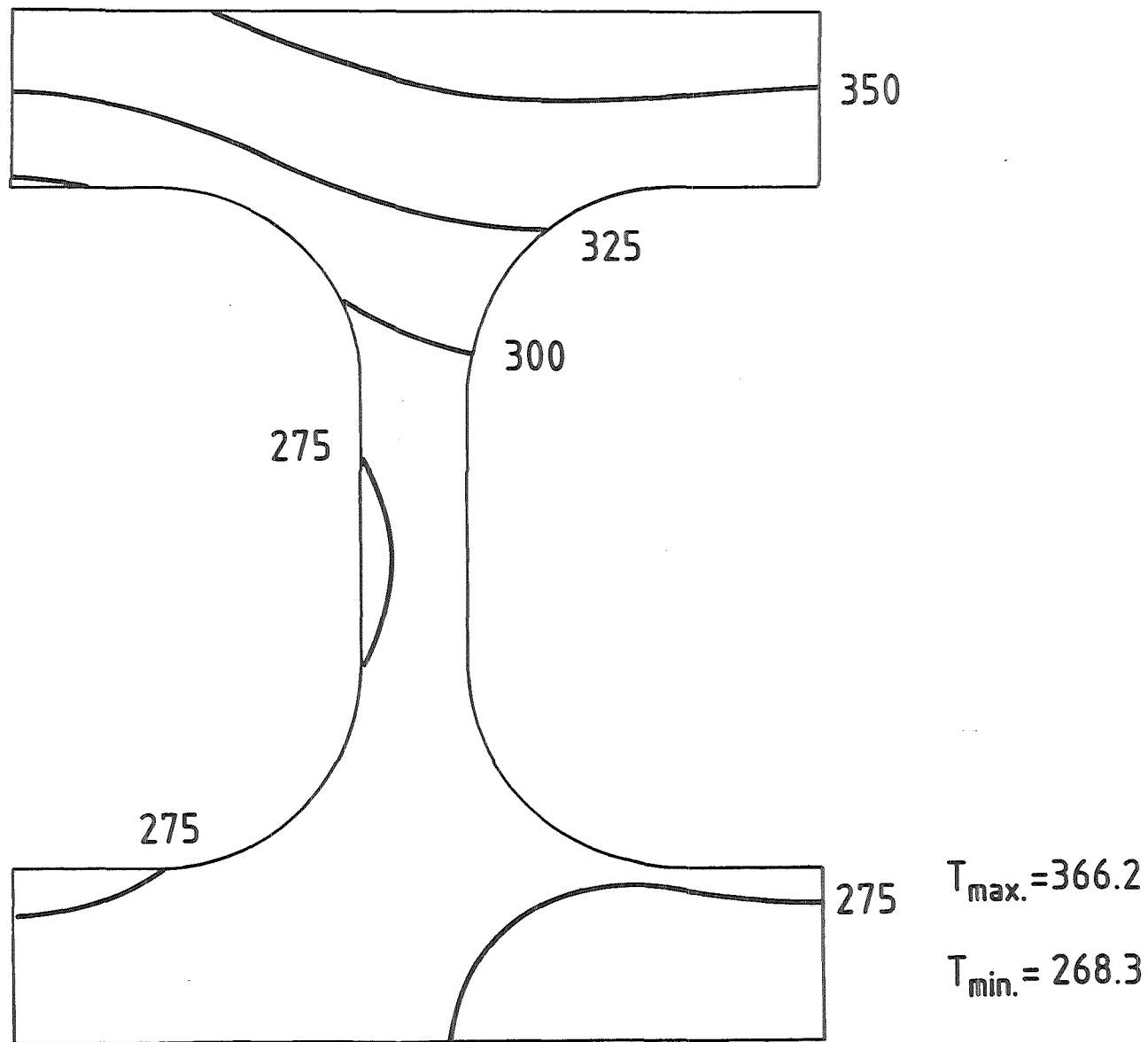
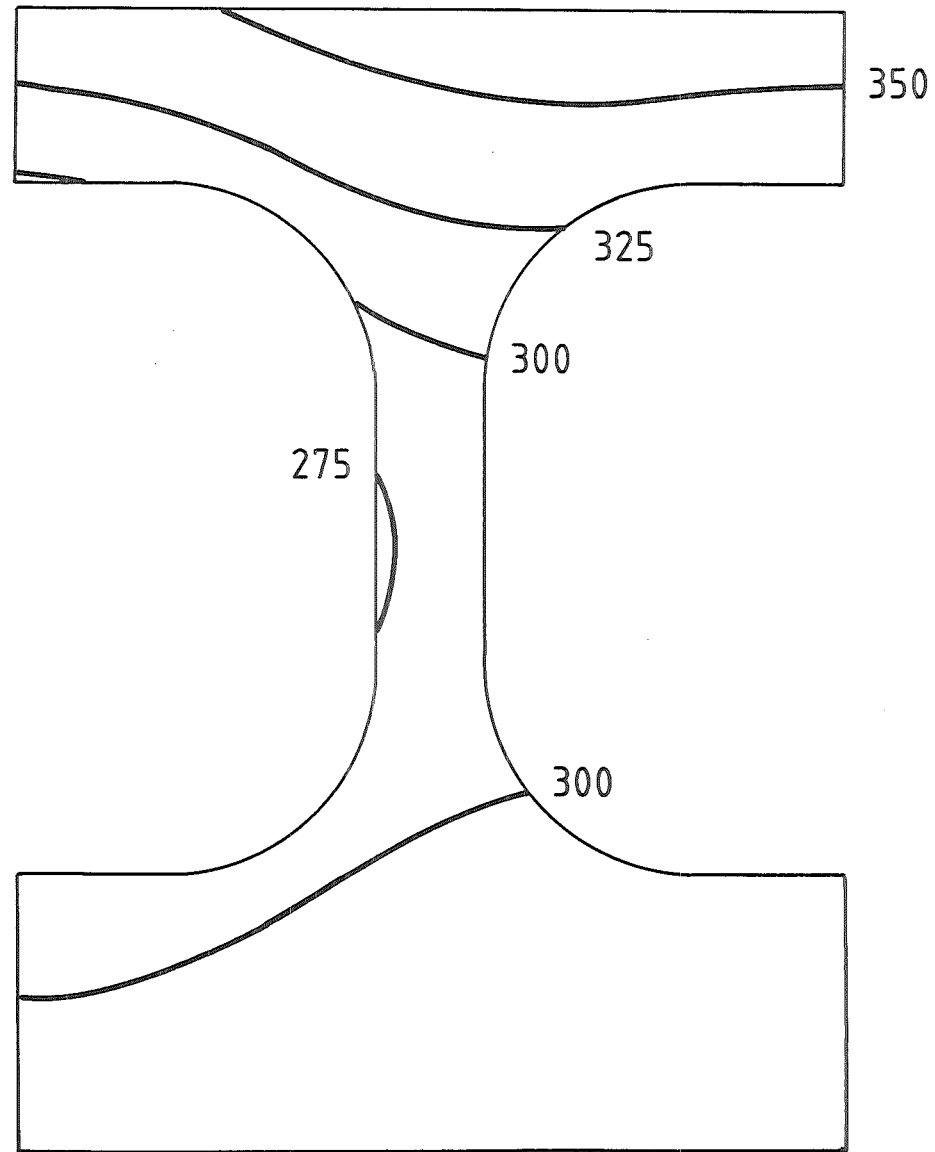


Fig. B4.2 Contour plot of temperature distribution for martensitic steel (case 2)



$$T_{\max} = 366^{\circ}\text{C}$$

$$T_{\min} = 272^{\circ}\text{C}$$

Fig. B4.4 Contour plot of temperature distribution for martensitic steel (case 4)

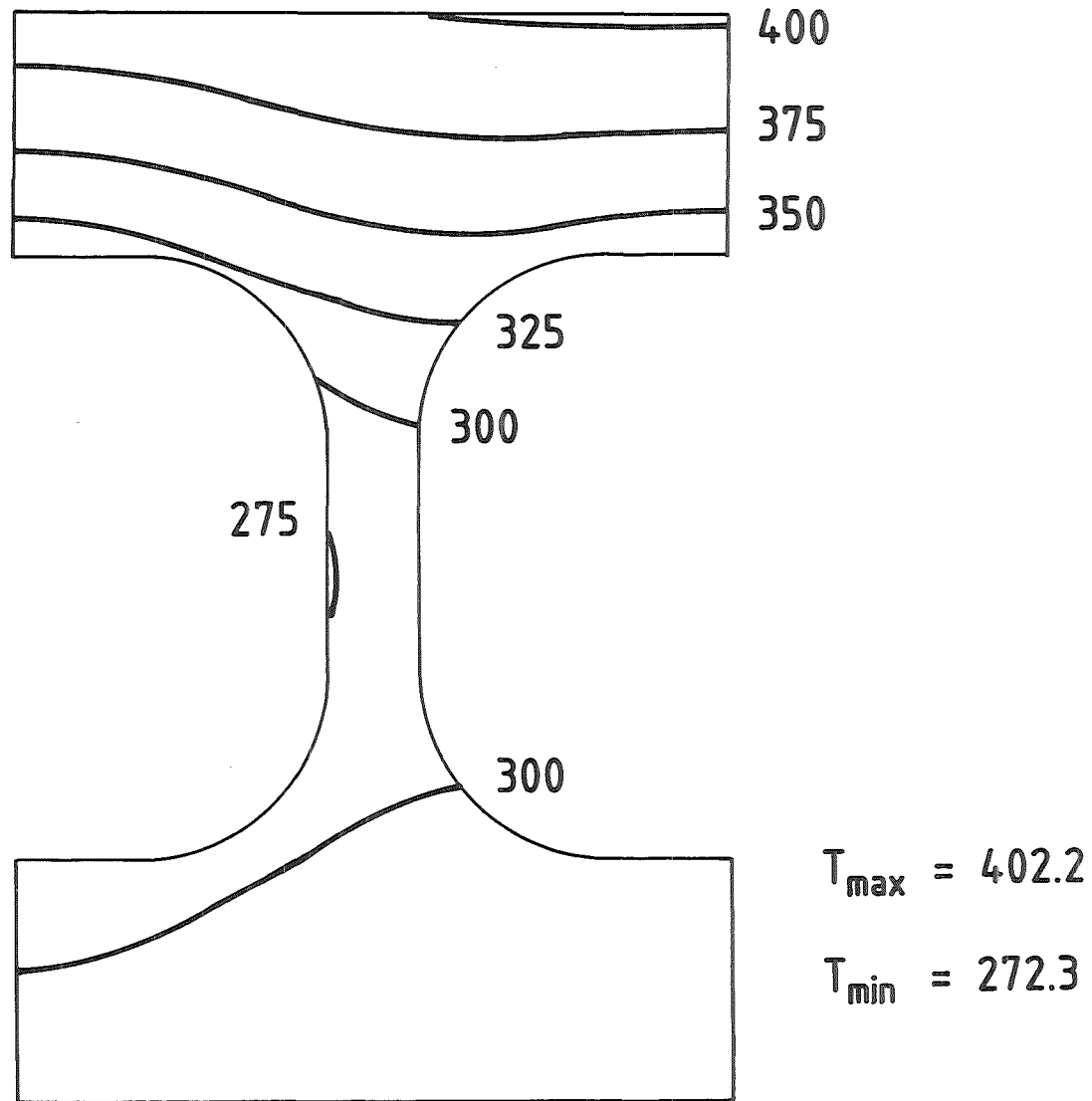


Fig. B4.3 Contour plot of temperature distribution for martensitic steel (case 3)

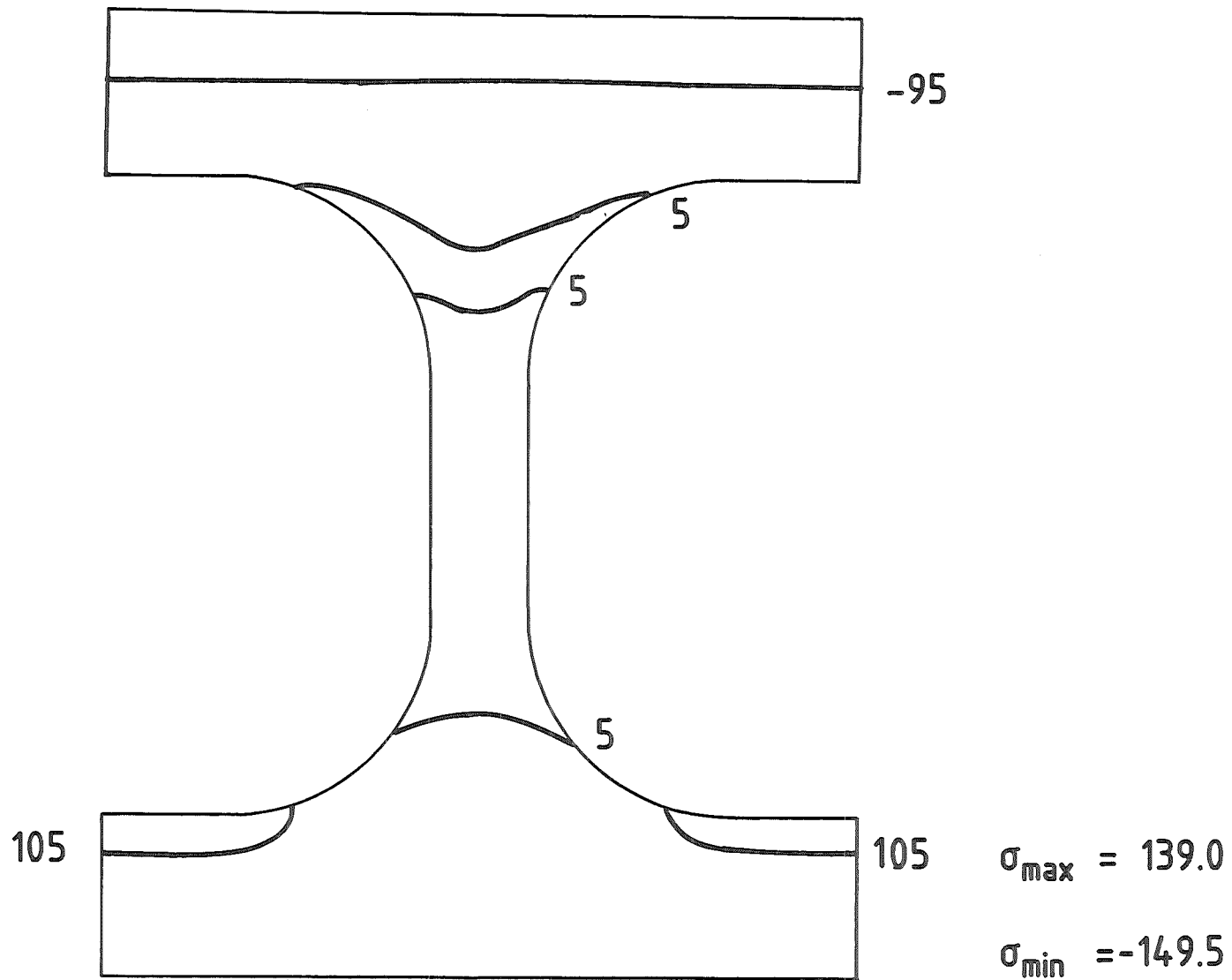


Fig B5.2 Contour plot of thermal stress distribution σ_{xx} for martensitic steel (case 2)

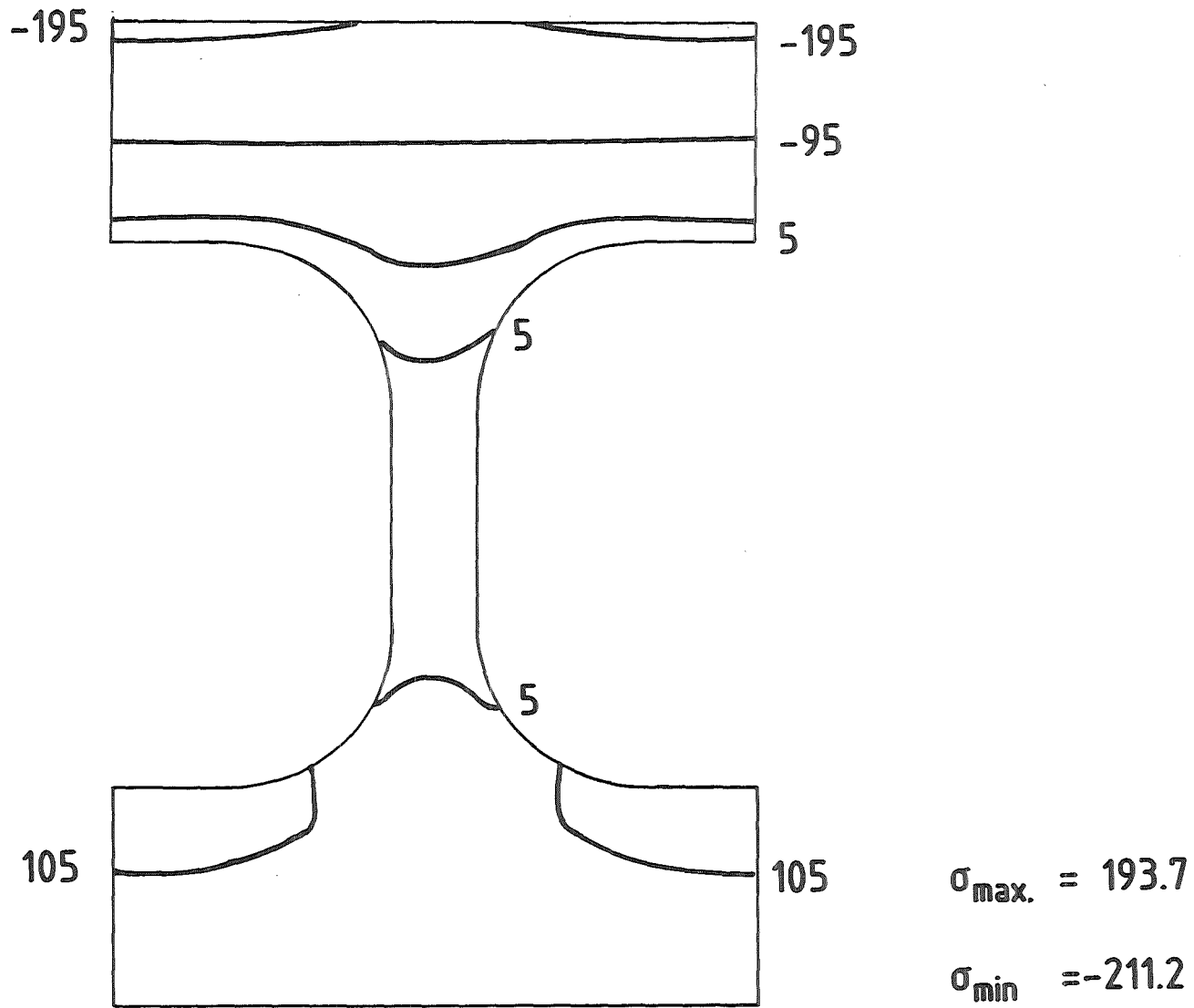


Fig. B5.3 Contour plot of thermal stress distribution σ_{xx} for martensitic steel (case 3)

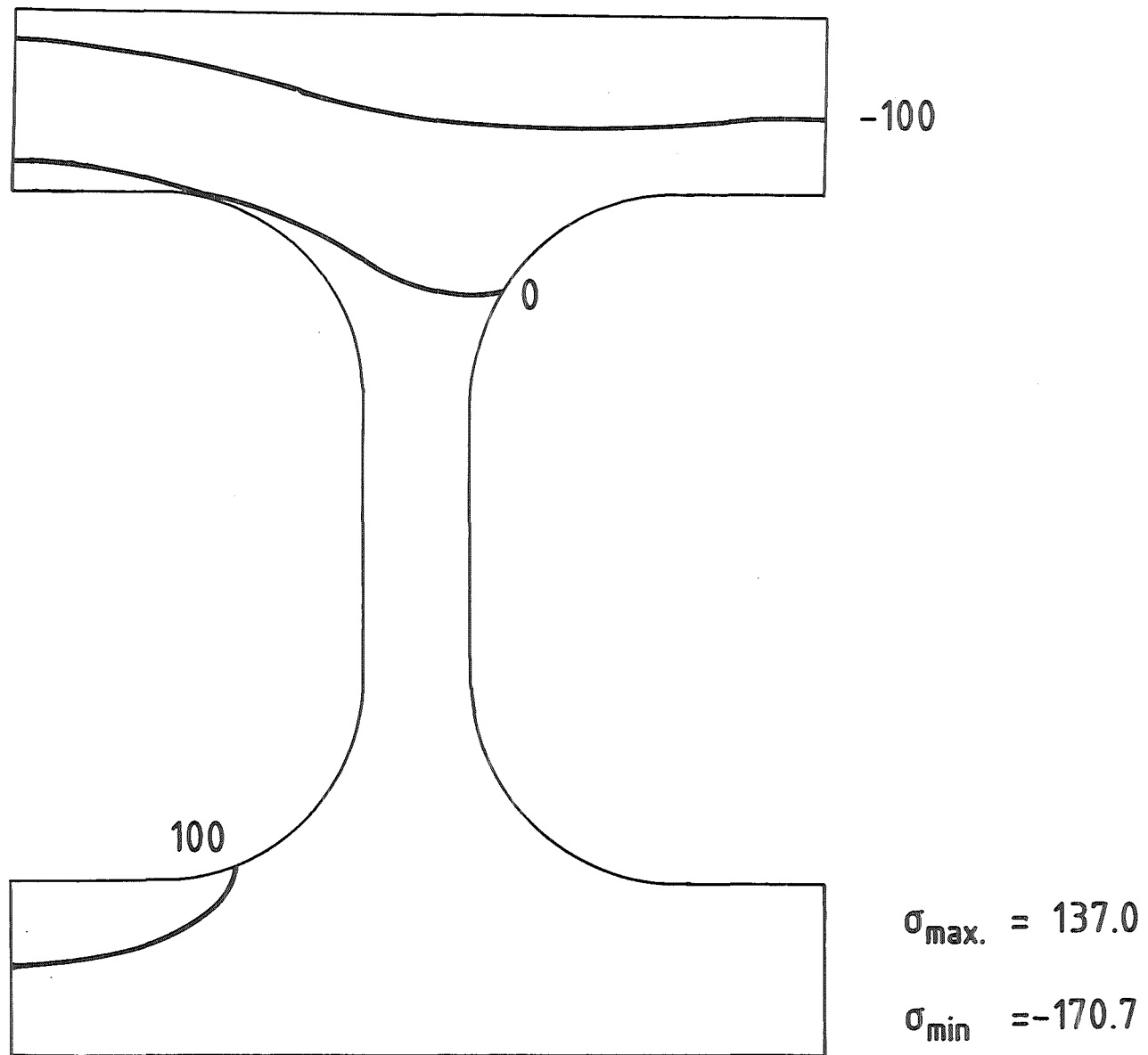
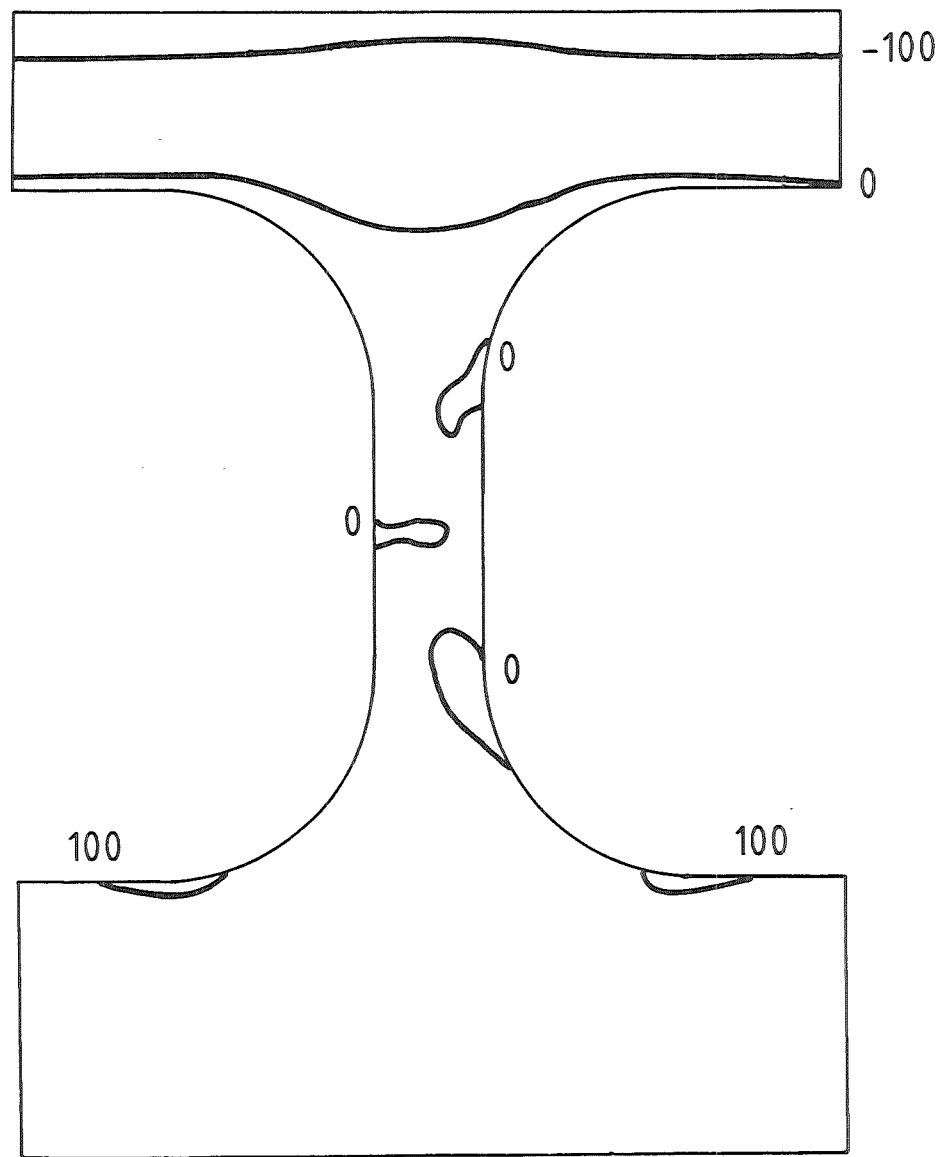


Fig. B6.2 Contour plot of thermal stress distribution σ_{zz} for martensitic steel (case 2)



$$\sigma_{\max} = 117 \text{ MPa}$$

$$\sigma_{\min} = -134 \text{ MPa}$$

Fig. B5.4 Contour plot of thermal stress distribution σ_{xx} for martensitic steel (case 4)

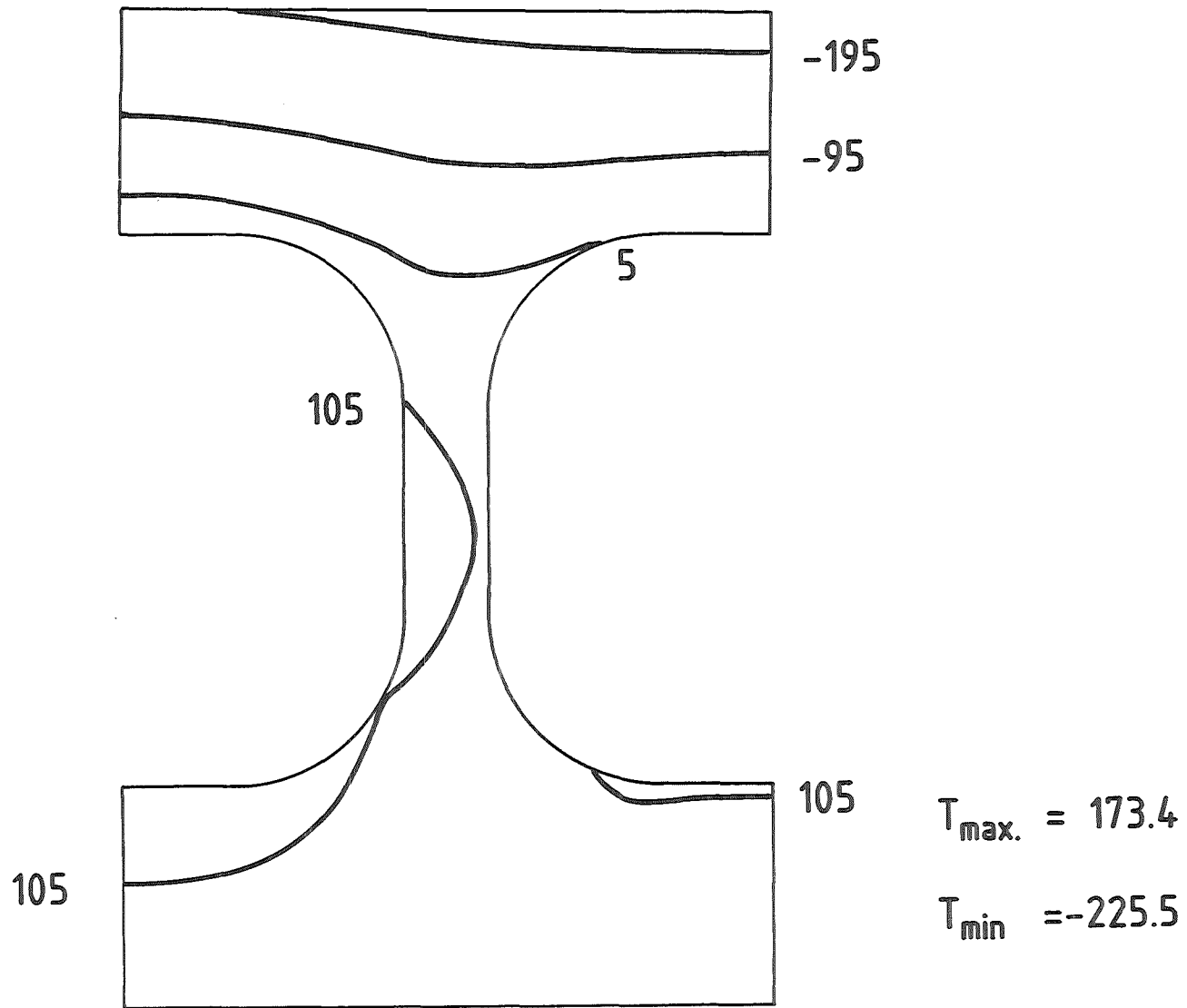
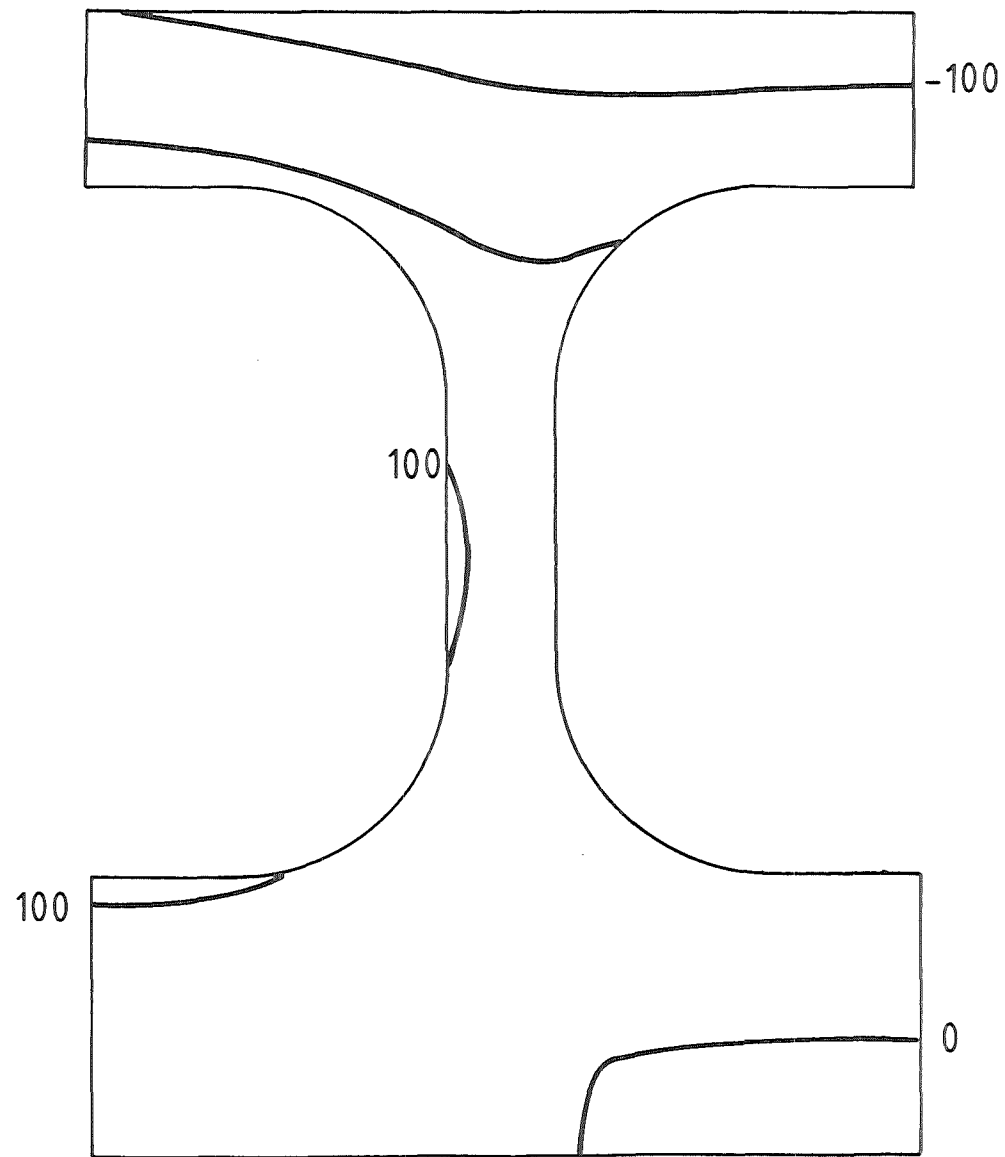


Fig. B6.3 Contour plot of thermal stress distribution σ_{zz} for martensitic steel (case 2)



$$\sigma_{\max} = 118 \text{ MPa}$$

$$\sigma_{\min} = 153 \text{ MPa}$$

Fig. B6.4 Contour plot of thermal stress distribution σ_{zz} for martensitic steel (case 2)

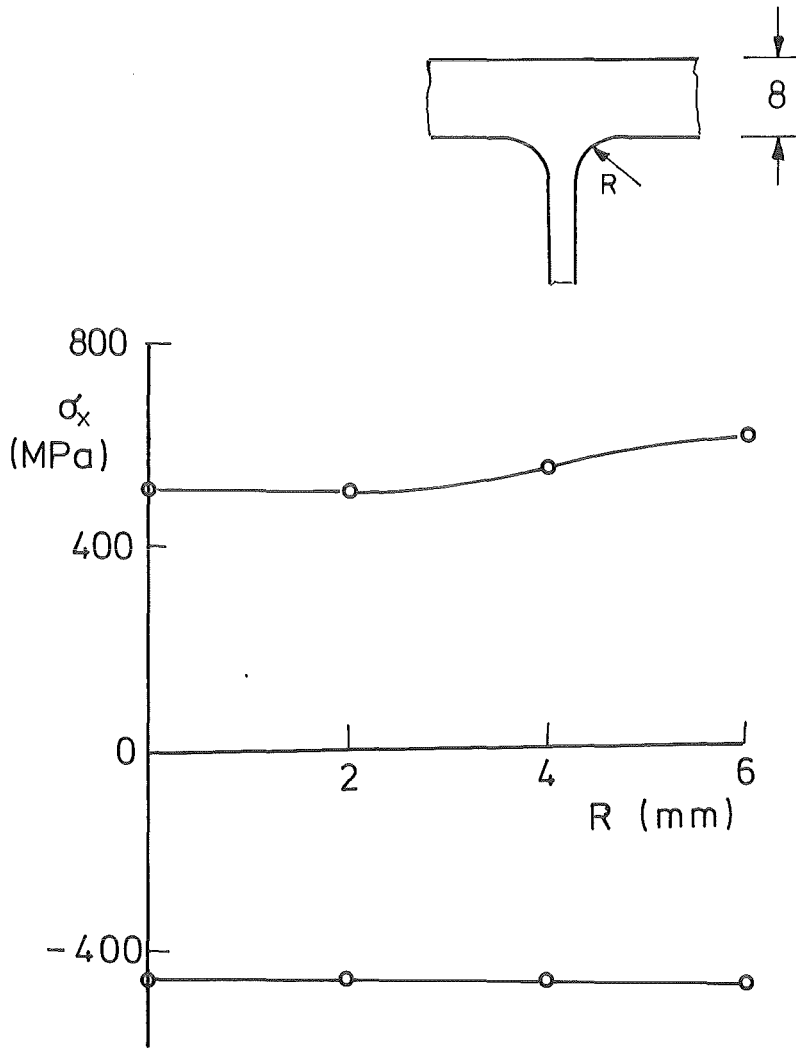


Fig. B7 Maximum tensile stresses in x-direction versus curvature radius R

T A B L E S

| | case 1 | case 1b | |
|---------------|------------|------------|-----|
| σ_{xx} | -455 488 | -287 325 | MPa |
| σ_{zz} | -481 413 | -393 346 | MPa |

Table 1

Stress ranges comparing different boundary conditions ('free expansion' against 'free expansion and bending')

Coefficients of eq.(4)

| | SS316 20% CW | | | 1.4914 | | |
|----------------|--------------|------------|------------|--------|------------|------------|
| | T | σ_x | σ_z | T | σ_x | σ_z |
| A ₀ | 442.0 | -448. | -481. | 402. | -209. | -230. |
| A ₁ | -71.3 | 460. | 416. | -41.7 | 196.3 | 145. |
| A ₂ | -9.3 | -200. | -251. | -54. | -28.7 | 96. |
| A ₃ | -44.7 | 544. | 699. | 58.7 | 122.7 | 11. |
| A ₄ | 21.3 | -256. | -331. | -32. | -53.3 | - |

Coefficients of eq.(6)

| | SS316 20% CW | | | 1.4914 | | |
|----------------|--------------|------------|------------|--------|------------|------------|
| | T | σ_x | σ_z | T | σ_x | σ_z |
| A ₀ | 300. | 445. | 412. | 297. | 220. | 210. |
| A ₁ | 22.3 | -265.7 | 196.7 | 15.6 | -109.3 | -105.3 |
| A ₂ | 6.7 | -60.7 | -125.3 | -5. | -62.7 | 9.3 |
| A ₃ | -37.3 | 154.7 | 458.7 | -5.9 | 85.3 | 53.3 |
| A ₄ | 31.3 | -53.3 | 298.6 | 3.2 | -21.3 | -21.3 |

Table 2

| | case 1 | case 2 | case 3 | case 4 | |
|-------------------|------------|------------|------------|------------|-----|
| austenitic steel | | | | | |
| σ_{xx} | -455 488 | -311 269 | -445 395 | -281 244 | MPa |
| σ_{zz} | -481 413 | -345 259 | -463 346 | -307 238 | MPa |
| T | 268 442 | 266 389 | 269 437 | 268 390 | °C |
| martensitic steel | | | | | |
| σ_{xx} | -213 241 | -149 134 | -211 194 | -134 117 | MPa |
| σ_{zz} | -231 208 | -171 137 | -226 173 | -152 119 | Mpa |
| T | 268 402 | 268 366 | 272 402 | 272 366 | °C |

Table 3

Stress ranges for several geometries and two materials

- case 1 (d = 8 mm , c = 5 mm), reference geometry
- case 2 (d = 5 mm , c = 5 mm)
- case 3 (d = 8 mm , c = 8 mm)
- case 4 (d = 5 mm , c = 8 mm)